國立臺灣大學物理研究所　　博士論文

指導教授：　　高涌泉,李世昌,葉恭平

在質心能量爲 $1.8\,\mathrm{TeV}$ 的質子-反質子對撞機中

測量雙輕子模態的頂夸克質量

研究生:葉平　　撰

中華民國85年6月

國 立 台 灣 大 學

物 理 學 研 究 所

葉 平 君 之 博 士 學 位 論 文

經考試合格特此證明

考試委員

李世昌

鄧炳坤

侯維恕

張元翰

葉恭平

林崇棻

徐鎧鋒

指導教授

李世昌

葉恭平

高涌泉

中華民國 85 年 6 月 13 日

授權書
（博碩士論文）

本授權書所授權之論文爲本人在 <u>國立臺灣</u> 大學(學院) <u>物理</u> 系(所)

<u>　　　　　</u>組 <u>八十四</u> 學年度第 <u>二</u> 學期所撰 <u>博</u> 士學位論文。

論文名稱：<u>在質心能量爲 1.8 TeV 的質子－反質子對撞機中測量</u>
<u>雙輕子模態的頂夸克質量</u>

☑同意　　　□不同意

本人具有著作財產權之*論文提要*，授予*國家圖書館*、*本人畢業學校及行政院國家科學委員會科學技術資料中心*，得重製成電子資料檔後收錄於該單位之網路，並與台灣學術網路及科技網路連線，得不限地域、時間與次數，以光碟或紙本重製發行。

- -

☑同意　　　□不同意

本人具有著作財產權之論文全文資料，授予*行政院國家科學委員會科學技術資料中心*，得不限地域、時間與次數以微縮、光碟重製後發行，並得享該中心微縮小組製作之研究報告、獎勵代表作、博碩士論文三檔資料等値新台幣伍佰元之服務。本論文因涉及專利等智慧財產權之申請，請將本論文全文延後至民國 <u>八十五</u> 年 <u>七</u> 月後再公開。

- -

☑同意　　　□不同意

本人具有著作財產權之論文*全文資料*，授予*教育部指定送繳之圖書館及本人畢業學校圖書館*，爲學術研究之目的以各種方法重製，或爲上述目的再授權他人以各種方法重製，不限時間與地域，惟每人以一份爲限。

上述授權內容均無須訂立讓與及授權契約書。依本授權之發行權爲非專屬性發行權利。依本授權所爲之收錄、重製、發行及學術研發利用均爲無償。

指導教授姓名：高涌泉、李世昌、葉恭平

研究生簽名：葉平　　　　　　　學號：F78202003
（親筆正楷）

日期：民國 85 年 7 月 10 日

- -

備註：1.上述同意與不同意之欄位若未鉤選，本人同意視同授權。
　　　2.授權第二項者，請再交論文一本予承辦人員。
　　　3.本授權書已於民國85年4月10日送請著委會修正定稿。

A Measurement of Top Quark Mass in Dilepton Channel

Using Invariant Mass of Lepton and b-jet

in $p\bar{p}$ Collisions at $\sqrt{s} = 1.8$ TeV

by

Ping Yeh

A dissertation submitted in partial fulfillment
of the requirements for the degree of
Doctor of Philosophy
in Department of Physics
of National Taiwan University
June 1996

摘要

在美國費米實驗室的對撞機偵測器(CDF)於1992年到1995年在質心能量爲1.8 TeV的環境下取了109/pb質子-反質子對撞的數據。從數據中我們觀測到10個質子-反質子變爲雙輕子加雙噴注加失稱橫向能量的頂夸克特徵事件。我們估計在這10個事件中有2.0±0.42個背景事件。經由輕子和b噴注的不變質量和頂夸克質量之間的關係,和一個簡單的配對方法,我們用這些雙輕子事件測量頂夸克的質量而得到162±21(統計誤差)$^{+6.8}_{-7.3}$(系統誤差) GeV/c^2。此結果和單輕子加噴注模態的測量175.6±5.6 GeV/c^{2}相合。我們亦討論了未來改良之可能性及途徑。

Abstract

The Collider Detector at Fermilab (CDF) has collected 109 inverse picobarn of proton anti-proton collision data from the 1992-1996 Tevatron run (Run 1), at a center of mass energy of $\sqrt{s} =$ 1.8 TeV. From the data we observed 10 $p\bar{p} \rightarrow$ dilepton + dijet + missing transverse energy candidate top quark events with an expectation of 2.0±0.42 events from backgrounds. From this sample of dilepton events, with a simple relation between top quark mass and mean invariant mass between lepton and b-jet and an algorithm to pair leptons with jets, we have measured the mass of top quark to be $162 \pm 21(stat.)^{+6.8}_{-7.3}(syst.)$ GeV/c^2, in agreement with results from lepton+jets channel 175.6 ± 5.6 GeV/c^2. The possible improvements in the future are also discussed.

Contents

List of Tables

List of Figures

viii

Chapter 1

Introduction

1.1 A Brief Overview of Standard Model

The current Standard Model of particle physics postulates that the matter in the universe are built from 3 families of 2 sectors of fermions and their anti-particles: the leptons,

$$\left(\begin{array}{c} e \\ \nu_e \end{array} \right) \left(\begin{array}{c} \mu \\ \nu_\mu \end{array} \right) \left(\begin{array}{c} \tau \\ \nu_\tau \end{array} \right),$$

and the quarks,

$$\left(\begin{array}{c} u \\ d \end{array} \right) \left(\begin{array}{c} c \\ s \end{array} \right) \left(\begin{array}{c} t \\ b \end{array} \right).$$

And the interaction among them are carried by

$$\gamma, W^\pm, Z^0, \text{gluon and (yet unobserved) Higgs boson.}$$

The photon, or γ, is familiar to physicists for a long time. The $W^\pm$ and Z^0 bosons, predicted by the electroweak theory, were discovered in CERN (European Laboratory for Particle Physics) in 1983[1, 2, 3, 4]. The existence of gluons were established by observation of three-jet events in PETRA e^+e^- collider located at DESY in 1979[5]. The Higgs boson is responsible for electroweak symmetry breaking and gives masses to W, Z bosons and all fermions. It is not observed yet.

The direct evidence of existence of all leptons except ν_τ have been established, and the existence of ν_τ was indirectly established from τ decay data combined with ν reaction data[6]. The situation

is similar in quark sector. The fifth quark, or b quark, was discovered in the $b\bar{b}$ Υ resonance states in 1977[7]. Since then a lot of experimental efforts were made to detect the t quark, or top quark. But no sign of top quark production was observed until 1994, when CDF announced the first evidence of $t\bar{t}$ production in $p\bar{p}$ collisions[8]. And the existence of top quark was later confirmed by both CDF and D0 collaboration at Fermilab in 1995. This completes the quark sector of the fundamental building blocks of matter. The only unseen particle remains in the Standard Model is the Higgs boson.

The Higgs boson can be indirectly probed in precision electroweak data. According to the Standard Model, the Higgs boson, top quark and b quark all appear in the vacuum polarization diagrams of $W^{\pm}$ and Z^0 bosons, and have an effect on the their masses. The contributions from lighter quarks are negligible because the term is proportional to the square of the fermion mass. With the presence of another standard model parameter θ_W (the weak mixing angle), we have five parameters: M_W, M_Z, M_t, M_H, and θ_W in the game. On the other hand, we have 2 constraints: there are two relations among M_Z, M_W and $\cos\theta_W$. Lots of different forms of these relations exist, we arbitrarily pick two of them here:

$$M_Z^2 = \frac{\pi\alpha}{\sqrt{2}G_F\rho\sin^2\theta_W\cos^2\theta_W}$$
$$\cos\theta_W = \frac{M_W}{M_Z}$$

where ρ is a parameter directly derived from the loop diagrams; therefore it depends on M_t and M_H: $\rho = \rho(M_t, M_H)$. Among the 5 parameters, the most precisely measured value is the mass of Z^0 boson. The world average is 91.187$\pm$0.007 GeV/c^2, or $\Delta M_Z/M_Z = 7.7 \times 10^{-5}$. Hence, the precise measurement of M_Z gives $\theta_W = \theta_W(M_t, M_H)$, which in turn gives $M_W = M_W(M_t, M_H)$, or $M_H = M_H(M_W, M_t)$. Figure 1.1 shows the relation and current measurement of M_W and M_t in Fermilab Tevatron.

It is clear that current resolutions on M_W and M_t are not enough to give a reasonable constraint on M_H. A much larger dataset and a better method to measure M_W and M_t are necessary.
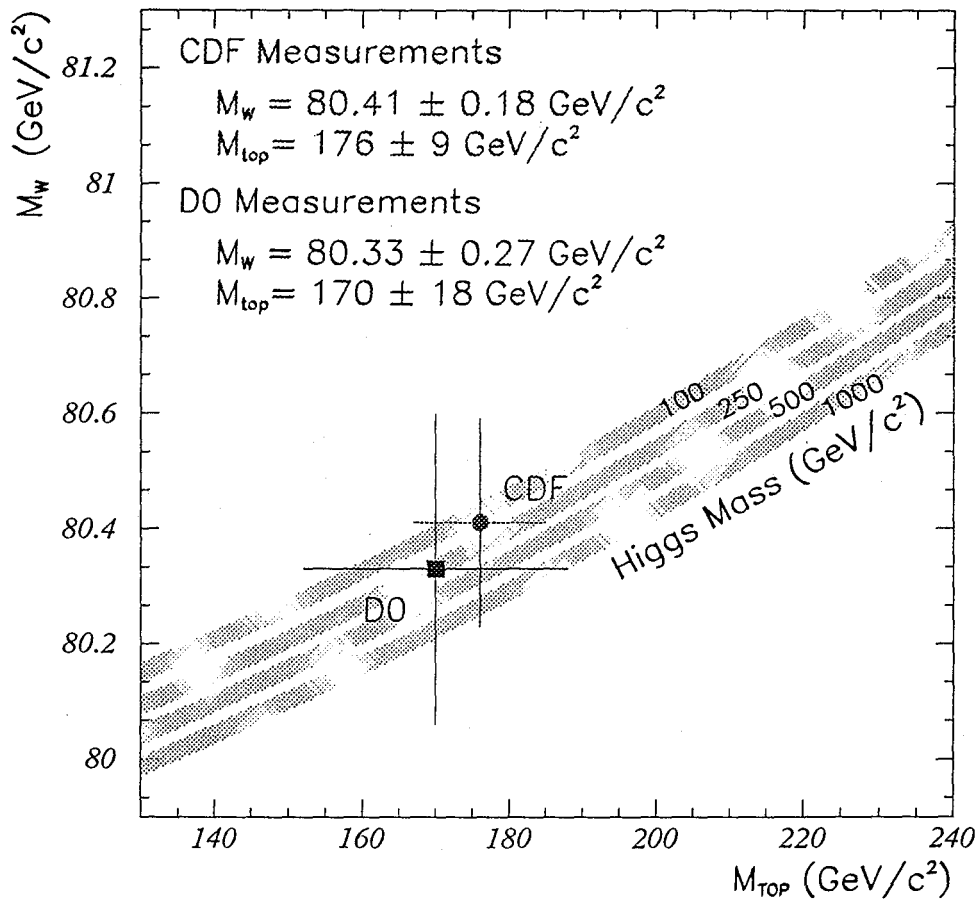
Figure 1.1: The measurement of M_W and M_t in Fermilab as of 1996, and the projection on Higgs mass.

We have shown the CDF measurement of M_t in Figure 1.1. However, it is measured in the so-called *lepton-plus-jets* channel. A direct measurement of M_t in the *dilepton* channel can provide a consistency check and a possible probe to new physics. This thesis presents a systematic method to measure the mass of top quark in the dilepton channel, and compare the result to the mass measured in the lepton+jets channel.

In the rest of this chapter we will briefly review some of the top quark physics and the proceedings in the last decade. Chapter 2 describes the Fermilab Tevatron accelerator and the CDF detector. Chapter 3 briefly shows the data path in CDF. Chapter 4 illustrates the procedure employed for selecting signal events while rejecting most of the background events. Chapter 5 develops a method to measure top quark mass, and apply the method to data. Finally, we'll reach a conclusion in Chapter 6.

1.2 "Existence of Top Quark" Before Discovery

Long before the direct discovery of top quark the physicists have believed that the top quark must exists. It is a highly anticipated particle. In this section we explain why.

There is no theory saying that a five quark Nature is absolutely impossible and top quark must exist. The top quark, if exists, by definition is the weak isospin partner of the b quark. Since the charge of the b quark was established to be $-(1/3)e$, it was only natural from the generation structure of quarks to expect that it has a partner with charge $+(2/3)e$, i.e., the top quark. If top quark doesn't exist, b quark would be a weak isospin singlet, and its interaction would be different from a theory with a doublet in the third generation. Some of these effects are appealing in theory and some others are quite visible in experiments. We elaborate a few of them here. [9]

1.2.1 Anomalies in Theory

It can be shown[10] that it is good to have weak isospin doublets because the anomaly arisen from the triangle loops can be cancelled generation by generation. If the b quark is a weak isospin singlet,

the anomaly is not cancelled in the third generation, and the gauge theory is not renormalizable. This would mean a major reform of the Standard Model is necessary. So one would prefer to have a doublet in the third generation.

1.2.2 Forward-Backward asymmetry in $e^+e^- \rightarrow Z \rightarrow b\bar{b}$ Process

Recently, the accumulation of high precision data on the neutral-current interactions has made it possible to measure the weak isospin of the b-quark. Consider the forward-backward asymmetry $A_{FB}(e^+e^- \rightarrow b\bar{b})$, defined at the Z^0 pole as

$$A_{FB}(e^+e^- \rightarrow b\bar{b}) \equiv \frac{N(forward) - N(backward)}{N(forward) + N(backward)},$$

where $N(forward)$ is number of events collected in the phase space with $\theta(e^-, b) < \pi/2$ and $N(backward)$ is for $\theta(e^-, b) > \pi/2$. Within the Standard Model, $A_{FB}(e^+e^- \rightarrow b\bar{b})$ is related to the third component of b quark's isospin and the vector and axial vector couplings of the fermions to the Z boson. It is expected to be 0.0997, assuming b is one member of a doublet and $\sin^2 \theta_W = 0.2321$. It would be zero if b is singlet.

The asymmetry has been measured in several e^+e^- colliding experiments. The recent results from LEP gives $A_{FB}(e^+e^- \rightarrow b\bar{b})$ = 0.087 ± 0.012 from L3 collaboration[11], 0.107 ± 0.011 from DELPHI collaboration[12] and 0.0963 ± 0.0077 from OPAL collaboration[13], all consistent with the assumption of existence of top quark.

1.2.3 Absence of Flavor Changing Neutral Currents

Historically, Glashow, Iliopoulos and Maiani[14] introduced the fourth quark to provide a partner for the s quark to explain the absence of strangeness-changing neutral currents like $K \rightarrow \mu^+\mu^-$. This is well-known as the GIM mechanism. Now we see that the absence of $b \rightarrow s\ell^+\ell^-$ is an analogy. Experimentally, CLEO collaboration has reported BR($b \rightarrow \ell^+\ell^- X$) < 1.2 × 10^{-3} with a 90% confidence level [15]. This provides a phenomenological ground for the existence of top quark.

1.3 Recent History of Top Quark Search

We give a brief list of results of past top search experiments in Table 1.1.

Year	Collab	$\sqrt{s}$	Channels	Data	Result
1988	UA1 [19]	546 630	$p\bar{p} \to W + X(W \to tb)$ $p\bar{p} \to Z + X(Z \to t\bar{t})$ $p\bar{p} \to t\bar{t} + X$	700 nb^{-1}	$M_t > 44$ GeV/c^2
1991	CDF[20]	1800	$p\bar{p} \to t\bar{t}X$, e+jets	4.1 pb^{-1}	$M_t > 77$ GeV/c^2
1992	CDF[21]	1800	$p\bar{p} \to t\bar{t}X$, dileptons	4.1 pb^{-1}	$M_t > 91$ GeV/c^2
1994	D0[22]	1800	$p\bar{p} \to t\bar{t}X$ lepton+jets, dilepton	15 pb^{-1}	$M_t > 131$ GeV/c^2
1994	CDF[8]	1800	$p\bar{p} \to t\bar{t}X$ lepton+jets and dilepton	19.3 pb^{-1}	First Evidence $M_t = 174 \pm 10^{+13}_{-12}$ GeV/c^2 $\sigma = 13.9^{+6.1}_{-4.8}$ pb
1995	CDF[17]	1800	same as above	67 pb^{-1}	Confirmation. $M_t = 176 \pm 8 \pm 10$ GeV/c^2 $\sigma = 6.8^{+3.6}_{-2.4}$ pb significance = 4.8 σ
1995	D0[18]	1800	same as above	~ 50 pb^{-1}	$M_t = 199^{+19}_{-21} \pm 22$ GeV/c^2 $\sigma = 6.4 \pm 2.2$ pb significance = 4.6 σ

Table 1.1: Experimental results of top search in the past. The unit of $\sqrt{s}$ is GeV.

1.4 Production of Top Quarks in $p\bar{p}$ Collisions

In a $p\bar{p}$ collider environment, top quarks are mainly produced in $t\bar{t}$ pairs through the following two processes:

$$q\bar{q} \to t\bar{t} + X,$$

$$gg \to t\bar{t} + X.$$

For a large range of M_t and $\sqrt{s}$ the cross section of the gluon fusion process is larger than that of the $q\bar{q}$ annihilation process. However, for a heavy top quark with mass ≈ 170 GeV/c^2, the $q\bar{q}$

channel contributes about 90% of the production rate in Tevatron because the quark luminosities are much larger than the gluon luminosities for large x.

Single top quark production processes are also possible, but it is expected to be rare. The Standard Model calculation of the production rate is about one order of magnitude smaller than $t\bar{t}$ processes at $\sqrt{s} = 1.8$ TeV.

1.5 The Decay of a Top Quark

Because top quark mass is larger than $M_W + M_b$, the dominant decay is the semi-weak process $t \to bW^+$ assuming the mass of Higgs boson is not lighter than M_t, and the W^+ is mostly real. The decay rate is[23]

$$\Gamma(t \to bW^+) = \frac{G_F M_W^2}{8\pi\sqrt{2}} \frac{1}{M_t^3} \left[\frac{(M_t^2 - M_b^2)^2}{M_W^2} + M_t^2 + M_b^2 - 2M_W^2 \right] \times \sqrt{[M_t^2 - (M_W + M_b)^2][M_t^2 - (M_W - M_b)^2]}$$

If we assume $M_t \approx 175$ GeV/c^2, we can get

$$\Gamma(t \to bW^+) \approx 1.55 \text{GeV}.$$

This directly translates to the lifetime of the top quark being approximately 0.4×10^{-24} sec. The heavy top quark makes the lifetime much shorter than the typical hadronization time thus it decays before it forms any kind of hadrons, including "toponium."

The b quark from top quark decay typically hadronizes into a jet, and the W^+ boson can decay into lepton pairs or quark pairs, resulting in different final states:

$$\begin{pmatrix} e^+ \\ \nu_e \end{pmatrix}, \begin{pmatrix} \mu^+ \\ \nu_\mu \end{pmatrix}, \begin{pmatrix} \tau^+ \\ \nu_\tau \end{pmatrix}, \begin{pmatrix} c \\ \bar{s} \end{pmatrix}, \begin{pmatrix} u \\ \bar{d} \end{pmatrix}.$$

Hence, in a $t\bar{t}$ decay, we can speak of 3 major channels:

- *dilepton* channel: Both W bosons decay leptonically. The event signature is 2 high energy leptons, 2 jets from b quark and $\bar{b}$ quark, and a large missing transverse energy due to the 2 un-detected neutrinos.

7

- *lepton+jets* channel: One W decays into leptonic channel, and the other W decays into $q\bar{q}'$, which results in 2 jets. The event signature is 1 high energy lepton, 4 jets, and a large missing transverse energy from the neutrino in W decay.

- *all hadronic* channel: Both W bosons decay into $q\bar{q}'$. The event signature is 6 jets.

Since a top quark doesn't hadronize before it decays, and the lifetime is much shorter than the typical time for spin-flip interactions, the information about its spin is retained when it decays. The spin of top and anti-top quarks might be correlated in the s-channel diagrams and the effect can be seen from the angular distribution of final state particles. This is the first time that we can see the spin of a bare quark. The current data accumulated in Tevatron experiments are not enough to have a concrete conclusion about this correlation. In the Collider Run II of Fermilab this effect is observable if it exists.

The top quark is also a good source of longitudinal polarized W bosons. According to the Standard Model[24],

$$BR(t \to bW^+_{longi})/BR(t \to bW^+_{any}) = \frac{M_t^2}{M_t^2 + 2M_W^2}$$

For $M_t \approx 175$ GeV/c^2, $\sim 70\%$ of top quarks decay to longitudinal W bosons. This fraction can be determined experimentally by measuring the invariant mass of the lepton from W decay and the b jet. New physics that couples to longitudinal W bosons may change this fraction, and could be probed.

Chapter 2

The Fermilab Accelerator and the CDF Detector

The data for this analysis were taken at Fermi National Accelerator Laboratory located at Batavia, Illinois, U.S.A. from June 1992 to February 1996. The experiment consists of two major apparatus: the accelerator and the detector. The accelerator provides proton beams and anti-proton beams traveling in opposite directions and collide at the center of the detector. There are two collider detectors in Fermilab: Collider Detector at Fermilab (CDF) and D-Zero (D0). The detectors then detect the final state particles that come out of the collision, and physicists can analyze the data to obtain physics results.

This analysis is based on data collected in CDF. We describe the accelerator in Section 2.1 and the CDF detector in Section 2.2.

2.1 The Fermilab Accelerator

Figure 2.1 shows a schematic view of the Fermilab accelerators. The protons are produced and accelerated in the following procedures until they reach 150 GeV:

1. Bottles of gaseous hydrogen are used as sources of protons.

2. Hydrogen gases are injected into an ion source to make negatively-charged hydrogen ions and

9
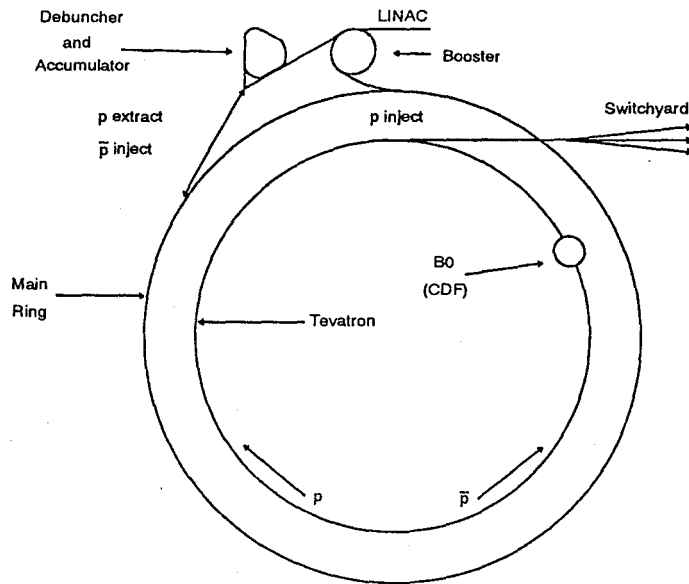
Figure 2.1: Diagram of the Fermilab accelerators.

they are extracted at energy roughly 18 keV.

3. 740 kV potential difference is used to accelerate the ions electrostatically to $\approx$ 750 keV.

4. The H^- ions are accelerated in the Drift Tube Linac to 116 MeV.

5. Through 7 Side-Coupled Cavities they are accelerated to 401.5 MeV.

6. The hydrogen ions pass through a carbon foil and the electrons are stripped, resulting in a proton beam that is passed to the circular Booster.

7. The Booster of radius 475 meters boosts the protons to 8 GeV and groups the protons into discrete bunches before injecting them into the Main Ring.

8. The Main Ring synchrotron accelerates the bunches of protons up to 150 GeV.

The Main Ring also delivers 120 GeV proton beams to a target to produce anti-protons. The anti-protons are debunched and stored in the Accumulator Ring for later injection back into the Main Ring.

10

After sufficient anti-protons are accumulated, the process of injecting beams into Tevatron begins. Tevatron is a synchrotron located in the same tunnel with the Main Ring, equipped with superconducting magnets for bending and/or focusing proton and anti-proton beams. At first, six bunches of 150 GeV protons are injected from Main Ring into Tevatron one by one. Then anti-protons are injected from anti-proton accumulator into Main Ring, accelerated to 150 GeV, and injected into Tevatron in 6 bunches. Six proton bunches and six anti-proton bunches circulate in opposite directions in the same Tevatron beam pipe, and are accelerated to 900 GeV simultaneously, and collide at the B0 and D0 interaction regions. The CDF detector is located at the B0 interaction point, as shown in Figure 2.1 (The D0 interaction point is not shown). The Switchyard in Figure 2.1 is used to split beams to different fixed-target experiments. It is not used during collider runs.

2.2 The CDF Detector

The CDF detector is a general-purpose detector for studying various particle physics in $p\bar{p}$ collision, including QCD, electroweak, heavy flavor physics and searches of "exotic" particles like SUSY particles, leptoquarks..., etc. It has forward-backward symmetry and approximate azimuthal symmetry. Figure 2.2 shows the side view of the detector.

The coordinate system used in CDF is also shown in Figure 2.2. The z axis is parallel to the proton direction, the y axis is vertical pointing upward, and x axis is simply $\hat{y} \times \hat{z}$. The angular coordinates that are commonly used in CDF are η and ϕ. ϕ is the ordinary azimuthal angle with $\phi = 0$ coincides with x axis. η is the *pseudorapidity* defined as

$$\eta \equiv -\ln(\tan\frac{\theta}{2})$$

where θ is the polar angle with respect to the z axis. The main reason of using η instead of θ is that for high energy particles satisfying $E \gg m$, η is approximately equal to rapidity y, defined as

$$y \equiv \frac{1}{2}\ln(\frac{E + P_z}{E - P_z}).$$

11
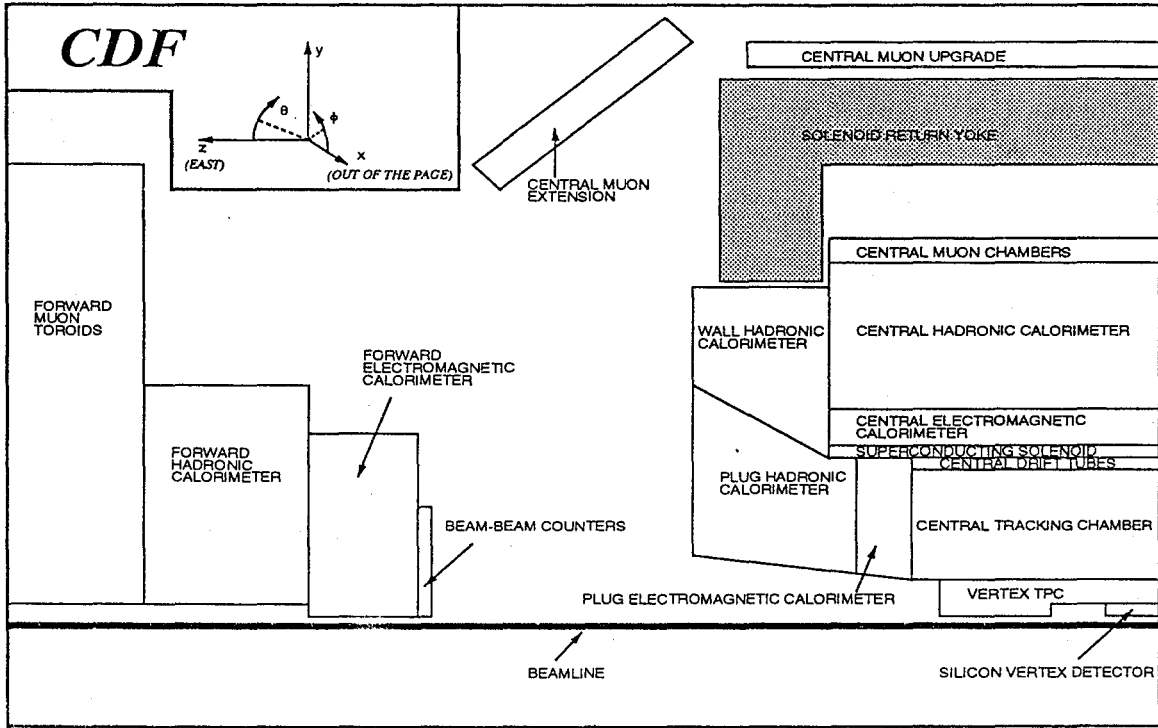
Figure 2.2: Side view of the CDF detectors.

It can be shown that rapidity distribution dN/dy is invariant under Lorentz transformation[25], and provides a better coordinate than θ.

The CDF detector system consists of 3 major parts: tracking system, calorimeter system and muon system. They are described in the following sections.

2.2.1 The Tracking Systems

There are 3 tracking detectors in CDF for measuring charges and momenta of charged particles: silicon vertex detector (SVX)[26, 27], vertex drift chamber (VTX)[28] and central tracking chamber (CTC)[29]. All tracking systems are immersed in a 1.4 Tesla magnetic field generated by a superconducting solenoid.

A charged particle that comes out of nominal collision point usually passes through SVX, VTX and CTC detectors before it hits the calorimeters. It can deposit energy in the depleted bulk silicon
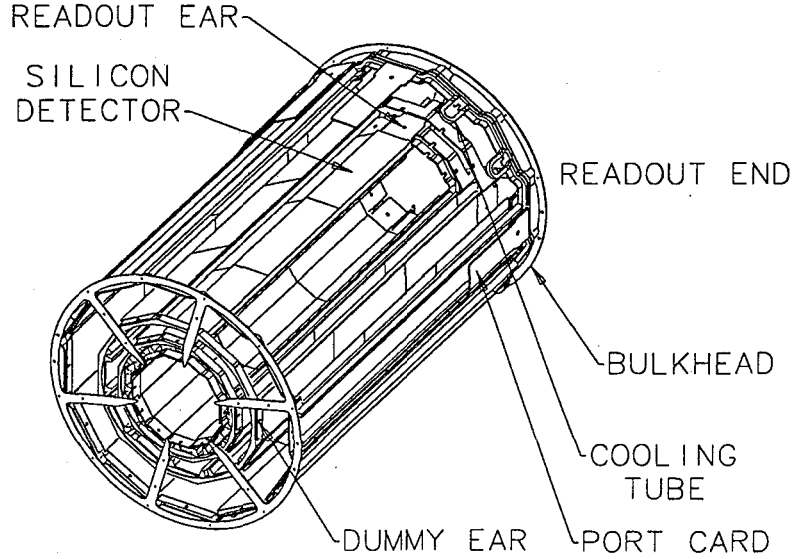
Figure 2.3: A 3-dimensional view of one barrel of the SVX detector.

and generates electron-hole pairs, and induces a signal. A typical minimum-ionizing particle creates about 20 000 electron-hole pairs in the bulk silicon. When passing through VTX and CTC, it ionizes gas molecules and the movement of gas ions and electrons in the electric field induces an electrical signal. Those spatial signals can be combined into a track to represent the trajectory of the particle. The trajectory is a helix because of the largely axial magnetic field. The momentum of the particle is measured from the curvature, azimuthal angle and polar angle of the helix.

The SVX detector consists of 4 layers of silicon wafers with equally spaced metal strips running in the z direction to measure the position of the tracks in $r - \phi$ plane. Because of its small pitch (50μmand 60μm), physicists in CDF are able to reconstruct the decay vertex of some short-lived particles like B mesons and D mesons. This has been a critical device for top quark physics in the lepton+jets channel. A 3-dimensional view of the SVX detector is shown in figure 2.3.

The SVX is mounted inside the VTX detector which has a pseudo rapidity coverage of $|\eta| < 3.25$.

VTX is the device for identifying event vertex in z axis. It has 8 modules of gas chambers, each module has 8 wedges. The wires in the end of each module provides (x, y) coordinates of the ionized charges, and the arrival time of the signal divided by the drift velocity gives a measurement of the z coordinate of the position that ionization occurs. Ionization points are connected to form track candidates, and track candidates are joined to form vertex candidates. The resolution of z coordinate of vertices is about 1 mm.

The outermost tracker is CTC, a 3.2 meter long cylindrical drift chamber whose 132 cm outer radius gives the largest leverage in fitting tracks. The open cell geometry represents minimum amount of material for particles, thus minimizes effects of multiple scattering.

The 84 layers of sense wires are grouped into 5 axial superlayers and 4 stereo superlayers interlaced with each other. The structure is shown in Figure 2.4. Starting with the vertex candidates found by VTX, the axial superlayers provide tracking in $r - \phi$ plane and stereo superlayers provide $r - z$ information.

We list some parameters of these 3 trackers along with parameters of the solenoid in Table 2.1.

2.2.2   Calorimeter System

Outside the solenoid enclosing the tracking system is the central calorimeter system. The plug and forward calorimeters cover ranges of smaller angles with respect to the beam. In each region (central, plug and forward) there are electromagnetic as well as hadronic calorimeters.

In the central region ($|\eta| < 1.0$) there are central electromagnetic calorimeter (CEM)[30], central hadronic calorimeter (CHA) and wall hadronic calorimeter (WHA)[31]. See Figure 2.2 for the positions of central calorimeters in the CDF detector system.

Charged particles with momenta greater than 350 MeV/c in the central region can pass through CTC. If they are not absorbed by the solenoid they can reach CEM. The central calorimeters consists of 24 identical wedges covering 15° each in ϕ, with $\sim$ 1.5° cracks between adjacent wedges. Each

14

	Two identical barrels × 12 identical wedges × 4 layers. Total length in Z = 51 cm.				
SVX	Layer	0	1	2	3
	Distance to Nominal Beam Line	3.0 cm	4.2 cm	5.7 cm	7.9 cm
	Pitch	60 μm	60 μm	60 μm	55 μm
	Number of Channels	256	384	512	768
	Single-hit Resolution in Data	13 μm			
	Impact Param. Resolution	17 μm			
	Signal to Noise ratio	9 → 6			
VTX	Outer Radius	22 cm			
	η Coverage	± 3.25			
	Z Vertex Resolution	1 mm			
	Gas	50% argon + 50% ethane + 0.7% isopropyl.			
	Drift velocity	46 μm/ns			
CTC	Inner Radius	28 cm			
	Outer Radius	132 cm			
	# of Axial Sense Wires	60 (5 superlayers)			
	# of ±3° Stereo Sense Wires	24 (4 superlayers)			
	Momentum resolution	$\approx 0.002 P_T$			
	CTC+SVX Momentum resolution	$[(0.0009 P_T)^2 + (0.0066)^2]^{1/2}$			
Solenoid	Length	4.8 m			
	Radius	1.5 m			
	Field Strength	1.4 Tesla			
	Current	4650 A			

Table 2.1: Some parameters of CDF tracking system.

— 554.00 mm I.D.

2760.00 mm O.D.
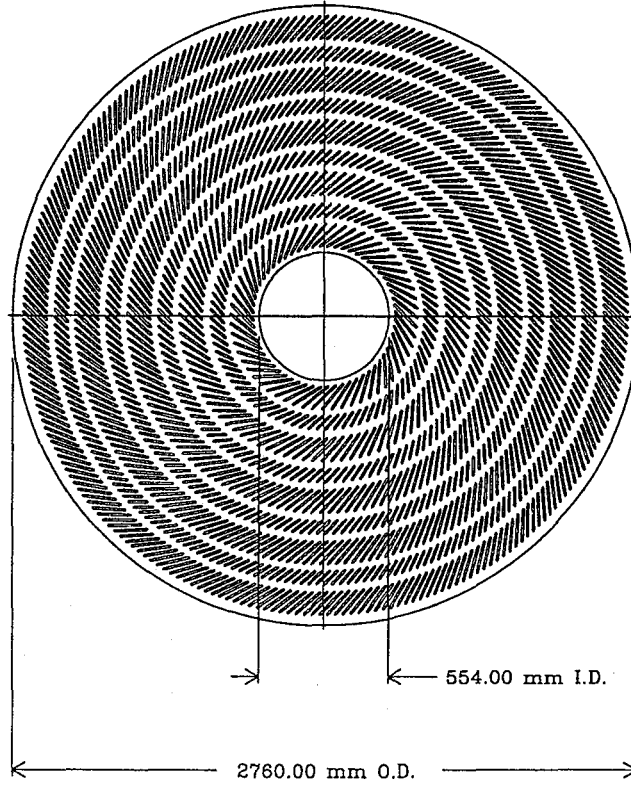
Figure 2.4: The end view of CTC showing the structure of 9 superlayers.

wedge is divided equally in pseudo rapidity into 10 projective towers, each tower pointing back to the origin of CDF coordinate system, the nominal interaction point.

In order to measure the shower position in the calorimeters, the Central Electromagnetic Strip Detector (CES)[30] are sandwiched inside CEM at 6 radiation lengths deep which is approximately the shower maximum for electromagnetic showers. In CES there are sense wires and strips to measure the shower position in $r - \phi$ plane and $r - z$ plane, respectively. The position resolution is approximately 3 mm by 3 mm. Figure 2.5 shows one wedge of the calorimeter module including CEM and CES.

The central hadron calorimeters are physically installed in the same wedges as CEM, and has the same tower geometry as CEM.
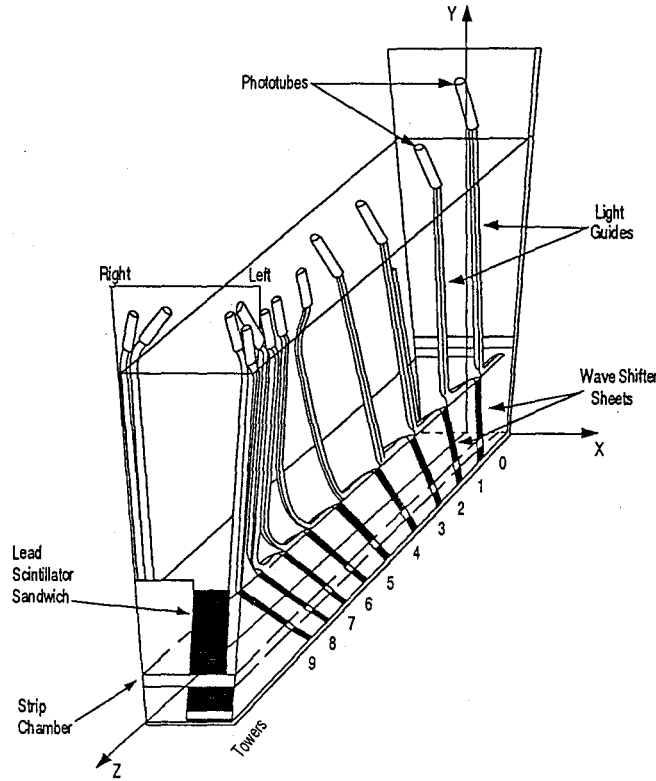
Figure 2.5: One wedge of the central calorimeter modules. The axes are draw along the CES chamber. The numbers label shows the projected tower structure of the modules, one tower per 0.1 in η.

We don't use plug and forward calorimeters so they are not described here. Interested readers are referred to References[32, 33, 34]. Some of the parameters of all calorimeters are listed in Table 2.2.

2.2.3 Muon Detectors

The calorimeters in central, plug and forward region serve as hadron absorbers for muon detectors. In the central region there are 3 muon chambers: Central Muon Detector (CMU)[35], Central Muon Upgrade (CMP), and Central Muon Extension (CMX). In the η region covered by end plug and forward calorimeters, Forward Muon Detector (FMU)[36] detects the muons.

A central muon with P_T above $\sim$ 1.5 GeV/c can usually survive the dE/dx interactions in the

System	Tower size	η Range	Absorber	Medium	Depth	Energy Resolution
CEM	$15° \times 0.1$	$|\eta| < 1.1$	Lead	Scint.	$18 \, X_0$	$13.7\%/\sqrt{E_T} \oplus 2\%$
CHA	$15° \times 0.1$	$|\eta| < 0.9$	Iron	Scint.	$4.5 \, \lambda_0$	$50\%/\sqrt{E_T} \oplus 3\%$
WHA	$15° \times 0.1$	$0.7 < |\eta| < 1.3$	Iron	Scint.	$4.5 \, \lambda_0$	$75\%/\sqrt{E} \oplus 4\%$
PEM	$5° \times 0.1$	$1.1 < |\eta| < 2.4$	Lead	Gas	$18\text{-}21 \, X_0$	$22\%/\sqrt{E} \oplus 2\%$
PHA	$5° \times 0.1$	$1.3 < |\eta| < 2.4$	Iron	Gas	$5.7 \, \lambda_0$	$106\%/\sqrt{E} \oplus 6\%$
FEM	$5° \times 0.1$	$2.2 < |\eta| < 4.2$	Lead	Gas	$25 \, X_0$	$26\%/\sqrt{E} \oplus 2\%$
FHA	$5° \times 0.1$	$2.4 < |\eta| < 4.2$	Iron	Gas	$7.7 \, \lambda_0$	$137\%/\sqrt{E} \oplus 3\%$

Table 2.2: Some parameters of CDF calorimeters.

solenoid and calorimeters and reaches the CMU. The CMU is also installed in the same wedges as CEM and CHA, but the ϕ coverage is somewhat smaller: $12.6°$. See Figure 2.6 for a schematic view of CMU in the central calorimeter wedge.

The CMU has 3 towers in each wedge $\times$ 4 layers per tower $\times$ 4 cells per layer. See Figure 2.7 for a transverse view. Each cell has one sense wire in the center which is used to determine the position of the track from the drift time of electrons. Four layers of cells with interleaving sense wires shifted horizontally by 2mm is used to resolve the left-right ambiguity.

In order to reduce the rate of fake muons from hadron punch-through effect, the CMP detector was installed prior to Run 1A with steel absorbers between CMU and CMP. For the top side and bottom side of the central detectors, the magnetic field return yoke serves as the absorber. On the left and right sides of the central detectors 2 steel walls of thicknesses 60 cm each were used. CMP also consists of 4 layers of single-wire cells, with scintillators mounted on the surface for precise timing.

The coverage of muons in (η, ϕ) space is extended by CMX to $0.6 < |\eta| < 1.0$. It consists of 4 layers of gas chambers sandwiched by scintillators for muon triggers.

The coverage of muon detectors are shown in Figure 2.8

The identification of a central muon is done by first forming muon stubs defined as straight lines connecting at least 3 out of 4 layers in each muon detector. So we can have CMU stubs, CMP stubs

18
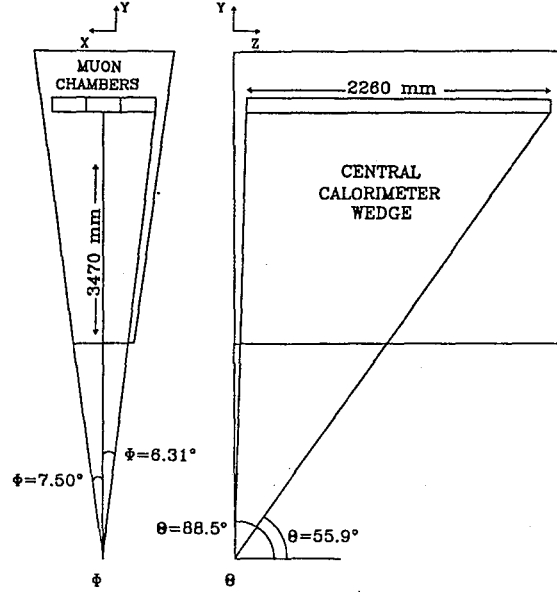
Figure 2.6: One wedge of the central muon detector. The three modules for each wedge is also shown.

and CMX stubs. And then CTC tracks are extrapolated to the surface of muon detectors and match to muon stubs. A matched stub can be considered a muon candidate, and the momentum of the candidate is the momentum of the CTC track.

Table 2.3 lists some parameters of CMU, CMP and CMX detectors.

2.2.4   Other Detectors

There are some other detector subsystems in CDF. The Central Pre-radiators (CPR) are proportional chambers located between the solenoid and CEM. They are used to sample the early development

Detector	Number of Layers	η Coverage	
CMU	4	84% of $|\eta| < 0.6$	53% of $|\eta| < 0.6$ is covered
CMP	4	63% of $|\eta| < 0.6$	by both CMU and CMP.
CMX	4	75% of $0.6 < |\eta| < 1.0$	

Table 2.3: Some parameters of the central muon detectors.
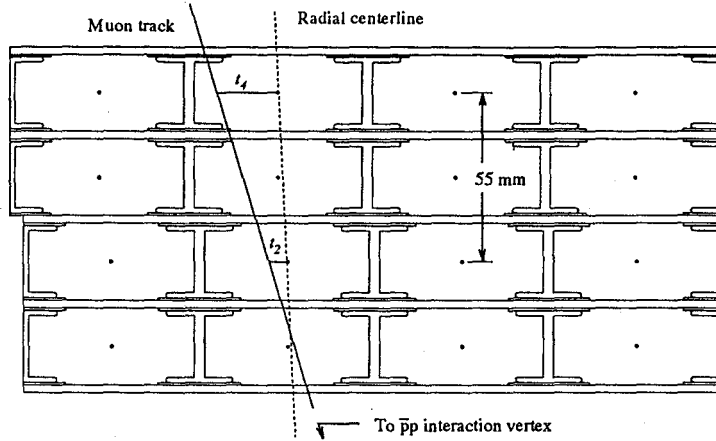
Figure 2.7: A transverse $(r - \phi)$ view of one CMU tower.

of showers in solenoid. The Beam-Beam Counters (BBC) are used to measure the instantaneous luminosity delivered by accelerator. They consist of 2 planes of scintillation counters covering the angular range of 0.32° to 4.47° in both forward and backward directions, or $3.2 < |\eta| < 5.9$. A coincidence requirement on both side of BBC serves as both a minimum bias trigger and the primary luminosity monitor. The rate of minimum bias triggers divided by the effective cross section gives a measurement of instantaneous luminosity.

CDF η-φ Map for Central Muons
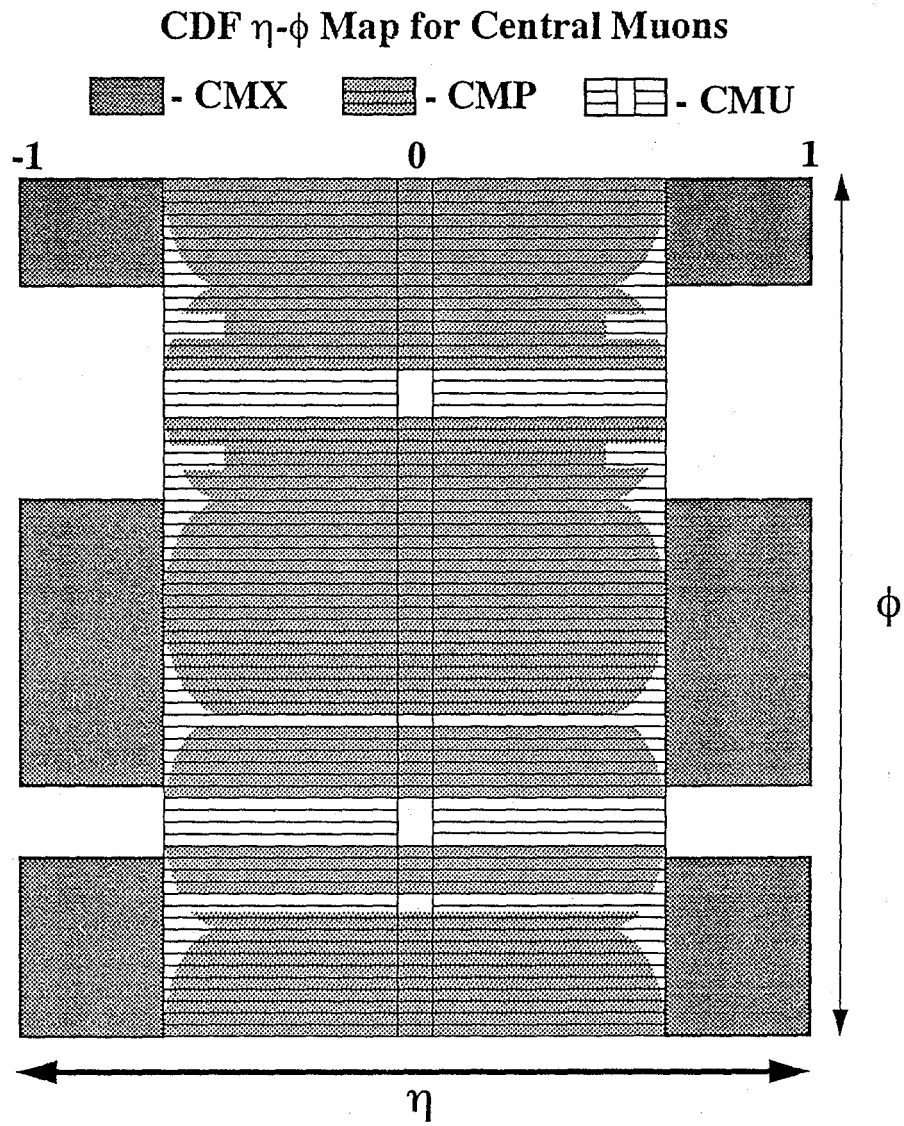
Figure 2.8: The coverage map of CDF central muon detectors CMU, CMP and CMX.

Chapter 3

CDF Data Path and Data Reconstruction

The interactions at the collision point produces lots of charged particles and neutral particles. The CDF detector detects traces that charged particles left in trackers and muon chambers and energies that particles deposit in calorimeters. To perform physical analysis those raw information have to be recorded on media and be constructed into a useful form. In this section we describe how data are handled in CDF.

3.1 The Trigger System

The beam crossing period of Tevatron in the course of Run 1 is 3.5 μs. In other words, the rate is $\approx$ 286 kHz. The effective cross section of CDF detector is about 70 mb, and the typical instantaneous luminosity delivered to CDF is about 5×10^{30} sec^{-1} cm^{-2}. Multiply these numbers together we get $\approx$ 1.2 events per crossing, or 343 K events/sec.

Given the complexity of CDF detectors and the nature of abundance of tracks and jets in $p\bar{p}$ collision, the average raw data size is about 100 KBytes. If we are going to record every event, it would take a bandwidth of 34 GB/s, which is very hard to achieve at the moment. And the biggest bottleneck is on the recording. In current technology tape drive can write approximately 500 KBytes per second. That's far from 34 GB/s. Thus, it is the formidable task to select 1 out of every 50 to

75 thousand events that has to be done by a trigger system.

The CDF trigger system consists of three levels. The first two are specially designed hardwares which make the decision to initiate the full detector readout[37]. The third level is a small-scale software processor farm[38].

The basic idea behind the multi-level trigger system is to have a chance to see every event yet record only interested event at the handleable rate with as little bias as possible. The lowest level should be fast to reduce dead time. The highest level should be sophisticated to determine whether or not a given event is interesting.

3.1.1 Level 1

The level-1 system should make decision within $3.5\mu s$ in order to be deadtimeless. By that time no digitized data can be available, so a separate analog data path is used to provide information to level-1 trigger system. Three major part of detectors provide information to level-1 hardware:

- Beam-Beam Counters: There are 2 time gates in BBC, the first one is timed for incoming beam halo particles while the second coincides with the time at which outgoing particles from a beam-beam interaction penetrate the counters. The first gate is useful for rejecting beam halo. The second provides CDF a minimum bias trigger.

  The difference of timing signal from the east and west BBC is used to find the beam-beam interaction point. With the timing resolution of 200 psec, the resolution of interaction point is about 10 cm, which is a good information in trigger time.

- Calorimeters: The calorimeter towers are grouped into trigger towers of size $\Delta\phi \times \Delta\eta = 15° \times 0.2$ to reduce the number of channels. The total energy deposition in each trigger tower is then weighted by a factor of $\sin\theta$ to calculate the transverse energy E_T. The reason to use transverse energy rather than energy is that in hadron colliders the total energy and momentum in the transverse plane is conserved, but not in the z direction. Then trigger towers with E_T above a

pre-programmed threshold are used to form 3 sums of energies: sum of E_T, sum of E_T weighted by $\cos\phi$ and sum of E_T weighted by $\sin\phi$. Here θ and ϕ are from the position of the tower and is fixed for each trigger tower. Then those 3 tower-by-tower sums are added together to form 3 sums for each calorimeter system (central/plug/forward, EM/HAD) and digitized into 10 bits integers. Finally a Level 1 Sum is performed to get sum E_T and missing E_T in the trigger level. Those are essentially the basic information for triggering events with electrons, photons or jets.

- Muon Detectors[39]: The difference in drift time in the 4 layers of CMU and CMX provides information about the incident angle of a track into the chamber. For CMU the angle is equal to $0.14 P_T^{-1}$. This gives a rough estimate of muon transverse momentum. An upper cut of time difference is equivalent to a P_T threshold in level 1 trigger.

The level-1 trigger rate is roughly 1 kHz at typical luminosity of 5×10^{30} cm^{-2} sec^{-1}.

3.1.2   Level 2

The decision making process is sent to level 2 for an event that passes level 1 triggers.

The level 2 trigger system is a set of specially configured hardware. In level 2, several other computations are performed:

- Calorimeter *clusters* are formed by a hardware nearest-neighbor cluster finder and E_T, average η and average ϕ of each cluster are re-calculated because those values in level 1 might be from analog signals that are not totally settled.

- R-ϕ tracks are found by the hardware Central Fast Tracker (CFT) with efficiency 93.5±0.3% and resolution $\delta P_T/P_T \approx 0.035 P_T$ for tracks above 10 GeV/c.

- Highly electromagnetic calorimeter clusters are matched to CFT tracks to form electron candidates.

- CMU, CMP and CMX track-segments are found and matched to CFT tracks to form muon candidates.

At the typical luminosity of 5×10^{30} cm^{-2} sec^{-1} the level-2 output rate is ≈ 12 Hz.

3.1.3 Level 3

After an event has passed level 2 triggers the DAQ system is asked to read out the whole event into level 3 for further processing. The level 3 trigger system consists of 4 commercial computers (Silicon Graphics Challenge) with 8 CPUs each. In level-3 the event is reconstructed by the same algorithm used in off-line data production, but with less precise data. The output rate is about 5 Hz, and the events are stored in 8mm magnetic tapes for off-line processing.

3.2   The Data Reconstruction

The raw data can't be used for physics analysis. They need to be reconstructed so physicists can identify electrons, muons, photons, jets, ... etc. In off-line data reconstruction the identification criteria are very loose to keep high efficiency. The reconstruction algorithms are described below.

3.2.1   Vertex Reconstruction

VTX hits are first connected into VTX track segments. In order not to miss the true track the connection process is done loosely. Then the VTX segments are pointed to beam line and intersections are found. Each intersection, or vertex, is associated with a class word classifying its quality. A vertex has higher class if there are more VTX segments pointing to it. The highest class is 12, marking a very good vertex candidate.

3.2.2 Track Reconstruction

CTC tracks are formed by a road-finder algorithm starting from the outer-most superlayer (superlayer 8). This is the most time-consuming part of data reconstruction.

3.2.3 Jet Reconstruction

High energy partons in the final state of a collision can create lots of partons from vacuum via the color field and eventually form colorless baryons or mesons. The colorless particles can decay or emit some radiations to produce more particles along its path. This is the *fragmentation* process. Most of the particles produced in the fragmentation go along the direction of the original parton. The narrow flow of particles is called a *jet*.

Particles inside the same jet mostly hit a small area of calorimeter and make a cluster of fired calorimeter towers. Therefore, the identification of a high energy parton is often equivalent to the identification of calorimeter clusters.

Calorimeter towers (both EM and HAD) are addressed in $\eta - \phi$ space. The "distance" between 2 towers with addresses (η_1, ϕ_1) and (η_2, ϕ_2) is defined as

$$R = \sqrt{(\eta_1 - \eta_2)^2 + (\phi_1 - \phi_2)^2}$$

with ϕ measured in radians. Nearby towers are grouped into clusters by a fixed-cone clustering algorithm. The algorithm is as follows:

1. Make a list of towers with energy above threshold, and sort them by decreasing energy.

2. The first tower, i.e., the tower with the highest energy, forms the "seed" of the first cluster.

3. Loop over all the rest of towers in the list. For each tower, find the closest seed.

4. If the distance to the closest seed is less than the cone size and the tower is adjacent to at least one tower in the cluster, this tower is merged into the cluster.

5. Otherwise the tower forms the seed of a new cluster.

In CDF, 3 cone sizes are used: 0.4, 0.7 and 1.0.

3.2.4 Electron and Photon Reconstruction

The electrons and photons typically are absorbed in the electromagnetic calorimeters and small amount of energy can leak into the hadronic calorimeters. They both form clusters in electromagnetic calorimeters. The only differences are on the track requirement and shower development. There are no tracks for a photon, while there are at least one track for an electron. The EM calorimeters are not fine enough to really distinguish electron showers from photon showers in a very high efficiency. Thus in CDF electrons and photons are reconstructed in the same way by looking at EM clusters and put track requirement at a later stage. The clusters are formed by a similar algorithm as jet reconstruction, but working on EM clusters and the cluster size is restricted to be no larger than 3 towers in pseudo rapidity ($\Delta\eta = 0.3$) by one tower in azimuth ($\Delta\phi = 15°$) in the central region. Other requirements are:

- Seed tower EM $E_T > 3$ GeV.

- non-seed towers in clusters EM $E_T > 0.1$ GeV.

- total EM E_T of a cluster > 5 GeV.

- $\dfrac{\text{Hadronic } E_T}{\text{EM } E_T} < 0.125$.

3.2.5 Muon Reconstruction

Hits in different layers of muon chambers are connected to form stubs. And CTC tracks are propagated to the surface of muon chambers. A match between stubs and tracks forms a muon candidate.

3.2.6 Missing E_T Reconstruction

Energy of all calorimeter towers are summed in the following fashion

$$(E_x, E_y) = \sum_i E_i(\cos \phi_i, \sin \phi_i)$$

to get the imbalance of energy in the transverse plane in the event. $\vec{\not{E}}_T$ is defined as $(-E_x, -E_y)$.

3.3 The Data Production

In previous section we've briefly discussed how data are reconstructed. In this section we describe the data production, i.e., the process of reconstructing all raw data.

In the course of Run 1B (Nov 1993 to July 1995), CDF has recorded roughly 56 million events. Due to the abundance of tracks in $p\bar{p}$ collisions and the large number of channels of the CDF detector, the average size of one event is approximately 100 Kilo bytes. That amounts to ≈ 5.6 Tera bytes of raw data. The raw data are stored on 1580 8mm magnetic tapes.

The primary physics goal in CDF in Run 1 is top quark search. Since the cross section of top quark production is expected to be small, the trigger rate is low, and an "express" data stream is designed to see interesting events, especially top candidates, on the day that it is recorded. The level 3 system filters out all events with high P_T electrons, muons, jets, missing transverse energies, ... etc. Those events are written to hard disks as well as tapes and are reconstructed within 10 hours of data taking, and the reconstructed events are stored on a set of express disks so physicists in CDF can analyze the fresh events right away.

To reconstruct all recorded raw data in a reasonable pace with the online data taking while maintaining the express stream is a big challenge in data production. It requires lots of CPU power and high I/O speed. As of the year of 1993, it takes about 20 seconds for an average workstation on the market to reconstruct one typical CDF event. Which means it would take about 35.5 CPU years to reconstruct all CDF data taken in the 1.5 years of Run 1B.

The rule of thumb to speed up data production is to use a lot of workstations and make them work together. That has been the method adopted by both CDF and D0 collaborations. CDF uses two "*farms*" of totally 101 networked workstations to do the job. Each farm has its own input server to read raw data from tapes and sends events to workstations (called "worker nodes") for reconstruction. After an event is reconstructed by a worker node it is sent to the output server. The output server assembles reconstructed events sent from all worker nodes and store them on disks. A second process is used to split data into separate physics "streams" before copying them to tapes. This way a physicist interested in J/ψ physics doesn't need to go through all 56 million events to make his/her data sample, he/she only needs to use tapes of J/ψ stream and all J/ψ events that are triggered are in the stream already.

CDF used roughly 6200 tapes for reconstructed data in Run 1B.

3.4   The Measurements of Properties of Objects

3.4.1   The Charge and Momenta of Charged Particles

As stated in previous sections, the momentum of a charged particle is measured from the curvature of the CTC track. The charge is measured from the sign of the curvature.

For prompt particles, i.e., particles that come directly from $p\bar{p}$ collisions, the vertex on the beam line provides another data point for fitting the helix. Because of the long leverage arm of this point (remember that the inner radius of CTC is 28 cm and the average distance between 2 adjacent CTC superlayers is 13 cm), the resolution is enhanced. Momentum measured in this way is called "beam-constrained momentum."

The SVX can improve the momentum resolution further. A charged particle that passes through fiducial volume of SVX typically leaves 3 or 4 hits in 4 layers of SVX ladders. The resolution of hit position is in the order of 10 μm. Those 3 or 4 hits enhances the momentum resolution.

3.4.2 The Charge and Momenta of Muons

The charge and momentum of a muon is assigned as the charge and momentum of the CTC track that matches to the muon stub. Since muons seldom undergo bremsstrahlung the track momentum is a good measure of muon momentum at the collision point.

3.4.3 The Charge and Momenta of Electrons

The bremsstrahlung effect of an electron is severe because of its small mass, and it often change direction and become softer before it hits the calorimeters. This means the track momentum is not a reliable measure of electron momentum. However, since the photons radiated from an electron tend to go along the electron, the photons have a good chance of hitting the same calorimeter tower with the electron.

Sometimes the radiated photon can convert into an e^+e^- pair when it hits high mass regions of the detector like the inner wall of CTC, and end up with 2 tracks along the original electron track. Therefore, an electron can make more than one tracks. Most of those tracks would hit the same EM calorimeter tower. The tracks that are bent out by magnetic fields and miss the tower are very soft and doesn't affect the energy measurement much.

So we can use the cluster energy measured in EM calorimeters as the energy and momentum of the electron, neglecting the tiny electron mass. The direction of the electron momentum is measured from the direction from event vertex to the EM cluster.

The charge of the electron is measured from the CTC tracks. Among all tracks that hits the EM cluster, we select the track that has the highest transverse momentum as the primary electron track, and assign its charge as the charge of the electron.

30

3.4.4 Momenta of Final State Partons — Jet Energy Correction

There can be lots of different particles in a jet which usually is the result of hadronization of a parton. Most of the particles inside a jet are hadrons and are absorbed by calorimeters. Some of them decay before reaching the calorimeters, and producing leptons at times. Some of them are charged and leave a track in tracking system and be bent by the magnetic field. Therefore, even with an ideal calorimeter the muons and neutrinos in a jet are not captured by calorimeters and the energy deposited in calorimeter inside a clustering cone can be smaller than the energy of the original parton.

Besides muons and neutrinos, there are other reasons why the jet energy measured in a real world calorimeter is not equal to the parton energy:

- Non-linear responses of calorimeters with respect to the energy that is deposited.

- Presence of cracks or holes between adjacent calorimeter towers: particles can go into a crack and don't leave significant amount of energies in calorimeters.

- Soft charged particles: they can be bent outside the clustering cone by the magnetic field.

- Soft gluon radiations: soft gluons can be radiated off a parton and the gluon can go outside the clustering cone.

- Underlying events from the the soft process in the same $p\bar{p}$ collision: those mostly soft processes can generate particles that hit calorimeters and add energies to clusters.

- Underlying events from extra vertices: When more than 1 $p\bar{p}$ collision occur in one beam crossing, the extra vertices also generate particles and add energies into clusters.

- Different calorimeter responses: not all calorimeter modules are created equal.

Based on the above facts, a jet energy correction is needed to map as close as possible the measured energy in calorimeters to the energy of the parton that originates the jet.

In CDF, the jet energy correction is done off-line. There are several different corrections done for correcting the energy of a jet:

1. **Relative correction:** This is used to compensate the difference among different calorimeter modules and the effect of cracks. The jet P_T is multiplied by a factor f_{rel} to obtain the equivalent P_T that would be recorded if the jet hits central calorimeters. The factor f_{rel} is a function of detector η and jet P_T.

2. **Absolute correction:** This correction estimates parton P_T for a given clustering cone size and a measured P_T. This is primarily correcting the nonlinear response of the calorimeter to low momentum particles.

3. **Underlying event correction:** Subtract the estimated energy deposition from underlying events. Average contributions from both extra vertices and the event vertex are subtracted.

4. **Out of cone correction:** This adds back the average energy leak outside the clustering cone from the soft gluon radiations and soft charged particles.

The actual steps are revealed in more detail below. Here we use P_T as the transverse momentum of the jet in question, f_{EM} as the electromagnetic fraction of the jet energy, i.e., $E_{EM}/(E_{EM}+E_{HAD})$, and N_V as the total number of event vertices. The operator $+=$ means "is increased by," $\times=$ means "is multiplied by," ... and so on.

Step 1.	P_T	$+=$ $P_T \times f_{EM} \times \Delta S_{EM}$	$\cdots$ EM scale change in Run 1
Step 2.	P_T	$\times=$ $f_{rel}(\eta, P_T)$	$\cdots$ relative correction
Step 3.	P_T	$-=$ $\max(N_V\text{-}1,0) \times p_1^{ue}$	$\cdots$ underlying event from extra vertices
Step 4.	P_T	$\leftarrow$ $a_0 + a_1 P_T + a_2 P_T^2$	$\cdots$ absolute correction
Step 5.	P_T	$-=$ p_2^{ue}	$\cdots$ underlying event from the same vertex
Step 6.	P_T	$+=$ p^{oc}	$\cdots$ out of cone correction

ΔS_{EM} is the scale shift of central electromagnetic calorimeter during Run 1A and Run 1B with

respect to Run 0 (1988/89). It is estimated to be[40]

$$\begin{cases} 0 & \text{for non-central jets,} \\ 4.5\% & \text{for Run 1A central jets,} \\ 4.9\% & \text{for Run 1B central jets.} \end{cases}$$

The relative correction factor $f_{rel}(\eta, P_T)$ is obtained from dijet data with at least one jet in the region of $0.2 < |\eta| < 0.7$ and no 3rd jet with $P_T > 15$ GeV/c. By demanding that P_T of the non-central jet is equal to P_T of the central jet $f_{rel}(\eta, P_T)$ can be obtained from the ratio of P_T. In region $0.2 < |\eta| < 0.7$ f_{rel} is close to 1 since this is where the relative correction is based. For central region $-0.2 < \eta < 0.2$ f_{rel} is 12% to 25% for raw $P_T = 20$ GeV/c to 100 GeV/c. The relatively large f_{rel} is from the large crack at z=0. Near $|\eta| = 1.1$ and $|\eta| = 2.4$ the correction is also large because of the central-plug crack and plug-forward crack.

p_1^{ue}, the average energy deposited in the clustering cone per class 12 vertex, is measured in minimum-bias data and W + 0 jets data[41]. In the minimum bias sample, the average raw energy inside a clustering cone in the central calorimeter is measured as a function of number of vertices. In the W + 0 jets sample where no jets has $P_T > 10$ GeV/c, the raw energy of a clustering cone opposite to the W electron or muon is measured also as a function of number of vertices. These two functions are consistent with each other and are linear in number of vertices. Thus p_1^{ue} is derived from the slope of the linear function. This correction is done after relative correction because it is derived from central calorimeters. The result of p_1^{ue} is 0.297 GeV per extra vertex for cone size 0.4.

The coefficients for absolute energy correction a_0, a_1 and a_2 are derived from Monte Carlo samples[42]. Pairs of partons with a flat P_T spectrum in the range $2 < P_T < 700$ GeV/c and $|\eta| < 1.2$ are generated and passed to ISAJET fragmentation routine which has been tuned to agree with the charged particle fragmentation observed in data from 1988/89 collider run. Then the CDF detector simulation QFL version 3.20 is used to simulate the event, and finally clustering algorithm is applied to form jets. A jet is said to match to a parton if $\sqrt{(\eta_{parton} - \eta_{jet})^2 + (\phi_{parton} - \phi_{jet})^2} < 0.5$. The coefficients a_0, a_1 and a_2 are obtained by fitting the scatter plot of parton P_T vs jet P_T to double quadratic function

33

with break point at 100 GeV/c. The result for cone size 0.4 is

$$a_0 = 1.37, a_1 = 1.1946, a_2 = -0.0008724 \qquad \text{for } P_T < 100 \text{ GeV/c,}$$

and

$$a_0 = -4.03, a_1 = 1.1794, a_2 = -0.0001815 \qquad \text{for } P_T > 100 \text{ GeV/c.}$$

p_2^{ue}, the underlying event contributions from the same event vertex, is obtained from the same minimum bias data as p_1^{ue}. It is the average post-correction energy deposited in the clustering cone when there is only 1 vertex.

p^{oc}, the out-of-cone energy correction, is derived from the same Monte Carlo samples[42] by counting particles outside the clustering cone and sum up their energies. A fit of the form

$$b_0(1 - b_1 \exp(-b_2 P_T))$$

is used on the scatter plot of average out-of-cone P_T vs jet P_T, and the result for cone size 0.4 is $b_0 = 22.999, b_1 = 0.915,$ and $b_2 = 0.00740$.

Chapter 4

Data Selection

The dilepton channel of top analysis is from the process

$$p\bar{p} \to t\bar{t}X \to W^+bW^-\bar{b}X \to \ell^+\ell^-\nu\bar{\nu}b\bar{b}X$$

where the 2 leptons can be either muons or electrons. The signature of this channel is 2 opposite signed leptons, at least 2 jets and large missing transverse energy from the 2 neutrinos. The event selection starts by filtering out events with 2 leptons satisfying the lepton identification cuts. In order to increase acceptance we define a set of looser identification cuts and we accept events with one standard lepton and one loose lepton. A series of kinematical cuts as well as $\rlap{/}{E}_T$ cut and dijet cut are applied on the filtered sample.

In this chapter we describe the cuts used to select candidate events.

4.1 Electron Identification

We only consider central electrons because in the plug and forward region the noise level is too high and the coverage of CTC doesn't go to large η. The other reason is that most leptons from $t\bar{t}$ events are in the central region. The concept of electron identification is rather straight-forward:

- We start with a fiducial EM calorimeter cluster with at least one track pointing to it. We assign the track with highest P_T among all associated tracks as the "electron" track. This track must

survive photon conversion test.

- We require that the energy deposited in hadronic calorimeters in the same cluster is much lower than its EM part to reject hadronic jets.

- We require that the energy deposited in calorimeter and the momentum of the track be consistent with each other to reject backgrounds like π^0 + tracks.

- We require that the intersection point of the track extrapolated to the surface of CES is close to the geometric center of CES shower profile.

- We require that the measured shower profile in CES fits expected shape. We use the χ^2 of the fit to determine whether or not the fit is good.

- We require that the lateral shower profile in calorimeter is consistent with electron test beam results. We define a variable L_{shr} which compares the energy of neighboring towers with the expected energy deposition from test beam electrons. It is defined as

$$L_{shr} = 0.14 \times \frac{E_{side} - E_{side}^{exp}}{\left[\left(0.14\sqrt{E_{total}}\right)^2 + \sigma^2(E_{side}^{exp})\right]^{\frac{1}{2}}}$$

where

$$
\begin{aligned}
E_{side} &= \text{energy in the neighbor towers,} \\
E_{total} &= \text{total energy in the seed tower and neighbor towers,} \\
E_{side}^{exp} &= \text{expected energy in the neighbor towers as a function of } E_{total} \\
&\quad \text{derived from test beam data,} \\
0.14\sqrt{E_{total}} &= \text{the resolution of } E_{total}, \\
\sigma^2(E_{side}^{exp}) &= \text{Resolution of } E_{side}^{exp} \text{ derived from test beam data.}
\end{aligned}
$$

A large value of L_{shr} indicates a departure from expected response to electrons.

- Since the top quark is heavy, the electron should have high transverse momentum. So a threshold on E_T is applied.

- To be sure the electron is "prompt", i.e., directly from the vertex, we require that the electron track is close to the event vertex.

- We reject electrons from a vertex that is far from the geometric center of the detector.

The selected value of cuts for both standard and loose electrons are listed in Table 4.1.

Variable		Standard	Loose	unit
E_T	>	20	20	GeV
P_T	>	10	10	GeV/c
E/P	<	1.8	4.0	
E_{HAD}/E_{EM}	<	0.05	$0.055 + 0.045\,E/100$	
$|\Delta x|$	<	1.5	1.5	cm
$|\Delta z|$	<	3.0	3.0	cm
χ^2_{strip}	<	10	-	
L_{shr}	<	0.2	0.2	
$|\Delta z(\text{track-vertex})|$	<	5.0	5.0	cm
$|z(\text{vertex})|$	<	60	60	cm

Table 4.1: Central electron identification cuts.

4.2   Muon Identification

We only consider central muons, i.e., muons that hit CMU, CMP or CMX. In the region with no muon chamber coverage high quality tracks that pass a set of minimum ionizing cuts are considered loose muons, and are called central minimum ionizing particles (CMI). The concept behind muon identification is rather straight-forward, too.

- We start with a muon stub in CMU or CMP or CMX with one CTC track matching to it.

37

- Since a high energy muon leaves very little energy in calorimeters, we require the energy deposited in the calorimeter tower (both electromagnetic and hadronic) through which the extrapolated CTC track passes is consistent with the result of a minimum ionizing particle.

- To avoid noises in muon chambers or cosmic rays that accidentally match to a CTC track, we require that some energy is deposited in the calorimeter tower.

- Just like the electron, we have a threshold on transverse momentum.

- We require that the CTC track is from the beam-line so the muon is a prompt muon, not a muon from secondary decays. This is done by requiring a small impact parameter.

- For the loose muon which no muon stubs are present, we require that the quality of the CTC track is high by demanding number of fired superlayers in CTC exceed a certain value, and there is little activity in calorimeter and CTC in the vicinity of the CTC track. Quantitatively, we define two variables representing the isolation of the CTC track in a cone of 0.4 in (η, ϕ) space:

$$I_{trk} \equiv \sum_{\Delta R < 0.4} P_T(\text{tracks})/P_T(\text{CTC track}),$$
$$I_{cal} \equiv \sum_{\Delta R < 0.4} E_T(\text{calorimeter})/P_T(\text{CTC track}).$$

And we place an upper cut on those 2 variables.

The cuts for both standard and loose muons are listed in Table 4.2. In the table TCM (tight central muon) refers to muons that hit CMU or CMP or both chambers.

4.3 Jet Selection

After 2 leptons are identified, we proceed with jets selection. Since we are looking for $t\bar{t}$ events with heavy top quarks, the final state particles tend to be in the central region. We select jets with $|\eta| < 2.0$ and $E_T > 10$ GeV cuts where E_T is the *raw* jet energy obtained from calorimeters.

38

		TCM	CMX	CMI	unit
P_T	>	20	20	20	GeV/c
3D track		yes	yes	yes	
EM energy	<	2	2	2	GeV
HAD energy	<	6	6	6	GeV
EM+HAD energy	>	0.1	0.1	0.1	GeV
track |d0-v|	<	0.3	0.3	0.3	cm
track |Z0-v|	<	5	5	5	cm
stub matching	<	2|5	5	-	cm (2 for CMU, 5 for CMP)
Fiducial		-	-	yes(*)	
# of Axial SL	>	-	-	2	
# of Stereo SL	>	-	-	3	
total # of SL	>	-	-	6	
I_{cal}	<	-	-	0.1	
I_{trk}	<	-	-	0.1	

Table 4.2: Central muon identification cuts. (*) We require that the CMI hit the fiducial volume of calorimeters in order to have a meaningful measurement of its calorimeter energies which is crucial in the identification of CMIs.

4.4 Missing E_T Correction

The measurement of $\not{E}_T$ is obtained from the imbalance of transverse energies in calorimeters. However, it does not represent the missing transverse energy *at the collision point*, where the 2 neutrinos emerge. There are two main reasons:

1. The muons in the event don't leave much energy in calorimeters, but represents a big amount of transverse energy at the collision point.

2. The raw jet energies are not equal to parton energies.

It is straight-forward to correct $\not{E}_T$ for these two effects. To be precise, we do

$$\vec{\not{E}}_T' = \vec{\not{E}}_T + \sum_{jets}\left(\vec{E_T}^{raw} - \vec{E_T}^{cor}\right) + \sum_{muons}\left(\vec{E_T}^{calorimeter} - \vec{P_T}^{muon}\right)$$

In doing this correction, all good jets (i.e., not noises) and all good muons (not necessarily high P_T muons) should be used in the summation. We use all jets that is in the central or plug region ($|\eta| < 2.4$) with $E_T > 10$ GeV and all muons with $P_T > 15$ GeV which pass all identification cuts.

4.5 Kinematical Cuts

After an event has been identified with 2 leptons, we apply the following kinematical cuts:

- Opposite sign requirement. We reject same-sign dilepton events.

- Lepton isolation cuts. We require that at least one lepton that passes standard cuts is isolated. The isolation cut is

$$I_{cal} < 0.1 \quad \& \quad I_{trk} < 0.1.$$

- Invariant mass windows. We reject ee and $\mu\mu$ events with dilepton invariant mass $M_{\ell\ell}$ in the range $75 < M_{\ell\ell} < 105$ in order to reject $Z \to \ell^+\ell^-$ events.

- Missing transverse energy cut. We require $\not{E}_T > 25$ GeV. For events with $\not{E}_T < 50$ GeV, we also require the ϕ angle between $\not{E}_T$ and nearest jet or lepton be greater than 20 degrees to reject $Z \to \tau^+\tau^-$ events and events with a mis-measured jet.

- Di-jet requirement. We require that there are at least 2 jets that pass the jet selection.

4.6 Acceptance

The acceptance of $t\bar{t}$ events in the dilepton channel is defined as the fraction of $t\bar{t}$ events that pass the selections cuts described in previous sections. Since BR($t\bar{t} \to \ell^+\nu\ell^-\bar{\nu}b\bar{b}$) is roughly 5%, the acceptance is surely less than 5%. It has been estimated by using Monte Carlo $t\bar{t}$ samples[43] to be $0.0077 \pm 0.0002(stat.) \pm 0.0007(syst.)$.

4.7 Backgrounds

There are 2 categories of backgrounds in dilepton channel:

1. Physics Background

    (a) $W^+W^- + 2$ jets $+ \not{E}_T$.

    (b) $Z \to \tau^+\tau^- + 2$ jets $+ \not{E}_T$.

    (c) Drell-Yan $+ 2$ jets $+ \not{E}_T$.

2. Detector Effect Background: fake lepton background. This background is from events with one real lepton, 2 jets, high $\not{E}_T$ and a fake lepton.

The number of each type of backgrounds are estimated from data when possible.

4.7.1 Drell-Yan

Drell-Yan process is $q\bar{q} \to \genfrac{}{}{0pt}{}{Z^*}{\gamma^*} \to \ell^+\ell^-$ where Z^* and γ^* are the virtual bosons. Because the energy in Tevatron is high enough to create real Z bosons most ($\sim 90\%$) of Drell-Yan events are from the Z resonance.

The number of Drell-Yan $+$ dijet $+ \not{E}_T$ events is estimated in data[44, 45]. We calculate the fraction of events that pass $\not{E}_T$ cut and dijet cut in the Z mass window (75,105)

$$f(\not{E}_T + dijet) = \frac{N(Z \; dilepton + \not{E}_T + dijet)}{N(Z \; dilepton)}$$

and subtract the contribution from top events in the Z mass window estimated in Monte Carlo. We got $f(\not{E}_T + dijet) \approx 0.1\% \pm 0.05\%$. We assume the $\not{E}_T$ cut efficiency is independent of $M_{\ell^+\ell^-}$ and dijet cut efficiency is weakly dependent on $M_{\ell^+\ell^-}$. We correct $f(\not{E}_T + dijet)$ for this dependence and apply it to data events outside Z window to get the expected number of Drell-Yan events. After the correction we obtain

$$N(\text{Drell-Yan}) = 0.62 \pm 0.30.$$

41

4.7.2 Fakes

A fake event in the top dilepton channel is an event with one real lepton + one fake lepton + $\not{E}_T$ + 2 jets, where the fake lepton can be a jet which fakes an electron or a track which fakes a muon. The number of such events is estimated by first counting events with one real lepton, 2 jets, large $\not{E}_T$ and one more object that can probably fake a lepton, then multiply the number of such events by the probability that objects can fake real leptons[46, 47].

For fake electrons, we call a jet that is able to fake an electron a "denominator electron" because it is used as the denominator when calculating the fake probability. We define the denominator central electrons (DCE) as jets that pass a set of very loose electron identification cuts. In a similar way we have "denominator muons" which are tracks that have potential to mimic muons. Because we have 3 types of muons TCM/CMX/CMI, we have 3 types of denominator muons DCM/DMX/DMI. The cuts are listed in table 4.3 along with cuts for real leptons for comparison.

To measure the lepton fake probabilities we need a leptonless sample and count the number of denominator leptons and measure the fraction that they pass the real lepton cuts. The closest sample is the QCD jet sample where real leptons are mostly from heavy flavor (b or c) events. Without subtracting the heavy flavor contents we got an over-estimate of the fake probability of $\approx 0.2\%$ to 2% depending on categories and P_T of the denominator lepton. Multiplying the fake probabilities to the number of events that have one good lepton, one denominator lepton, dijet and $\not{E}_T$ we obtain

$$N(\text{fake}) = \begin{cases} 0.16 \pm 0.16 & e\mu \\ 0.21 \pm 0.17 & ee\&\mu\mu \end{cases}$$

4.7.3 $Z \to \tau^+ \tau^-$

This is the background from $p\bar{p} \to Z \to \tau^+\tau^- \to \ell^+\ell^-\nu's$. Since all leptons are much lighter than Z boson, the kinematics of $Z \to \tau^+\tau^-$ has essentially no difference with that of $Z \to \ell^+\ell^-$. To take advantage of this and avoid relying on Monte Carlo to model the kinematics, we use $Z \to e^+e^-$ data, replace e's by τ's with the same P_T and redecay the τ leptons to simulate the background[48]. The

Variable		DCE	LCE	TCE	
E_T	>	20	20	20	
P_T	>	10	10	10	
E/P	<	-	4.0	1.8	
HAD/EM	<	0.125	*	0.05	(*) $0.055 + 0.045 \times E/100$
|dx|	<	-	1.5	1.5	
|dz|	<	-	3.0	3.0	
Strip χ^2	<	-	-	10	
Lshr	<	-	0.2	0.2	
|Δz(track-vertex)|	<	-	5.0	5.0	
|z(vertex)|	<	-	60	60	

		DCM	TCM	DMX	CMX	DMI	CMI
P_T	>	20	20	20	20	20	20
3D track		yes	yes	yes	yes	yes	yes
EM energy	<	-	2	-	2	-	2
HAD energy	<	-	6	-	6	-	6
EM+HAD energy	>	0.1	0.1	0.1	0.1	0.1	0.1
track |d0-v|	<	-	0.3	-	0.3	-	0.3
track |Z0-v|	<	-	5	-	5	-	5
stub matching	<	2,5	2,5	5	5	-	-
Fiducial		-	-	-	-	yes	yes
# of Axial SL	>	-	-	-	-	3	3
# of Stereo SL	>	-	-	-	-	2	2
total # of SL	>	-	-	-	-	6	6
I_{cal}	<	-	-	-	-	0.1	0.1
I_{trk}	<	-	-	-	-	0.1	0.1

Table 4.3: Cuts used to select denominator leptons and real leptons

43

result is

$$N(Z \to \tau^+\tau^-) = \begin{cases} 0.38 \pm 0.11 & e\mu \\ 0.21 \pm 0.08 & ee\&\mu\mu \end{cases}$$

4.7.4 W^+W^-

We use ISAJET Monte Carlo generator to generate WW+dijet+$\not{E}_T$ events. Since the gluon radiation process in ISAJET is questionable, we used Z+dijet matrix element calculation to check the dijet fraction at normal Z process and compare it to the case when we raise Z mass to 240 GeV/c^2, the expected equivalent energy for WW process. We found that the fraction increased by 60%. On the other hand, ISAJET gives about 2.7 times more jets than Z data. So we multiply 1.6/2.7 on the dijet cut efficiency of ISAJET and we obtain

$$N(WW) = \begin{cases} 0.20 \pm 0.09 & e\mu \\ 0.16 \pm 0.07 & ee\&\mu\mu \end{cases}$$

4.7.5 Total Backgrounds

We summarize the backgrounds in table 4.4.

	$e\mu$	$ee + \mu\mu$	combined
W^+W^-	0.20±0.09	0.16±0.07	0.36±0.11
$Z \to \tau^+\tau^-$	0.38±0.11	0.21±0.08	0.59±0.14
Drell-Yan	—	0.62±0.30	0.62±0.30
Fake leptons	0.16±0.16	0.21±0.17	0.37±0.23

Table 4.4: Expected number of background events in 109 pb^{-1} of data.

Chapter 5

Mass Measurement

In a top quark event there are 6 particles in the final state. If we can measure all the four vectors of these 6 particles we can reconstruct top quark mass, i.e., we need to know 24 variables to measure top quark mass. However, in a dilepton event we can only measure the missing transverse energy and three vectors of 2 leptons and 2 jets. That's 2+3*4=14 variables. If we assume we know the mass of leptons and b quarks, we know 4 more variables and we need 6 more constraints to solve M_t. We do have the following constraints:

$$(\ell + \nu)^2 = M_W^2 \tag{5.1}$$

$$(\ell + \nu + b)^2 = M_t^2 \tag{5.2}$$

$$\vec{\nu}_{T1} + \vec{\nu}_{T2} = \not{E}_T \tag{5.3}$$

These 3 equations represents 6 constraints in the price of introducing one more variable: M_t. So we are still one constraint short and the top quark mass can not be analytically solved event-by-event.

Many physicists have tried many different ideas to get around this problem to measure the top quark mass. In this thesis we develop one of the simplest method.

From the cascade decay of the top quark, we have the following equations in the rest frame of W boson:

$$t \rightarrow W + b \qquad\qquad M_t^2 = M_W^2 + M_b^2 + 2M_W E_b \tag{5.4}$$

45

$$W \rightarrow \ell + \nu \qquad\qquad E_\ell = E_\nu = \frac{M_W}{2} \qquad\qquad (5.5)$$

where lepton masses are neglected. For a fixed M_t, E_b is a constant. And M_t can be determined from E_b by eq. (5.4).

Experimentally, we can probe E_b by measuring the Lorentz-invariant quantity $M_{\ell b}^2$, the invariant mass of the b quark and the lepton from W decay. It can be expressed in the W rest frame as

$$M_{\ell b}^2 = (\ell + b)^2 = M_\ell^2 + M_b^2 + 2E_\ell E_b - 2P_\ell P_b \cos\theta_{\ell b}.$$

We can substitute E_ℓ and P_ℓ by $M_W/2$ and obtain

$$\frac{M_{\ell b}^2 - M_b^2}{M_W} = E_b - P_b \cos\theta_{\ell b}. \qquad\qquad (5.6)$$

We have the following observations on equation (5.6):

- Only $M_{\ell b}^2$ and $\cos\theta_{\ell b}$ vary event-by-event. All other quantities are constants.

- We consider M_b and M_W as known, and use $M_b = 5$ GeV/c^2 and $M_W = 80.4$ GeV/c^2.

- E_b is the constant to be determined. P_b is just $\sqrt{E_b^2 - M_b^2}$.

- $M_{\ell b}^2$ can be measured in the lab frame in data because it is Lorentz-invariant.

- $\cos\theta_{\ell b}$ is unknown in each dilepton event because we can not reconstruct the W rest frame due the the presence of 2 neutrinos.

However, for a sample of dilepton top events, taking an average over events of equation (5.6) leads to

$$\frac{\langle M_{\ell b}^2 \rangle - M_b^2}{M_W} = E_b - P_b \langle \cos\theta_{\ell b} \rangle.$$

where

- $\langle M_{\ell b}^2 \rangle$ can be measured from the data. For a small number of top dilepton events, the statistical uncertainty in $\langle M_{\ell b}^2 \rangle$ will be a major source of the total uncertainty on M_t.

46

- $\langle \cos \theta_{\ell b} \rangle$ can be regarded as an input parameter from theory or Monte Carlo generators. In Ref [49], $\langle \cos \theta_{\ell b} \rangle = 0.144$ was obtained from PYTHIA for $M_t = 140$ GeV/c^2. The choice of $\langle \cos \theta_{\ell b} \rangle$ and its effect on the determination of M_t will be discussed in Section 5.1.

Thus, E_b can be obtained from $\langle \cos \theta_{\ell b} \rangle$ and measurements of $\langle M_{\ell b}^2 \rangle$, and M_t can be calculated using eq. (5.4).

A good approximation can be made here. Since $E_b \gg M_b$ ($E_b > 82$ GeV/c^2 for $M_t > 140$ GeV/c^2), we can safely expand P_b in orders of $(M_b/E_b)^2$. The leading term (0-th order) is just E_b and by further ignoring M_b^2 terms we get

$$M_t^2 = M_W^2 + \frac{2\langle M_{\ell b}^2 \rangle}{1 - \langle \cos \theta_{\ell b} \rangle}. \tag{5.7}$$

The error on M_t^2 in this approximation can be estimated by the dropped M_b^2 terms and the first order term in (M_b^2/E_b^2) which is

$$M_b^2 - \frac{2M_b^2}{1 - \langle \cos \theta_{\ell b} \rangle} + \frac{M_W M_b^2}{E_b} \frac{\langle \cos \theta_{\ell b} \rangle}{1 - \langle \cos \theta_{\ell b} \rangle}.$$

After substituting theoretical values for E_b and $\langle \cos \theta_{\ell b} \rangle$ (see section 5.1.1) the error term is -33.8 GeV^2/c^4 for $M_t = 140$ GeV/c^2 and -32.4 GeV^2/c^4 for $M_t = 220$ GeV/c^2. Percentage-wise, it is 0.17% and 0.067% for $M_t = 140$ and 220 GeV/c^2, respectively. We conclude that this approximation is very good.

It is worthwhile to mention that it is straight-forward to obtain the statistical uncertainty of M_t from the statistical uncertainty of $\langle M_{\ell b}^2 \rangle$:

$$\sigma_{M_t} = \frac{1}{M_t} \frac{\sigma \langle M_{\ell b}^2 \rangle}{1 - \langle \cos \theta_{\ell b} \rangle}. \tag{5.8}$$

The uncertainty term from $\sigma \langle \cos \theta_{\ell b} \rangle$,

$$\frac{1}{M_t} \frac{\langle M_{\ell b}^2 \rangle}{(1 - \langle \cos \theta_{\ell b} \rangle)^2} \sigma \langle \cos \theta_{\ell b} \rangle, \tag{5.9}$$

is not statistical in nature because we don't measure $\langle \cos \theta_{\ell b} \rangle$. $\sigma \langle \cos \theta_{\ell b} \rangle$ is the expected difference between the value we fix and the true $\langle \cos \theta_{\ell b} \rangle$. It is considered as a systematic uncertainty.

5.0.6 Outline of the method

The procedure to measure M_t is summarized as follows:

1. Measure $\langle M_{\ell b}^2 \rangle$ in the data sample.

2. Calculate E_b and M_t with input parameter $\langle \cos \theta_{\ell b} \rangle$ fixed at a pre-determined value (we use 0.118 in this study, see section 5.2.1).

3. Correct M_t with a correspondence function to compensate the shift produced by using a fixed $\langle \cos \theta_{\ell b} \rangle$.

4. Estimate the statistical uncertainty of M_t by equation (5.8) with $\sigma \langle M_{\ell b}^2 \rangle$ estimated in data.

5. Estimate the systematic uncertainty of M_t.

5.0.7 Strategy

We adopt the following strategy to develop the method toward the final measurement of M_t:

1. Make Monte Carlo samples of $t\bar{t} \rightarrow W^+ b W^- \bar{b} \rightarrow \ell^+ \nu \ell^- \bar{\nu} b \bar{b}$ events and check that they have the correct top quark decay properties.

2. Work in the Monte Carlo samples to demonstrate that this method works in the ideal case, and the statistical uncertainty can be estimated.

3. Study the effect of combinatorics of pairing leptons and jets.

4. Study the effect on M_t due to the presence of gluon jets and/or leptons from $W \rightarrow \tau \nu \rightarrow \ell \nu \nu$ decays in $t\bar{t}$ Monte Carlo.

5. Look at data to obtain M_t and its statistical uncertainty.

6. Study the systematic uncertainties.

5.1 $t\bar{t}$ Monte Carlo Samples

We use Monte Carlo samples to develop the method. Three types of $t\bar{t}$ Monte Carlo samples are used.

1. Generic HERWIG sample:

   - HERWIG version 5.6.

   - Parton distribution function: MRS-D0'.

   - Hard collision: $p\bar{p} \rightarrow t\bar{t}$.

   - No selection is used in HERWIG.

   - Tau leptons are re-decayed by TAUOLA 2.1 (library version 2.5).

   - b quarks are re-decayed by CLEOMC V9_0.

   - use QFL' for detector simulation.

2. HERWIG dilepton sample: this sample has been generated separately.

   - Same HERWIG+TAUOLA+CLEOMC as generic HERWIG sample.

   - Require 2 leptons with $P_T > 18$ GeV in generator level before QFL'.

3. HERWIG clean signal sample: This is a sub-sample of HERWIG dilepton sample. The following requirements were added to HERWIG dilepton sample to make this sample.

   - Standard dilepton selection cuts.

   - Require that both W bosons decay to $e\nu$ or $\mu\nu$.

   - Require the two leptons identified in reconstructed level match to leptons directly from W decays. The match requirement is $\Delta R < 0.4$ where ΔR is defined as $\sqrt{(\Delta\eta)^2 + (\Delta\phi)^2}$.

   - Require the 2 hardest jets match to b and $\bar{b}$ quarks with $\Delta R < 0.4$.

Background monte carlo samples will be described in the Background Section.

49

5.1.1 $\cos\theta_{\ell b}$: Theory

In Standard Model, the distribution of $\cos\theta_{\ell b}$ depends on the polarization of W boson[50, 51]. We denote the longitudinal, left-handed, and right-handed W bosons as W_0, W_- and W_+, respectively. We then have:

$$\frac{dN}{d\cos\theta_{\ell b}} \propto \begin{cases} \sin^2\theta_{\ell b} & Br(t \rightarrow b + W_0) = \dfrac{M_t^2}{M_t^2 + 2M_W^2} \\[2mm] \dfrac{1}{2}(1 + \cos\theta_{\ell b})^2 & Br(t \rightarrow b + W_-) = \dfrac{2M_W^2}{M_t^2 + 2M_W^2} \\[2mm] \dfrac{1}{2}(1 - \cos\theta_{\ell b})^2 & Br(t \rightarrow b + W_+) = 0 \end{cases}$$

After combining them,

$$\frac{dN}{d\cos\theta_{\ell b}} \propto \frac{M_t^2 \sin^2\theta_{\ell b} + 2M_W^2 \frac{(1-\cos\theta_{\ell b})^2}{2}}{M_t^2 + 2M_W^2} \tag{5.10}$$

Since the longitudinal W term in $dN/d\cos\theta_{\ell b}$ is proportional to $\sin^2\theta_{\ell b}$, which is symmetric in $\cos\theta_{\ell b}$, the contribution to mean is zero. So only left-handed W has non-zero contributions to the mean, i.e.,

$$\langle\cos\theta_{\ell b}\rangle = \frac{M_W^2}{M_t^2 + 2M_W^2} \tag{5.11}$$

Thus, the theoretical $\langle\cos\theta_{\ell b}\rangle$ is exactly half of the branching ratio of top decaying into left-handed W:

$$\langle\cos\theta_{\ell b}\rangle = \frac{1}{2} Br(t \rightarrow b + W_-)$$

5.1.2 Modeling of $\cos\theta_{\ell b}$ in HERWIG: A Check

At first, we want to make sure the $t\bar{t}$ monte carlo has the correct W polarization effect built in. We compare the $\cos\theta_{\ell b}$ distribution in the generic HERWIG sample with the Standard Model prediction. Generator information of 4-vectors of W is used to boost the lepton and b into W rest frame where $\cos\theta_{\ell b}$ is calculated. Upper half of figure 5.1 shows the $\cos\theta_{\ell b}$ distributions for $M_t = 140$ GeV/c^2 and $M_t = 220$ GeV/c^2. The agreement between HERWIG and Standard Model indicates that HERWIG is modeling correctly the W polarization in top decay.

50

Only the mean of $\cos\theta_{\ell b}$ enters into this method. Good agreement in $\langle\cos\theta_{\ell b}\rangle$ vs M_t between the generic HERWIG samples and the theoretical curve of eq. (5.11), is shown in bottom half of figure 5.1.

5.1.3 Some Kinematical Observables in $t\bar{t}$ Monte Carlo

Here we examine distributions of some variables in HERWIG clean signal sample. We show in figure 5.2 the distribution of object P_T in 3 HERWIG samples with M_t assigned to 140, 180, and 220 GeV/c^2, respectively. It is apparent that E_T of the leading jet has the best discriminating power among those 4 variables shown.

We also checked distribution of invariant masses of lepton+jet. There is a complication here. There are 2 leptons and (at least) 2 jets in a typical dilepton candidate event. If we only take the 2 hardest jets j_1 and j_2, there are 4 combinations of forming invariant masses:

$$\text{Pair 1:} \qquad M_{+1}^2 = M_{\ell^+ j_1}^2, \quad M_{-2}^2 = M_{\ell^- j_2}^2$$

$$\text{Pair 2:} \qquad M_{+2}^2 = M_{\ell^+ j_2}^2, \quad M_{-1}^2 = M_{\ell^- j_1}^2$$

In the clean signal sample, one of the pairs is right, i.e., it combines ℓ^+ with b and ℓ^- with $\bar{b}$, and the other pair is wrong. Distribution of the 2 invariant masses from the right pair is shown in figure 5.3a) and those from the wrong pair are shown in figure 5.3b). We know by neglecting a M_b^2 term that the distribution of right pairing $M_{\ell b}^2$ is proportional to $(1 - \cos\theta_{\ell b})$. Thus it is bounded above by the condition $\cos\theta_{\ell b} > -1$. On the other hand, the wrong pair takes leptons from one side and jet from the other side of the $t\bar{t}$ event, and the distribution is ultimately related to $t - \bar{t}$ correlation. What we see in HERWIG clean signal sample is an exponential distribution which hints that the correlation is either small or not implemented in HERWIG.

Since we don't know which jet is b and which jet is $\bar{b}$ in real data, it can not be determined which pair is the right one. We define two pairings:

All pairs (M_{all}^2)   : Both Pair 1 and Pair 2 are used.
Softer pair (M_{min}^2) : Pick the pair that gives smaller $\sum M_{\ell b}^2$
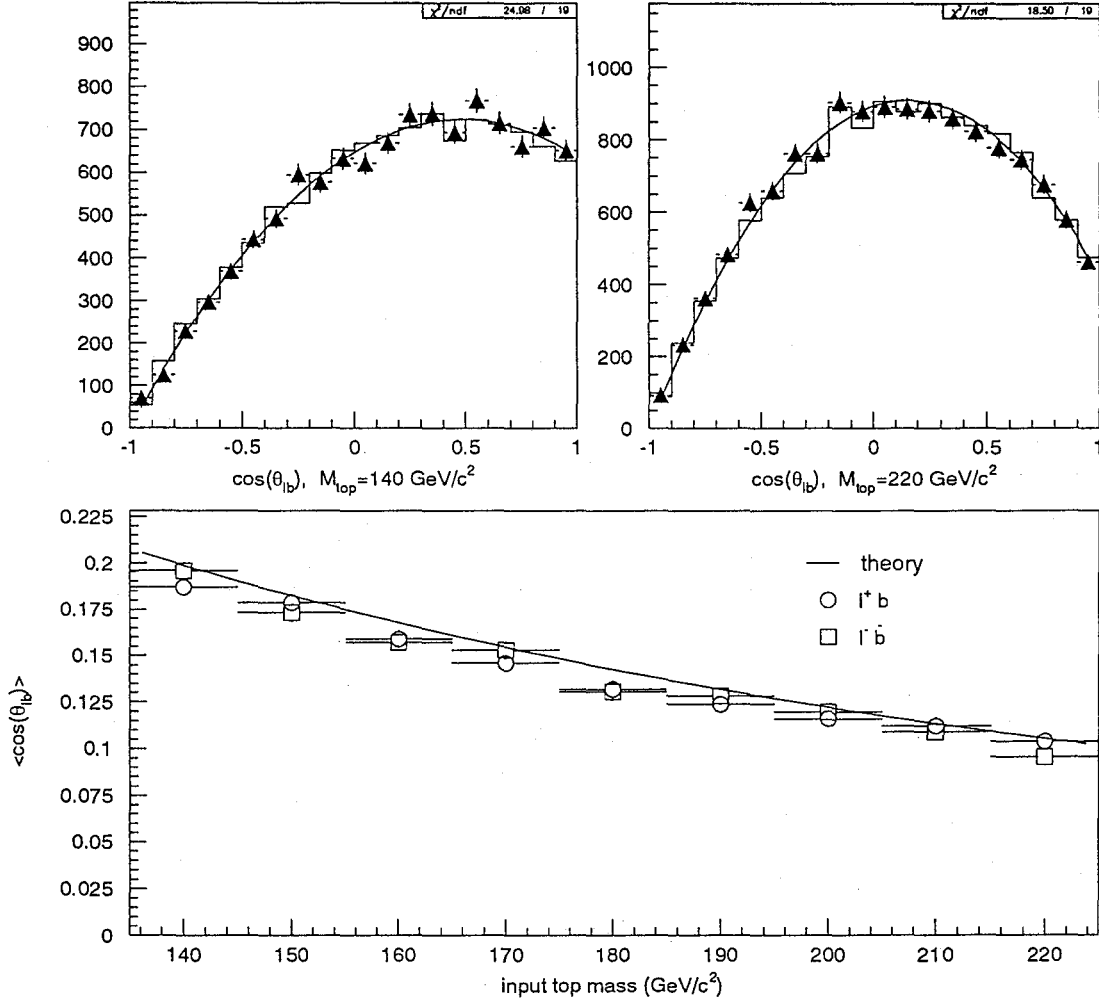
51

Figure 5.1: $\cos\theta_{\ell b}$ in the generic HERWIG $t\bar{t}$ samples without analysis cuts. Top: The distribution of $\cos\theta_{\ell b}$ in $M_t = 140$ GeV/c^{2}and 220 GeV/c^{2}samples. The black triangles are $\cos\theta_{\ell-\bar{b}}$, the dashed histogram is $\cos\theta_{\ell+b}$, the curve is theoretical curve of $dN/d\cos\theta_{\ell b}$ (eq (5.10)) normalized to $\cos\theta_{\ell-\bar{b}}$. Bottom: $\langle\cos\theta_{\ell b}\rangle$ vs input top mass. HERWIG and Standard Model theory agrees with each other very well.
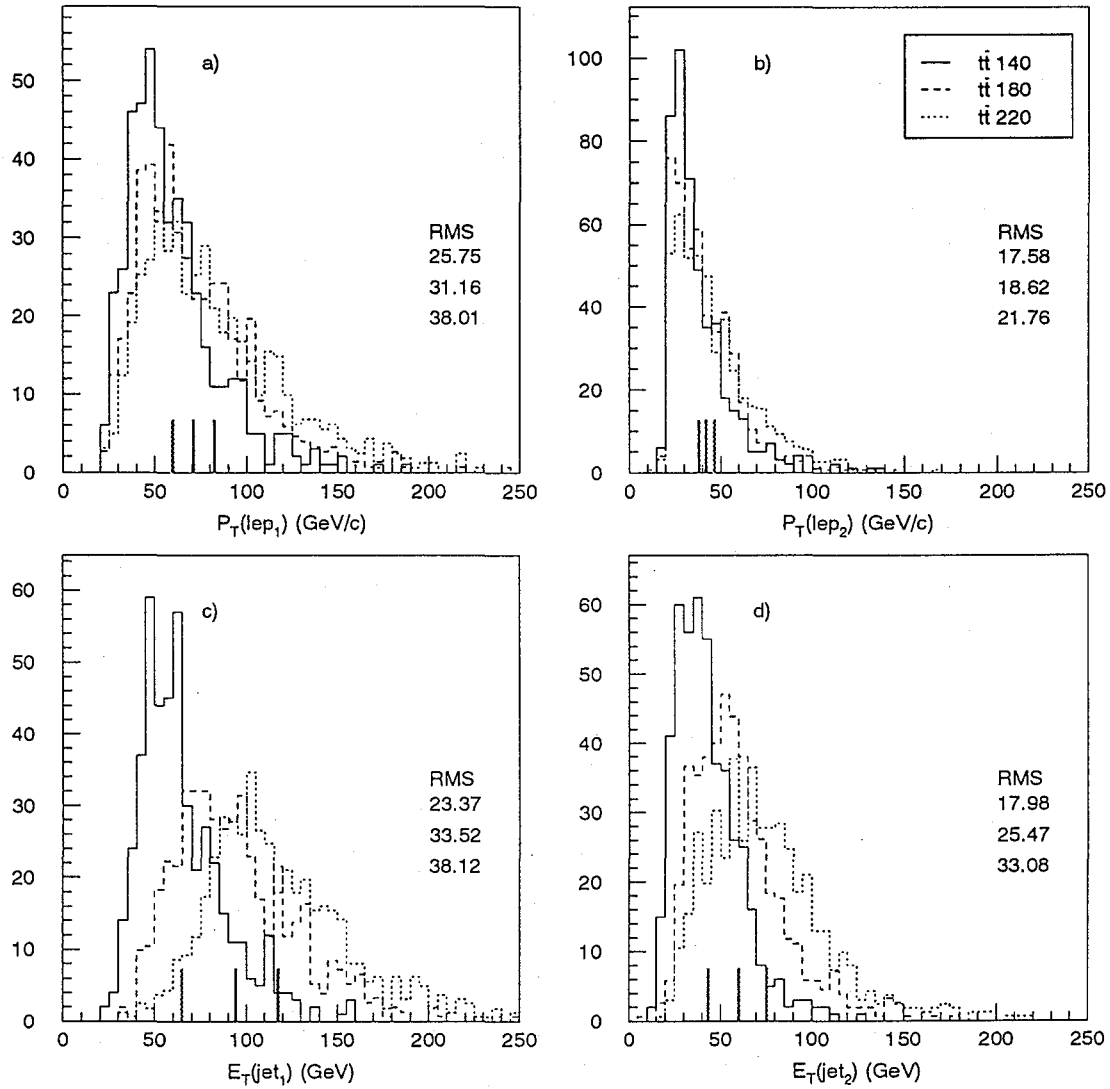
Figure 5.2: P_T of the 4 objects that we use for the mass reconstruction for 3 different top mass samples. The vertical bars in the bottom of each plot indicates the mean of the variable in each top mass sample. It is seen that the average P_T of the second lepton is essentially independent of top mass, and E_T of the leading jet gives the most discriminating power among those 4 variables.
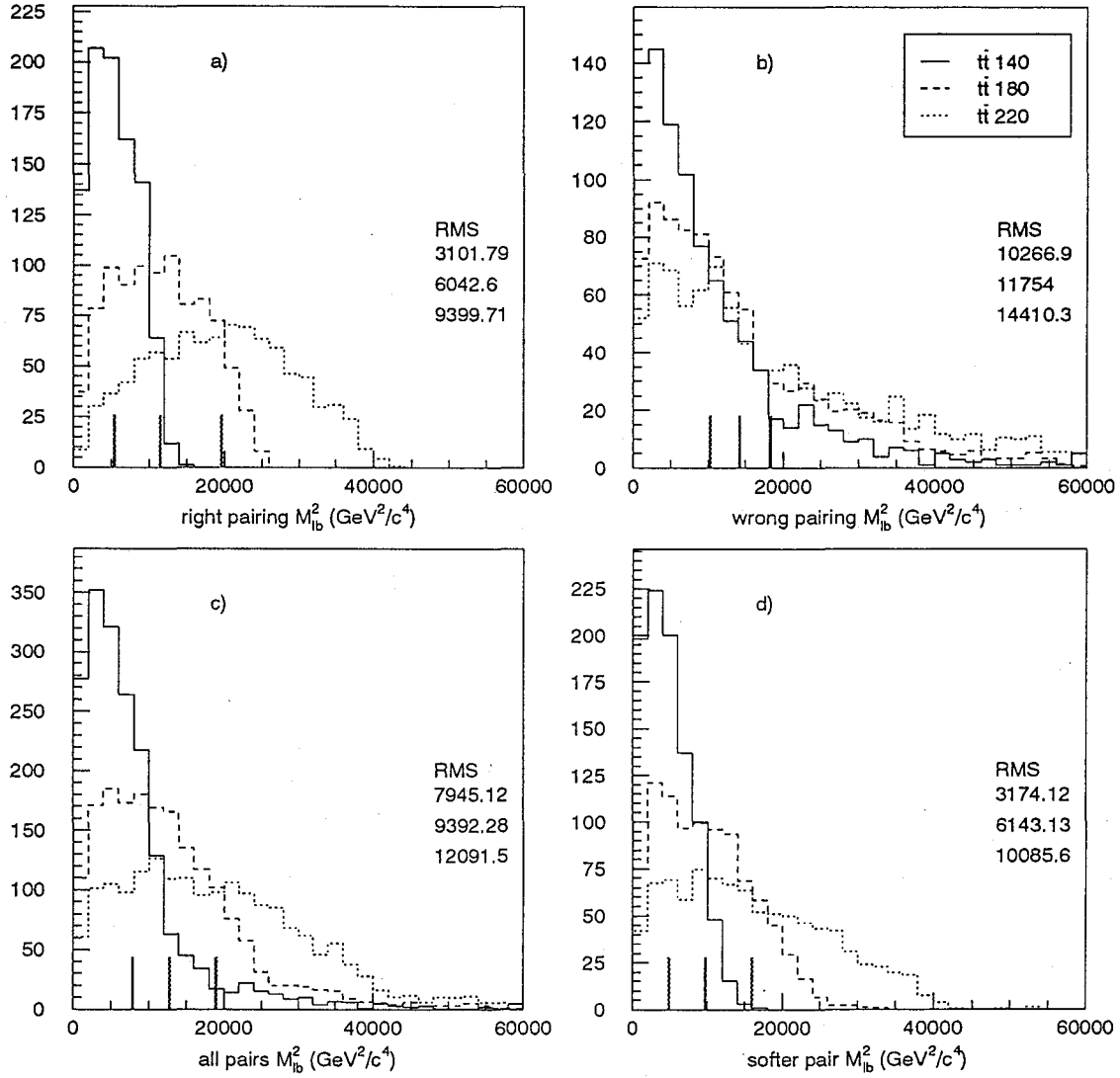
Figure 5.3: The distribution of M_{lb}^2. a) Right pairing, b) wrong pairing, c) all pairs, d) softer pair. See text for definitions. The right pairing, as predicted in theory, are bounded above. The wrong pairing exhibits an exponential tail.

They are shown in figure 5.3c) and figure 5.3d).

5.1.4 $\cos\theta_{\ell b}$ in Selected Events: Selection Bias

We use HERWIG clean signal samples to check $\cos\theta_{\ell b}$ in $t\bar{t}$ dilepton events after the selection cuts. See figure 5.4.

We see that the selection procedure have a bias on the $\cos\theta_{\ell b}$ distribution. The effect of the bias is cutting out events with $\cos\theta_{\ell b} \approx 1$. Since $M_{\ell b}^2 \approx t(1 - \cos\theta_{\ell b})$, it means events with small $M_{\ell b}^2$ are rejected. To form a small invariant mass, 2 objects need to have either low energy or small angular separation, or both. So the bias can be understood as the following:

- The P_T thresholds for leptons and jets filter out low P_T leptons and low E_T jets.

- For isolated leptons: the isolation cut keeps jets away from it.

- For non-isolated leptons: E/P cut for electrons, E_{HAD} and E_{EM} cuts for muons are implicit isolation cuts.

The selection bias prevented us from using the theoretical value of $\langle\cos\theta_{\ell b}\rangle$. So we need to find a proper value for $\langle\cos\theta_{\ell b}\rangle$ for our method. This is described in the next section.

5.2 Method Development

From the previous section we know 2 facts:

1. Selection bias keeps us from using the theoretical value of $\langle\cos\theta_{\ell b}\rangle$.

2. Lack of b and $\bar{b}$ identification makes us unable to use the right pair of $\langle M_{\ell b}^2 \rangle$.

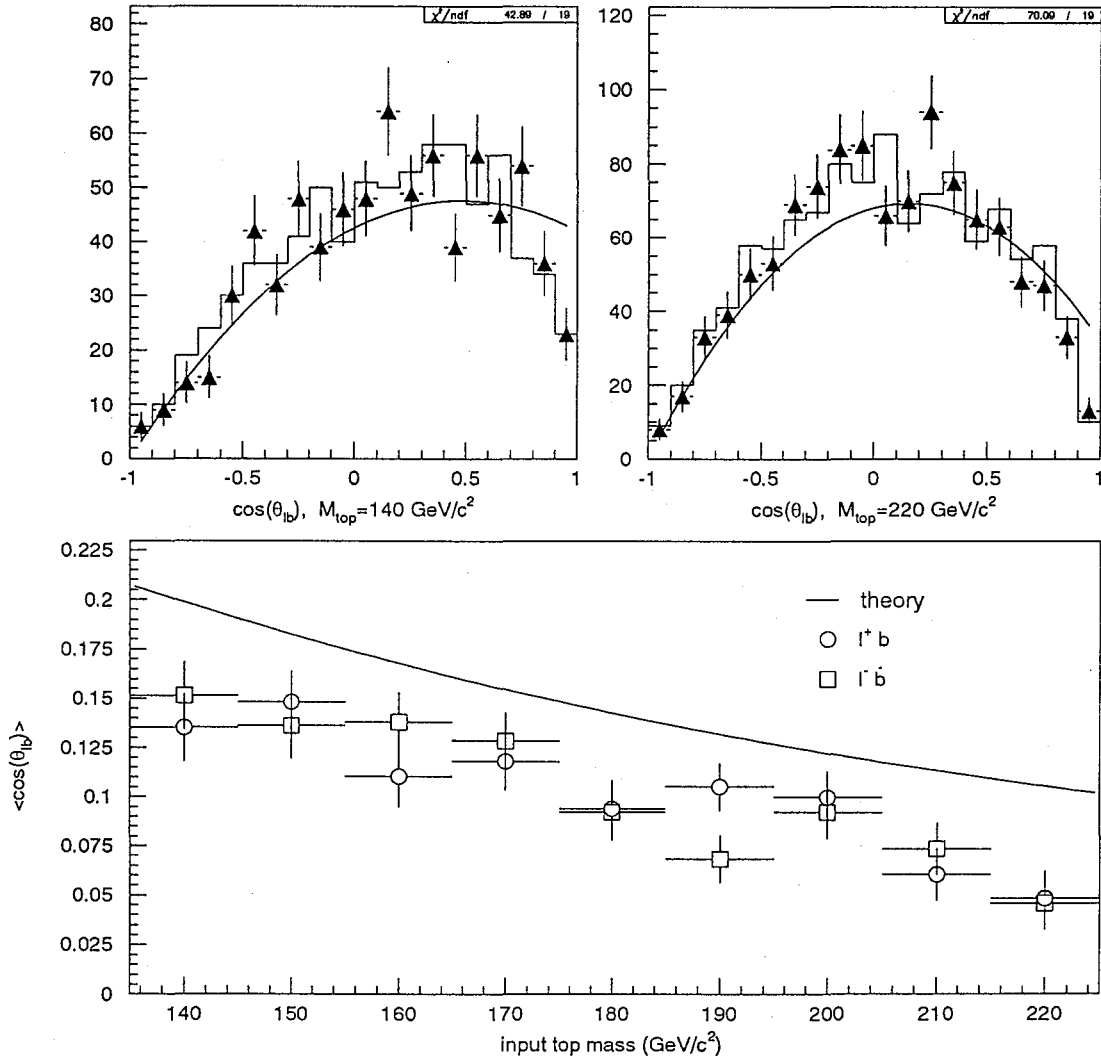In this section we develop a method to handle these issues.

Figure 5.4: $\cos\theta_{\ell b}$ in the HERWIG clean signal sample. Top: The distribution of $\cos\theta_{\ell b}$ in $M_t = 140$ GeV/c^2 and 220 GeV/c^2 sample. The legends are the same as figure 5.1. Bottom: $\langle\cos\theta_{\ell b}\rangle$ vs top mass. A discrepancy from Standard Model is clearly seen.

5.2.1 Choosing $\langle \cos \theta_{\ell b} \rangle$

HERWIG clean signal $t\bar{t}$ samples are used to determine $\langle \cos \theta_{\ell b} \rangle$ with the following procedure:

1. Measure $\langle M_{\ell b}^2 \rangle$ of right pair in each sample with input top mass $M = 140, 150, ..., 220$.

$$\langle M_{\ell b}^2 \rangle_M = \frac{1}{2N} \sum_{N \text{ events}} (M_{\ell^+ b}^2 + M_{\ell^- \bar{b}}^2). \tag{5.12}$$

   where N is the total number of events in each sample.

2. For any given $c \equiv \langle \cos \theta_{\ell b} \rangle$, calculate M_t by equation (5.7). Thus the resultant M_t is a function of $\langle \cos \theta_{\ell b} \rangle$ and M, i.e., $M_t = M_t(M; c)$.

3. Define $\chi^2(c)$ as

$$\chi^2(c) \equiv \sum_M \frac{(M_t(M, c) - M)^2}{\sigma_{M_t}^2(M, c)}$$

   where the denominator is given by Eq. (5.8). Minimize $\chi^2(c)$ with respect to c to get the best $\langle \cos \theta_{\ell b} \rangle$ to be used throughout this study.

We fit the function $\chi^2(c)$ to a parabola and obtain the minimum point at 0.118.

The minimum point depends on the samples used in the calculation of $\chi^2(c)$. For example, if we exclude $M_t = 210$ GeV and $M_t = 220$ GeV samples, the minimum point is at $c \approx 0.132$. If we exclude the $M_t = 140$ and 150 GeV/c^2 samples, it moves to 0.110. The effect on M_t from using different values of $\langle \cos \theta_{\ell b} \rangle$ is shown in the next section.

5.2.2 Calculating M_t in Monte Carlo Samples

We fix $c = 0.118$ and apply our method on the HERWIG clean signal samples. The result is shown in figure 5.6. The optimal value of c is close to the right value for true $M_t = 180$ GeV/c^2, the central sample. For smaller true M_t, the output M_t is lower than true value, while for larger true M_t it is higher. This can be understood in the following way:
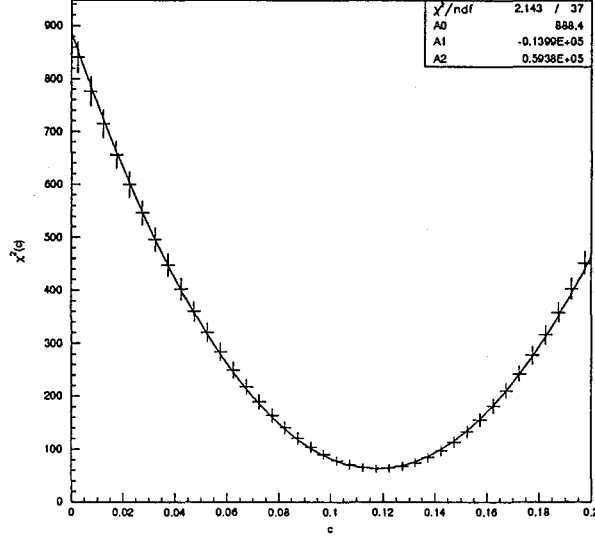
Figure 5.5: $\chi^2(c)$ obtained from 9 HERWIG clean signal sample. The minimum point is at $0.1399/2/0.5938 = 0.118$.

Eq. (5.7): smaller input parameter $\langle \cos \theta_{\ell b} \rangle$ $\Rightarrow$ smaller M_t

Figure 5.4: smaller true M_t $\Rightarrow$ bigger true $\langle \cos \theta_{\ell b} \rangle$

Therefore: if true M_t is small $\Rightarrow$ true $\langle \cos \theta_{\ell b} \rangle$ is large,

    $\Rightarrow$ fixed c is smaller than true $\langle \cos \theta_{\ell b} \rangle$,

    $\Rightarrow$ output M_t is smaller than true M_t

Actually this is a nice feature. This means the resolution of the method is good in ideal case.

The biggest difference between output M_t and true M_t is 5.3 GeV/c^2 at true $M_t = 220$ GeV/c^2.

From eq. (5.9) we can estimate the systematic uncertainty due to the change of c mentioned in the previous section. The maximum of uncertainty is 1.6 GeV/c^2 for $\langle \cos \theta_{\ell b} \rangle = 0.110$, and 0.89 GeV/c^2 for $\langle \cos \theta_{\ell b} \rangle = 0.132$. This shift is small, and can be compensated later, see next section.

5.2.3 Correction Function: output $M_t \rightarrow$ true M_t

Figure 5.6 shows the relation between calculated M_t and true M_t for both generator and reconstructed data level, with the expected shift of M_t due to fixed $\langle \cos \theta_{\ell b} \rangle$. This shift can be compensated by
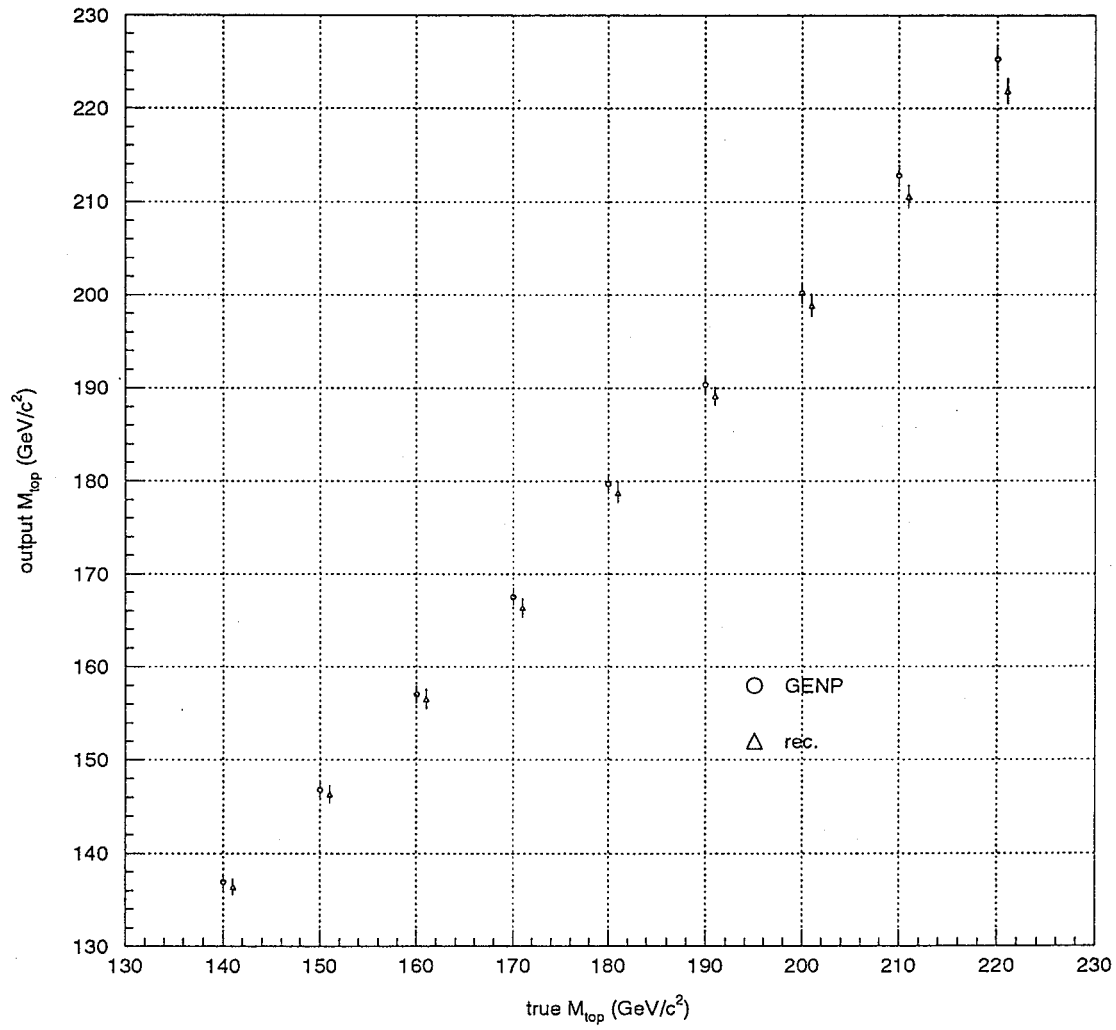
Figure 5.6: Output M_t vs true M_t. The optimal $\langle \cos \theta_{\ell b} \rangle = 0.118$ is used. The points from reconstructed level are shifted to the right side by 1 GeV/c^2 in order to see the error bars clearly.

fitting output M_t as a linear function of true M_t

$$M_t = A_0 + A_1 M_t^{true}$$

and the inverse function

$$M_t^{true} = B_0 + B_1 M_t \qquad (5.13)$$

gives the correction. To avoid confusion, we use the following names for variables:

Raw M_t (M_t^{raw}) : M_t obtained from eq. (5.7) with fixed $\langle \cos \theta_{\ell b} \rangle$.

Correction Function   :   Function to map raw M_t to true M_t.

Final M_t : M_t obtained after applying correction function to M_t^{raw}.

So the correction function is

$$M_t^{final} = B_0 + B_1 M_t^{raw}. \qquad (5.14)$$

The coefficients A_0, A_1, B_0, B_1 and their covariances are listed in table 5.1.

	A_0	A_1	$V_{A_0 A_1}$
rec.	-13.9±2.55	1.07±0.0144	-0.0364
GENP	-18.1±2.28	1.10±0.0130	-0.0292

	B_0	B_1	$V_{B_0 B_1}$
rec.	13.1±2.21	0.936±0.0127	-0.0276
GENP	16.5±1.88	0.911±0.0107	-0.0200

Table 5.1: The parameters obtained from linear fit of M_t^{raw} vs M_t^{true}. $V_{A_0 A_1}$ is the covariance of A_0 and A_1 and $V_{B_0 B_1}$ is the covariance of B_0 and B_1.

5.2.4   Statistical Uncertainty of Final M_t

The uncertainty of final M_t can be written as

$$
\begin{aligned}
\sigma^2(M_t^{final}) &= \sigma_{B_1}^2 (M_t^{raw})^2 + 2V_{B_0 B_1} M_t^{raw} + \sigma_{B_0}^2 + B_1^2 \sigma^2(M_t^{raw}) \\
&\equiv \sigma_B^2(M_t^{raw}) + B_1^2 \sigma^2(M_t^{raw}) \qquad (5.15)
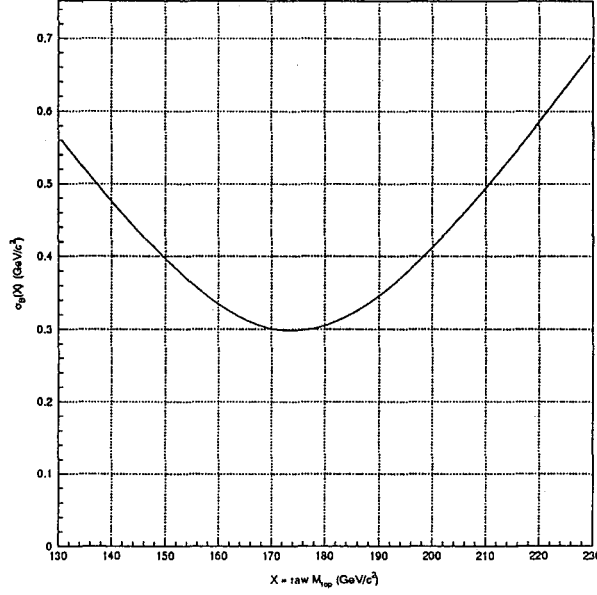\end{aligned}
$$

Figure 5.7: The $\sigma_B^2(M_t^{raw})$ term in eq. (5.15).

The magnitude of $\sigma_B^2(M_t^{raw})$ is due to Monte Carlo statistics. As shown in figure 5.7, it is negligible.

We can verify our estimate of statistical uncertainty (eq. (5.15)) by performing *pseudo experiments*:

1. Randomly select 10 events from HERWIG clean signal sample to mimic the data taken in an experiment.

2. Calculate $\langle M_{\ell b}^2 \rangle$ from 20 measurements of $M_{\ell b}^2$ in the 10 events. Set $\sigma \langle M_{\ell b}^2 \rangle = \text{RMS}/\sqrt{20}$, define pull $\equiv \dfrac{\langle M_{\ell b}^2 \rangle - \text{true } \langle M_{\ell b}^2 \rangle}{\sigma(\langle M_{\ell b}^2 \rangle)}$. Here true $\langle M_{\ell b}^2 \rangle$ is the mean value of $M_{\ell b}^2$ in the whole monte carlo sample.

3. Calculate raw M_t from equation (5.7), and $\sigma(M_t^{raw})$ from equation (5.8), and pull $\equiv$ (raw M_t - true M_t)/$\sigma(M_t^{raw})$.

4. Calculate final M_t from equation (5.14), $\sigma(M_t^{final})$ from equation (5.15), and pull $\equiv$ (final M_t - true M_t)/$\sigma(M_t^{final})$.

61

5. Repeat and plot distributions of variables.

See figures 5.8, 5.9 and 5.10 for distributions. From figure 5.8 we see that the statistical error of $\langle M_{\ell b}^2 \rangle$ is larger than $(\text{RMS}/\sqrt{2N})$ by 3% to 7% because $M_{\ell b}^2$ distribution is not Gaussian, and this discrepancy is carried over to the pull distribution of raw M_t and final M_t, but not magnified nor shrunk. This proves that our expressions for statistical uncertainty of raw M_t and final M_t are correct.

5.2.5 Lepton-Jet Pairing for $M_{\ell b}^2$

The developed method so far works well when we know which lepton is paired with which jet. But this can not be done for the data because we don't distinguish b jets from $\bar{b}$ jets. As shown in section 5.1.3 and Figure 5.3:

- The distribution of $M_{\ell b}^2$ of right pairs is highly dependent on true M_t. And they are bounded above.

- The distribution of $M_{\ell b}^2$ of wrong pairs all have long tails and the shape is less dependent on true M_t although the mean still follows M_t.

- The mean values of $M_{\ell b}^2$ in the wrong pairs tend to be larger than that in right pairs, especially for smaller M_t.

These observations motivates us to use the pair that gives smaller $M_{\ell b}^2$, i.e., M_{min}^2. The percentage of obtaining the right pair by selecting M_{min}^2, as shown in figure 5.11, is 72% for $M_t = 140$ GeV/c^2 and is only 52% for $M_t = 220$ GeV/c^2, consistent with expectations from Figure 5.3.

In the next section we study the mapping between $\langle M_{min}^2 \rangle$ and right pair $\langle M_{\ell b}^2 \rangle$.

5.2.6 Correspondence Function: from $\langle M_{min}^2 \rangle$ to $\langle M_{\ell b}^2 \rangle$

The right pair $\langle M_{\ell b}^2 \rangle$ is used to determine M_t. So correspondence functions are needed to map $\langle M_{min}^2 \rangle$ to $\langle M_{\ell b}^2 \rangle$. Figure 5.12 shows scatter plot of $M_{\ell b}^2$ vs M_{min}^2 obtained from the HERWIG clean
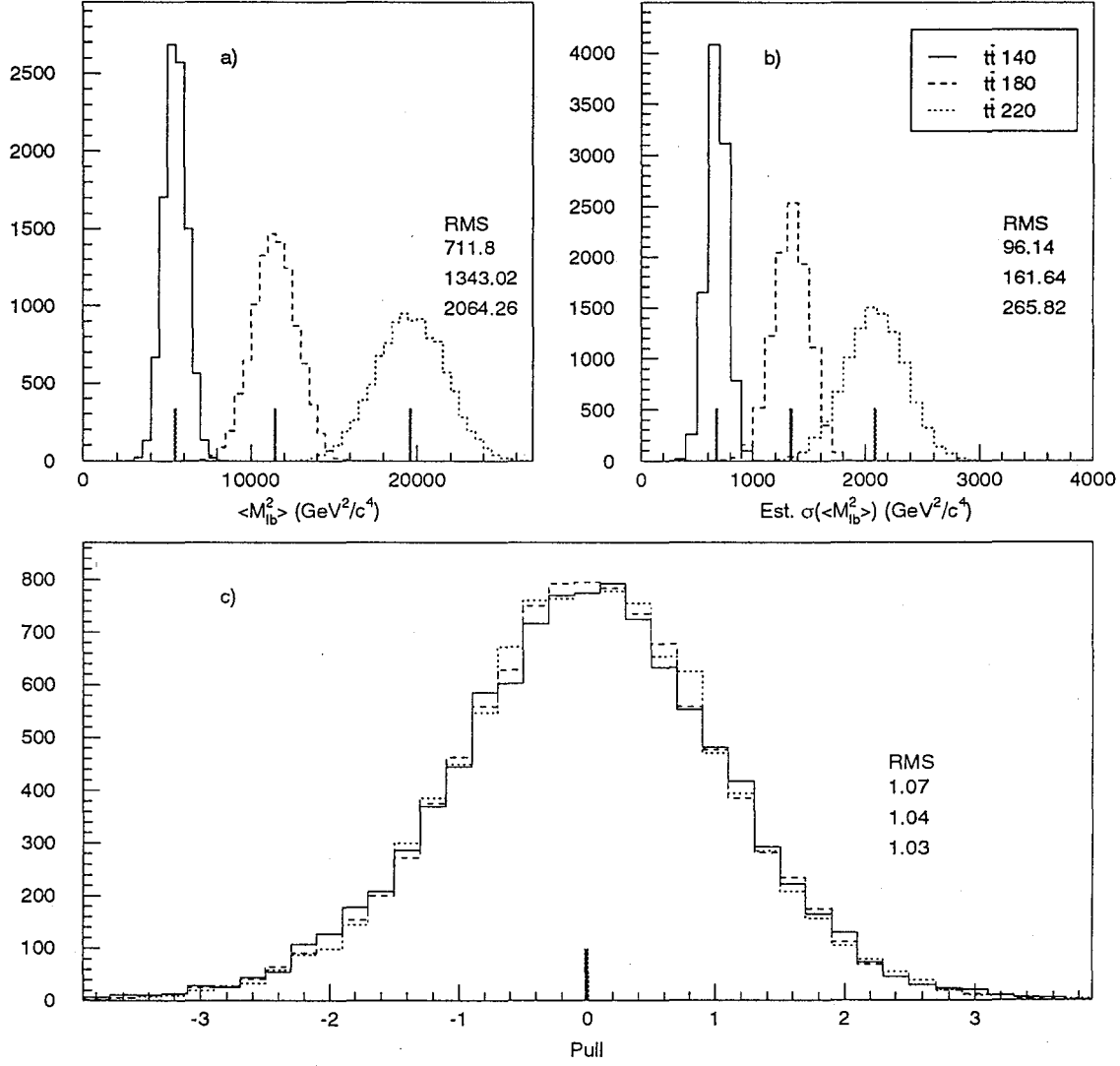
Figure 5.8: $\langle M_{\ell b}^2 \rangle$ distribution in pseudo experiments with input $M_t = 140$, 180 and 220 GeV/c². Top left: $\langle M_{\ell b}^2 \rangle$. Top right: Estimated statistical error $\sigma \langle M_{\ell b}^2 \rangle = \mathrm{RMS}(M_{\ell b}^2)/\mathrm{sqrt}(2N)$. Bottom: Pull distribution. Pull $\equiv (\langle M_{\ell b}^2 \rangle - \mathrm{true}\ \langle M_{\ell b}^2 \rangle)/(\mathrm{est.}\ \sigma \langle M_{\ell b}^2 \rangle)$.

Figure 5.9: Raw M_t distribution in pseudo experiments with input $M_t = 140$, 180 and 220 GeV/c^2. Top left: Raw M_t. Top right: Estimated statistical error $\sigma(M_t^{raw})$ from eq. (5.8). Bottom: Pull distribution. The pull distribution is not expected to center at 0 because we know there is a shift between raw M_t and true M_t.
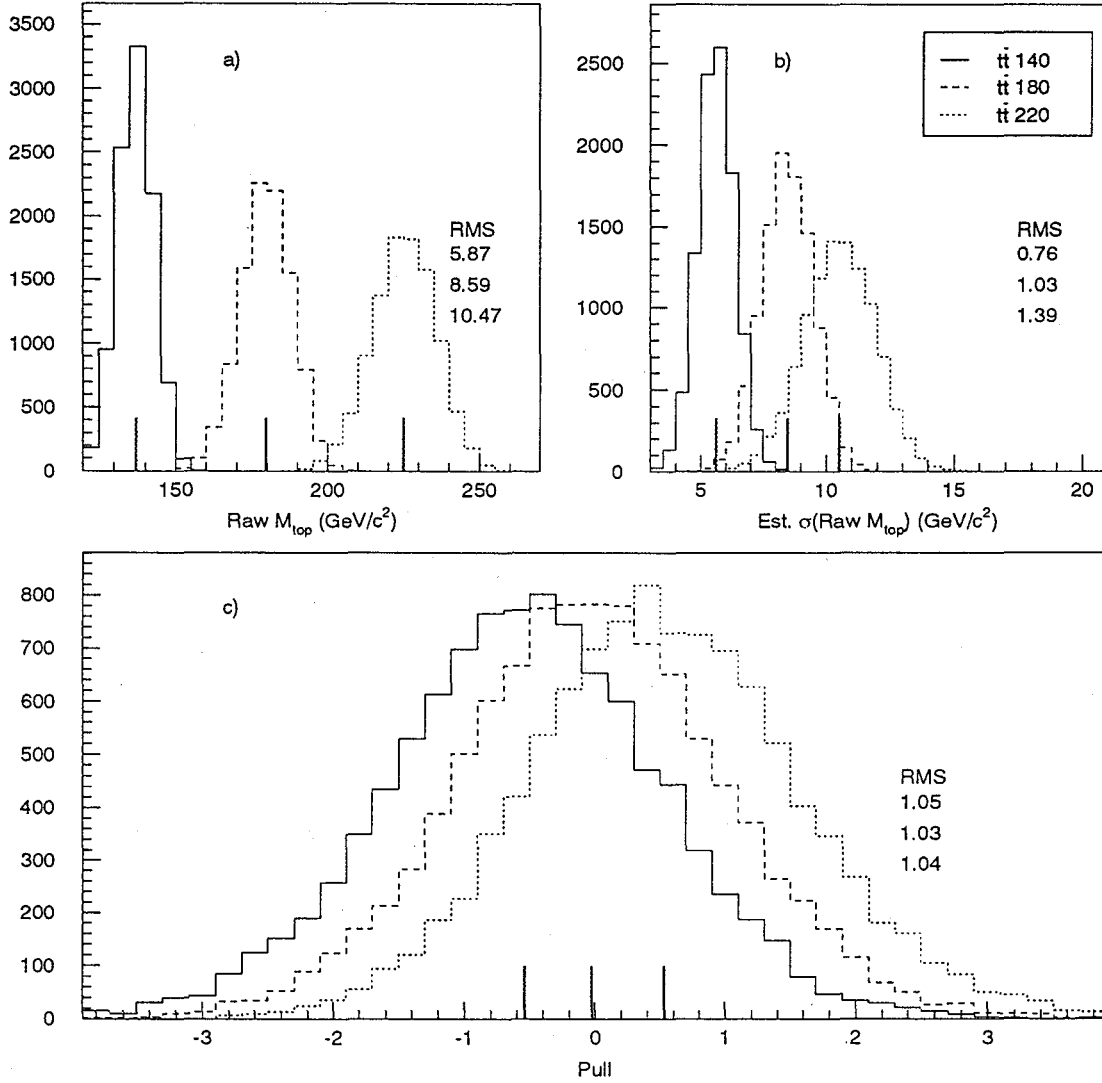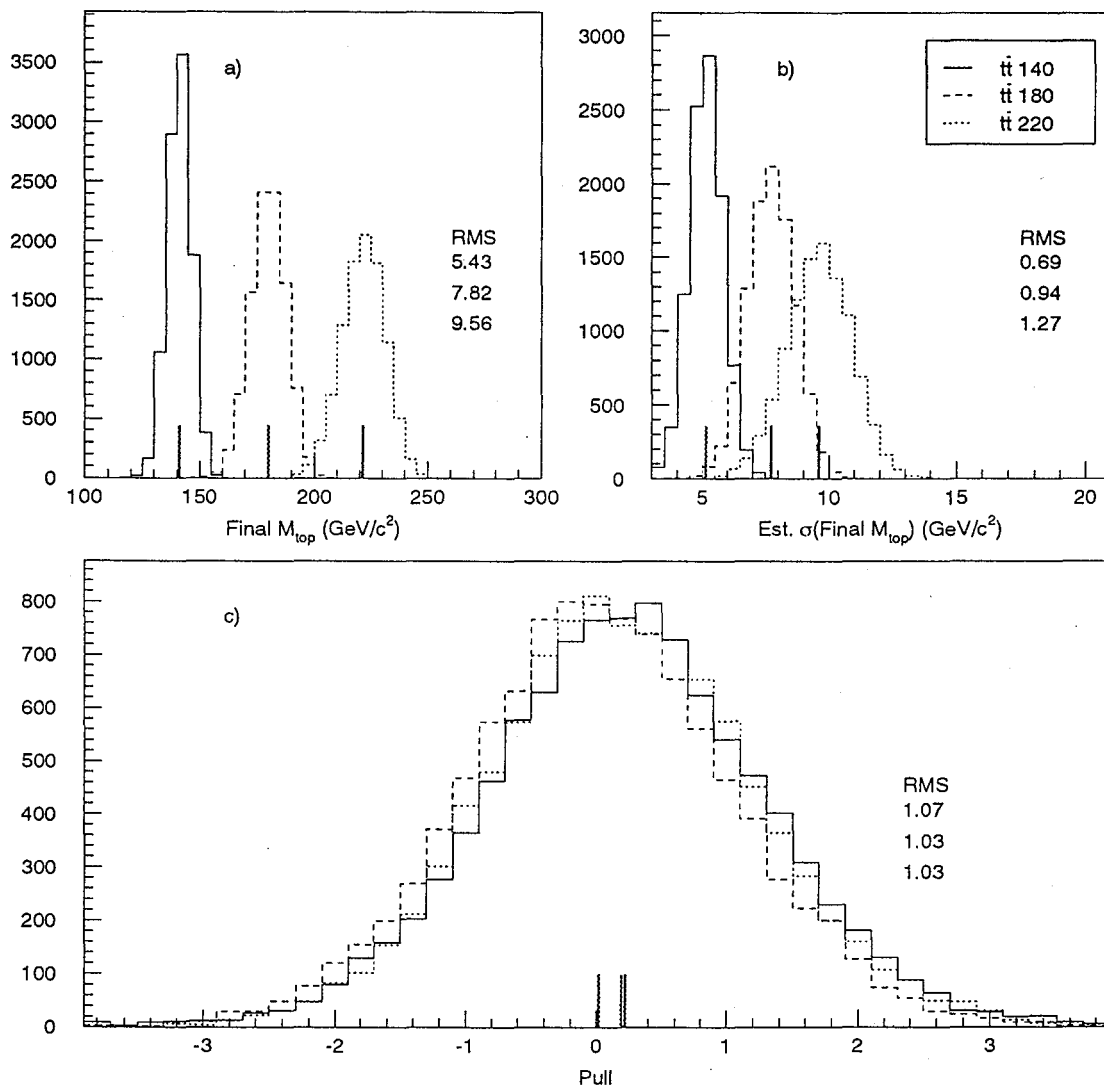
Figure 5.10: Final M_t distribution in pseudo experiments with input $M_t = 140$, 180 and 220 GeV/c^2. Top left: Final M_t. Top right: Estimated statistical error σ_{M_t} from eq. (5.15). Bottom: Pull distribution.
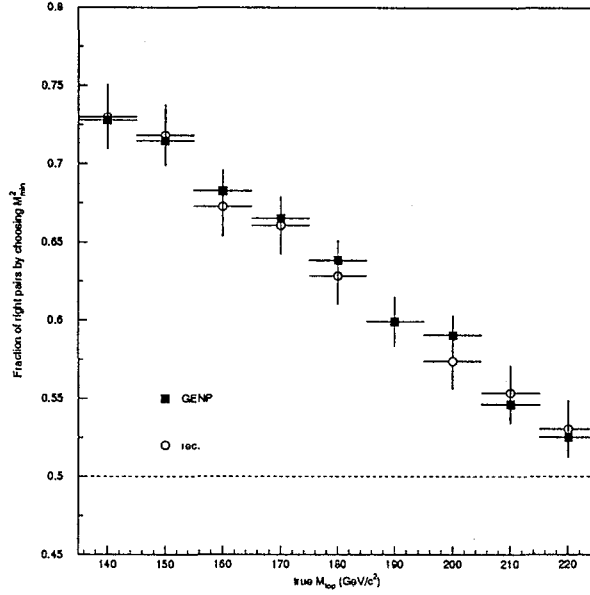
Figure 5.11: The percentage of picking the right pair by using M^2_{min} as a function of true M_t.

signal samples.

In Figure 5.12, lots of data points are concentrated on the diagonal, indicating a good chance of getting the right pair. Since M^2_{min} is the minimum of two pairs, it is always less than or equal to right pair $M^2_{\ell b}$.

These scatter plots show that $M^2_{\ell b}$ is not a single-valued function of M^2_{min}. However, we can still use the HERWIG clean signal samples to map the central values of M^2_{min} to $\langle M^2_{\ell b} \rangle$. In each sample with a fixed M_t, we calculate $\langle M^2_{\ell b} \rangle$ and $\langle M^2_{min} \rangle$, and fit them to a linear function

$$\langle M^2_{\ell b} \rangle = C_0 + C_1 \langle M^2_{min} \rangle.$$

Figure 5.13 shows the scatter plot of $\langle M^2_{\ell b} \rangle$ vs $\langle M^2_{min} \rangle$, together with the linear fit.[1] One can see that linear fit is a reasonable choice. The parameters obtained from the fit are: $C_0 = -823. \pm 220.$, $C_1 = 1.27 \pm 0.0254$ and the covariance $V_{C_0 C_1} = -5.24$.

---

[1]Because we have uncertainties on both X and Y variables in fitting, the standard least-square fitting procedure doesn't work. We use a least-square fit program developed in Ref. [55] to do the fit and obtain the covariance matrix.
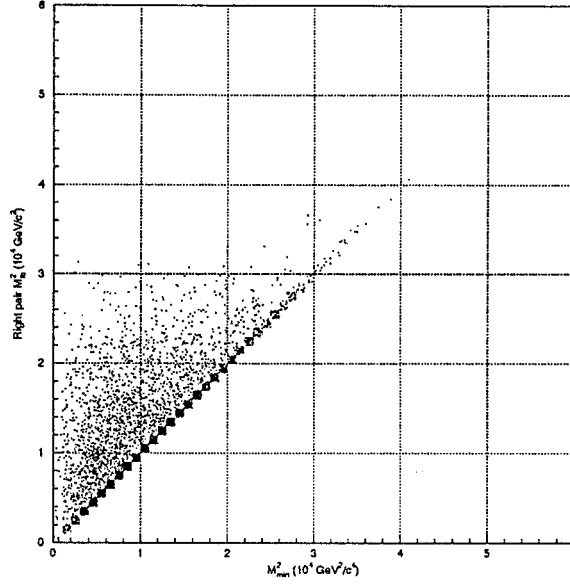
66

Figure 5.12: Scatter plot of right pair $M_{\ell b}^2$ vs M_{min}^2. All events in the 9 HERWIG clean signal samples are plotted into this figure.

The statistical uncertainty of $\langle M_{\ell b}^2 \rangle$ can be written down as

$$
\begin{aligned}
\sigma_{\langle M_{\ell b}^2 \rangle}^2 &= \sigma_{C_0}^2 + 2V_{C_0 C_1} \langle M_{min}^2 \rangle + \sigma_{C_1}^2 \langle M_{min}^2 \rangle^2 + C_1^2 \sigma^2 \langle M_{min}^2 \rangle \\
&= \sigma_C^2(\langle M_{min}^2 \rangle) + C_1^2 \sigma^2 \langle M_{min}^2 \rangle
\end{aligned}
\tag{5.16}
$$

$\sigma_C(\langle M_{min}^2 \rangle)$ is shown in figure 5.14.

We can again verify equation (5.16) by pseudo experiments. The statistical uncertainty of final M_t is estimated by eq. (5.15), and the pull distribution is examined. See figures 5.15 and 5.16 for results from pseudo experiments. As seen in the pull distribution of $\langle M_{min}^2 \rangle$, the statistical uncertainty is again under-estimated by using RMS$/\sqrt{2N}$ To get a better estimate of uncertainties, we attempted to multiply a factor of 1.07 to RMS$/\sqrt{2N}$ as the estimate of error on mean and we obtain the root-mean-squares of pull distributions of final M_t as 0.98, 0.99 and 1.02 for the 3 true top masses we used in doing pseudo experiments.

We also tried to use M_{all}^2 as our choice of pairing. We see that due to the long tail of M_{all}^2 distribution (see figure 5.3c), the pull of $\langle M_{all}^2 \rangle$ is no longer Gaussian-like. This directly translates
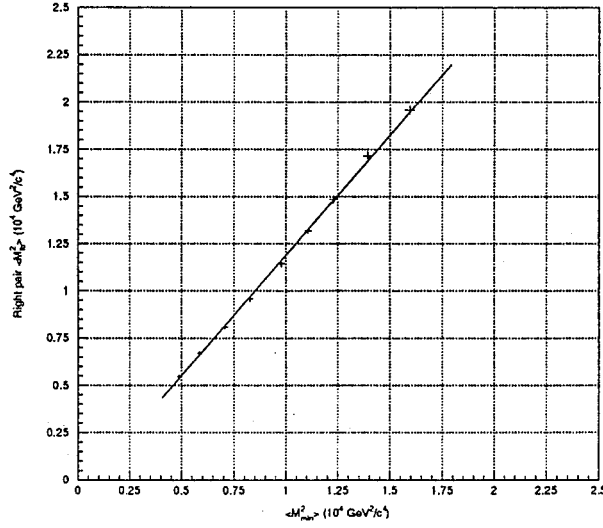
67

Figure 5.13: The scatter plot of $\langle M_{\ell b}^2 \rangle$ vs $\langle M_{min}^2 \rangle$. Each point is from one HERWIG clean signal sample with one true M_t.

into the very non-Gaussian shape of pull of final M_t. The statistical uncertainty estimate in $\langle M_{all}^2 \rangle$ pairing would not be reliable, and we abandon using M_{all}^2.

5.2.7 Summary of Method Development

We have demonstrated that this method works in ideal $t\bar{t}$ events that in average we can get the final M_t close to true M_t, and the statistical uncertainty estimate is appropriate. The flow chart of the method is shown in figure 5.17. The statistical uncertainty would be improved by approximately 30% if the right lepton-jet pairing could be assigned.

5.2.8 Some Comments

Some alternative methods are possible for implementing equation (5.7). We enumerate two of them below.
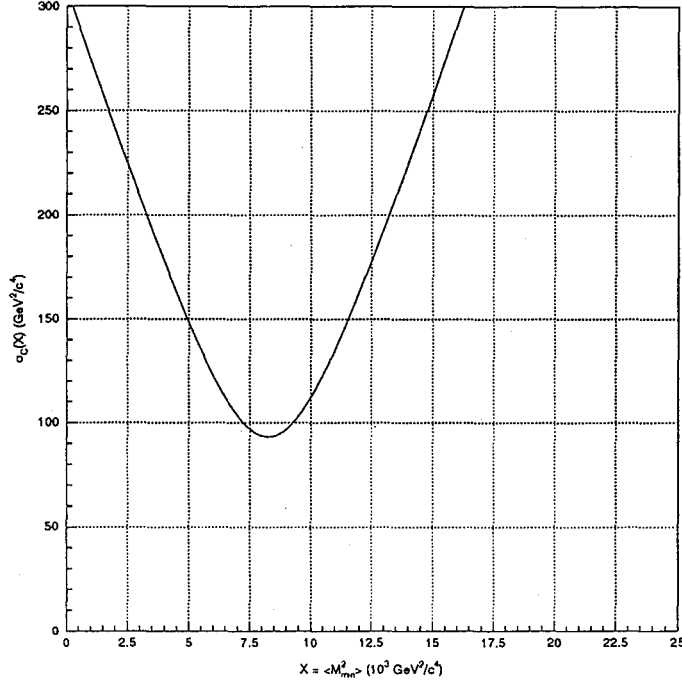
68

Figure 5.14: The $\sigma_C(\langle M^2_{min} \rangle)$ term in the statistical uncertainty of $\langle M^2_{\ell b} \rangle$ from measured $\langle M^2_{min} \rangle$.

1. One may parameterize the relation of $\langle \cos \theta_{\ell b} \rangle$ vs M_t shown in figure 5.4 and insert $\langle \cos \theta_{\ell b} \rangle$ as a function of M_t into the equation, and solve M_t. We tested this possibility. The monte carlo statistics is not enough to get an accurate relation between $\langle \cos \theta_{\ell b} \rangle$ and M_t, but we fit them to a straight line, with χ^2 of 6.83/7. Then after some re-arrangement of terms equation (5.7) becomes a cubic equation of M_t, and one can have an analytical solution. We found that we can obtain M_t with 3 GeV/c^2 accuracy comparable to the method developed in previous sections, but not better. However, the analytical form of $M_t(\langle M^2_{\ell b} \rangle)$ is complicated and the propagation of error is pretty complex.

2. One may device a correspondence function between $\langle M^2_{min} \rangle$ and standard model value of $\langle M^2_{\ell b} \rangle$, and use standard model value of $\langle \cos \theta_{\ell b} \rangle = M^2_W/(M^2_t + 2M^2_W)$ in equation (5.7). We also tested this possibility. Numerically, it yields the same results.
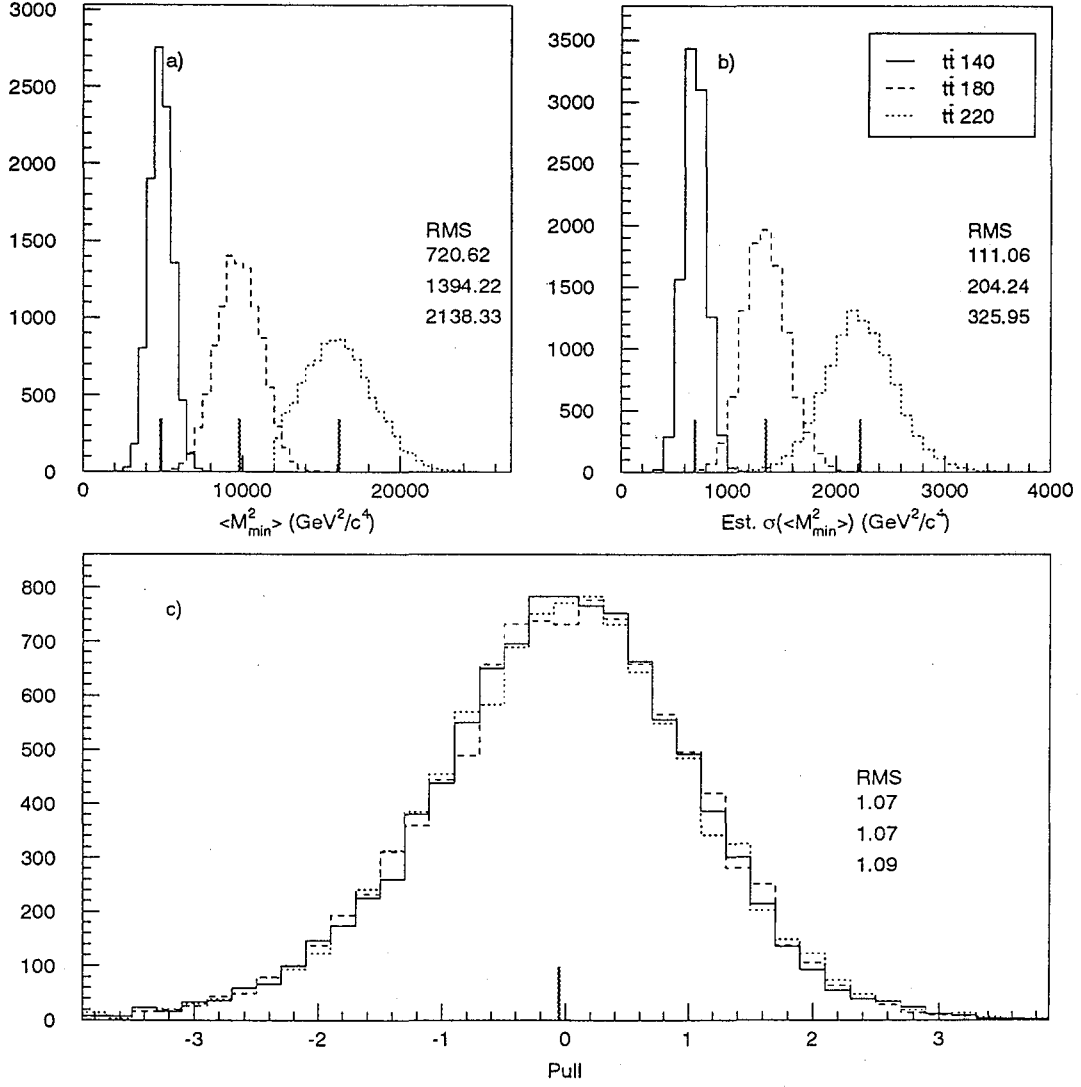
Figure 5.15: $\langle M_{min}^2 \rangle$ distribution in pseudo experiments with input $M_t = 140$, 180 and 220 GeV/c^2. Top left: $\langle M_{min}^2 \rangle$. Top right: Estimated statistical error $\sigma \langle M_{min}^2 \rangle = \mathrm{RMS}(M_{min}^2)/\mathrm{sqrt}(2\mathrm{N})$. Bottom: Pull distribution.

70
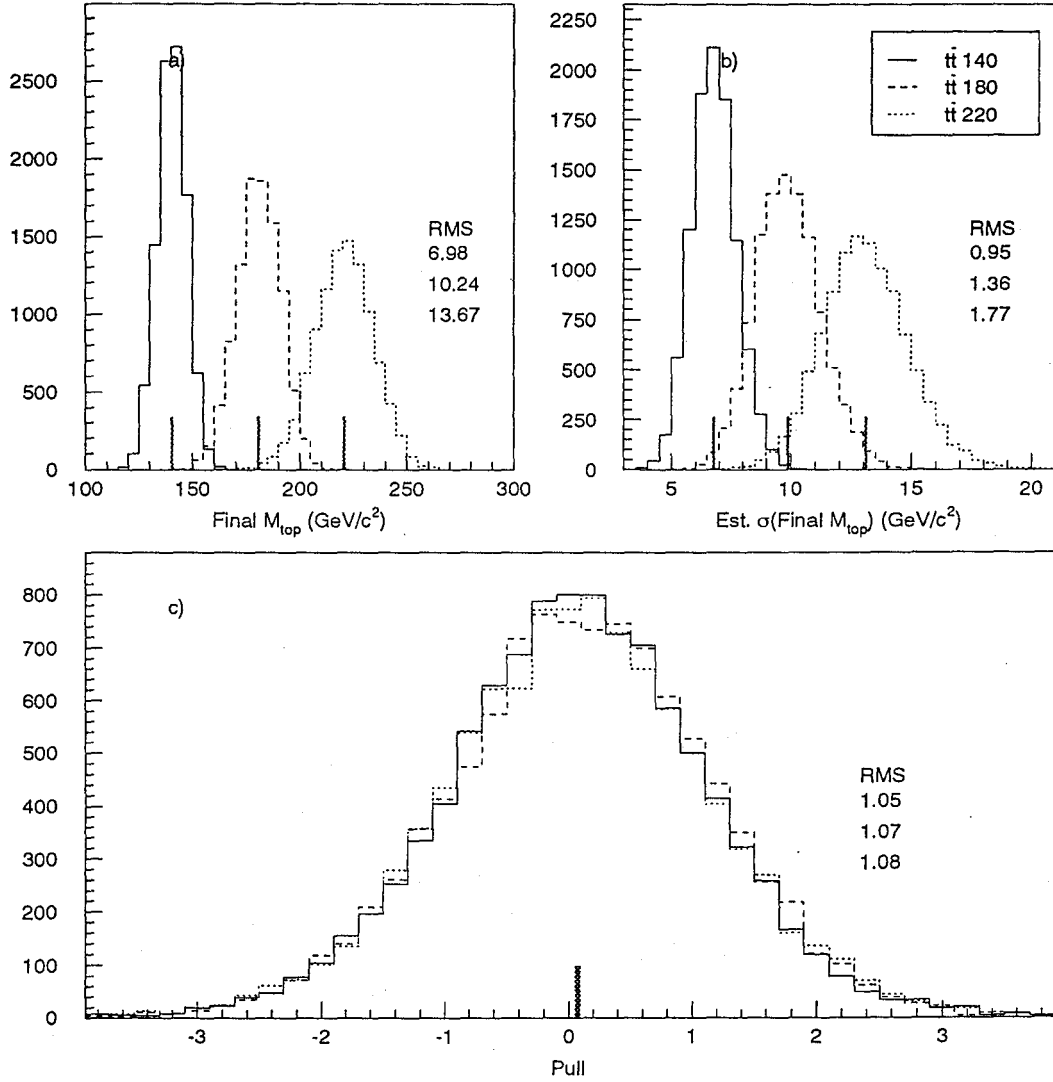
Figure 5.16: Final M_t distribution from $\langle M^2_{min} \rangle$ pairing in pseudo experiments with input $M_t = 140$, 180 and 220 GeV/c². Top left: Final M_t. Top right: Estimated statistical error σ_{M_t} from eq. (5.15). Bottom: Pull distribution.

Generic Monte Carlo or Data

Event Selection

Monte Carlo Signal Sample
or
Data Candidates

Selection bias changes
$\cos\theta_{\ell b}$ and $M^2_{\ell b}$
distribution and their means

$\langle M^2_{min}\rangle$

Correspondence
Function

$C_0 + C_1 X$

Expected $\langle M^2_{\ell b}\rangle$

$M^2_t \approx M^2_W + M^2_b + 2\langle M^2_{\ell b}\rangle/(1-c)$

Raw M_t

Correspondence
Function

$B_0 + B_1 X$

Final M_t

Figure 5.17: Flow chart of the method.

The method is developed entirely on generator information of 4-vectors of leptons and b quarks. Switching to reconstructed data level with JTC96S jet correction doesn't change the conclusion muc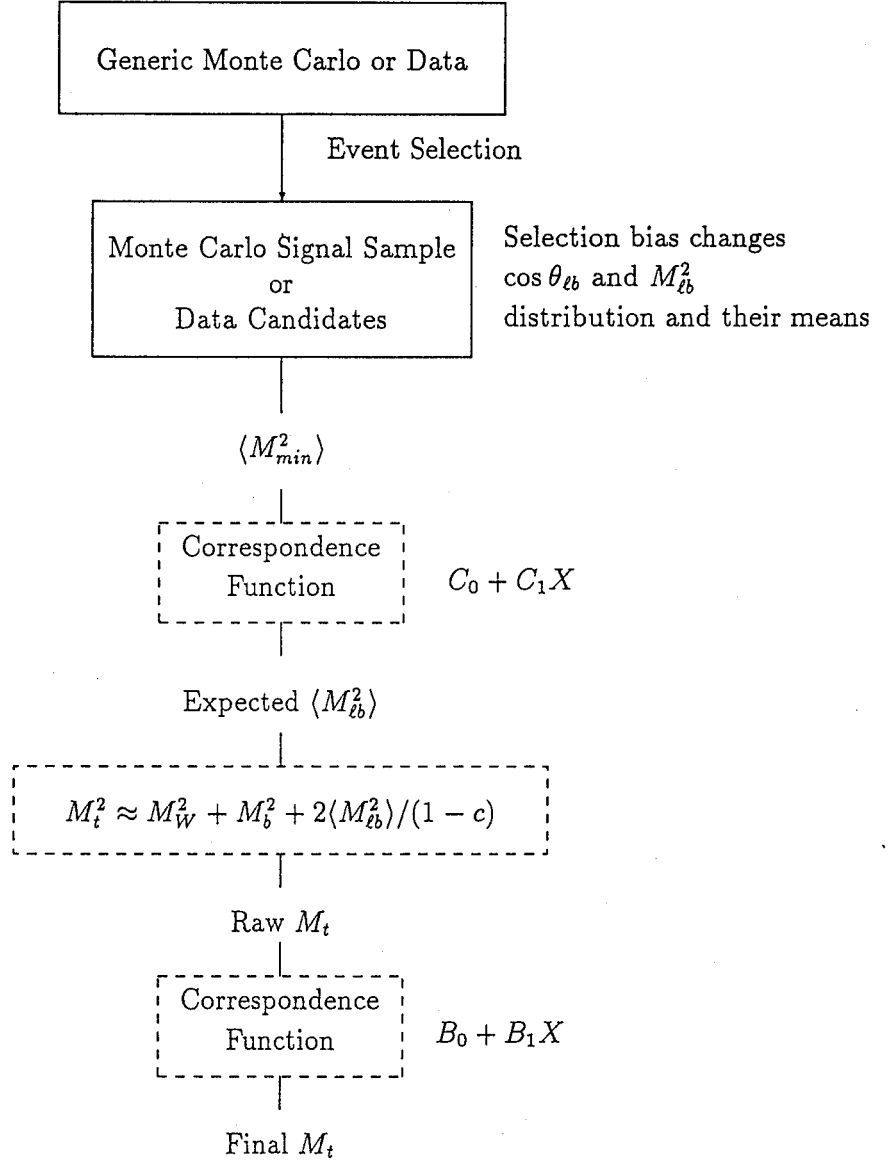h. The mean value of final M_t is shifted slightly (about 2.5 GeV/c² at the $M_t = 220$ GeV/c² sample, which is $\approx 1.1\%$). The width of $\langle M^2_{min} \rangle$ distribution is larger, but it can be estimated by $1.10 \times \text{RMS}/\sqrt{2N}$. With generator 4-vectors the multiplicative factor is 1.07. See Figure 5.18.

5.3   Effects on M_t due to Other $t\bar{t}$ Decay Modes

Here we consider the effect on the top quark mass measurement from $t\bar{t}$ events that don't support the

$$t\bar{t} \rightarrow W^+ b W^- \bar{b} \rightarrow \ell^+ \nu b \ell^- \bar{\nu} \bar{b}$$

hypothesis. We will first identify different $t\bar{t}$ event types and estimate fraction of events of each type, then measure $\langle M^2_{min} \rangle$ in each type of events, and re-derive the correspondence function to incorporate all types of $t\bar{t}$ events.

5.3.1 $t\bar{t}$ Event Types

We categorize $t\bar{t}$ dilepton events by the sources of two identified leptons and two leading jets. Three types of leptons are: "W" type lepton from direct $W \rightarrow \ell\nu$ decay, "τ" type lepton from the cascade decay $W \rightarrow \tau\nu \rightarrow \ell\nu\nu\nu$, and "b" type lepton from $b \rightarrow \ell X$ or $b \rightarrow cX \rightarrow \ell X$. And we have 2 types for jets. A jet is of type "b" if it matches to a generator level b particle or $\bar{b}$ particle within a cone of $\Delta R < 0.4$, otherwise it is labeled as type "g". Here type "g" was meant for gluons, but it also includes (1) b quarks that split into 2 jets, (2) b quarks that emits a hard lepton and the resulting c particle recoiled, or (3) b jets that end up outside the cone of $\Delta R < 0.4$. For the purpose of mass study, as long as a jet doesn't match to the original b particle, the jet no longer presents the b quark at the $t - b - W$ vertex on which the analysis in based, and introduces a shift on M_t measurement.

"τ" type leptons or "b" type leptons tend to be softer than "W" type leptons. And, jets from gluon radiations are also softer than b-jets in average. One of the reason why they can be among the
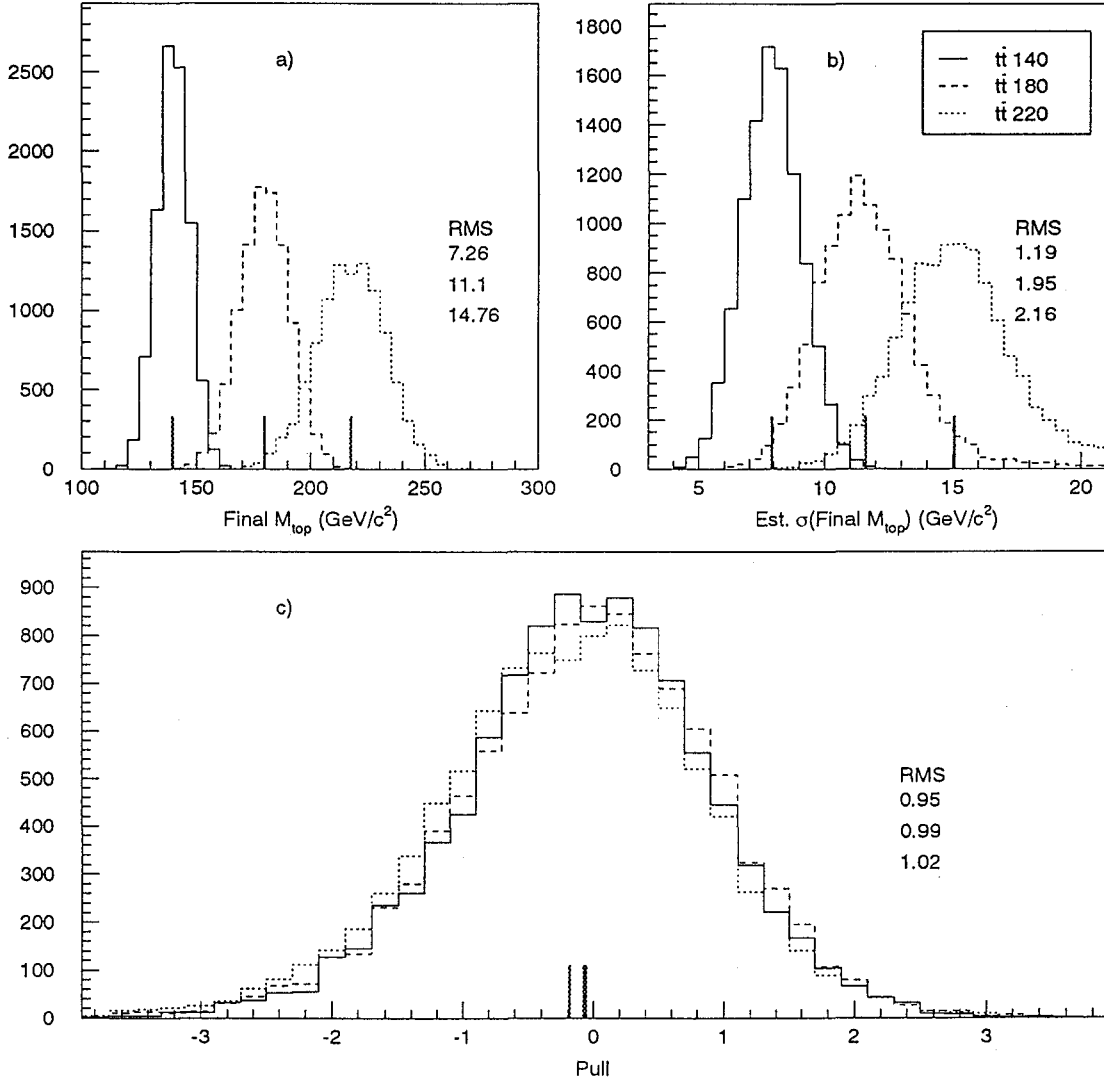
Figure 5.18: Similar figure as figure 5.16 but reconstructed data are used for 4-vectors of objects. Top left: Final M_t. Top right: Estimated statistical error σ_{M_t} from eq. (5.15). Bottom: Pull distribution. We use $\sigma\langle M_{min}^2 \rangle = 1.10 \times \text{RMS}/\sqrt{2N}$.

2 leading jets is that the b-jets sometimes are in the forward region and are out of our acceptance.

Given the above definitions, we can categorize any $t\bar{t}$ dilepton event by the sources of dileptons and dijets. For example, "WWbb" type is the perfect type for our method, "Wτbb" type has one "τ" type of lepton, "WWbg" type has one "g" jet, ..., and so on.

We use the HERWIG dilepton sample to estimate the fraction of each type of events and we show them in figure 5.19.

The fraction of events with one "g" jet in the 2 hardest jets is $\approx 25\%$ and approximately 2% of all events have 2 "g" jets. The perfect "WWbb" type of events is about 60%, and increases with M_t. This can be understood that as M_t goes higher, the b-jets get harder, but gluons from initial state radiations essentially stay M_t-independent. Final state radiation gets harder, too, but in average b-jets have more chance to rank in first or second in E_T when top is heavy.

The first 4 types of events constitutes about 96% of all $t\bar{t}$ dilepton events and non of the rest of the types have fraction larger than 2%. We will ignore them entirely and scale up the first 4 types to 100%.

We list the percentages of each type of events for true $M_t = 140$, 180 and 220 GeV/c^{2}in table 5.2.

Type	140	180	220
WWbb	58.9±1.75	63.0±1.44	64.7±1.40
WWbg	26.6±1.58	20.9±1.21	17.6±1.12
Wτbb	7.12±.918	8.36±.826	11.0±.918
Wτbg	3.69±.672	3.20±.525	2.93±.496
WWgg	1.53±.437	1.33±.342	1.73±.383
Wbbg	1.02±.358	.979±.294	.518±.211
Wτgg	.254±.180	.267±.154	.259±.149
Others	.891±.335	1.96±.413	1.29±.332

Table 5.2: Percentages of 7 $t\bar{t}$ event types in 3 HERWIG dilepton samples.
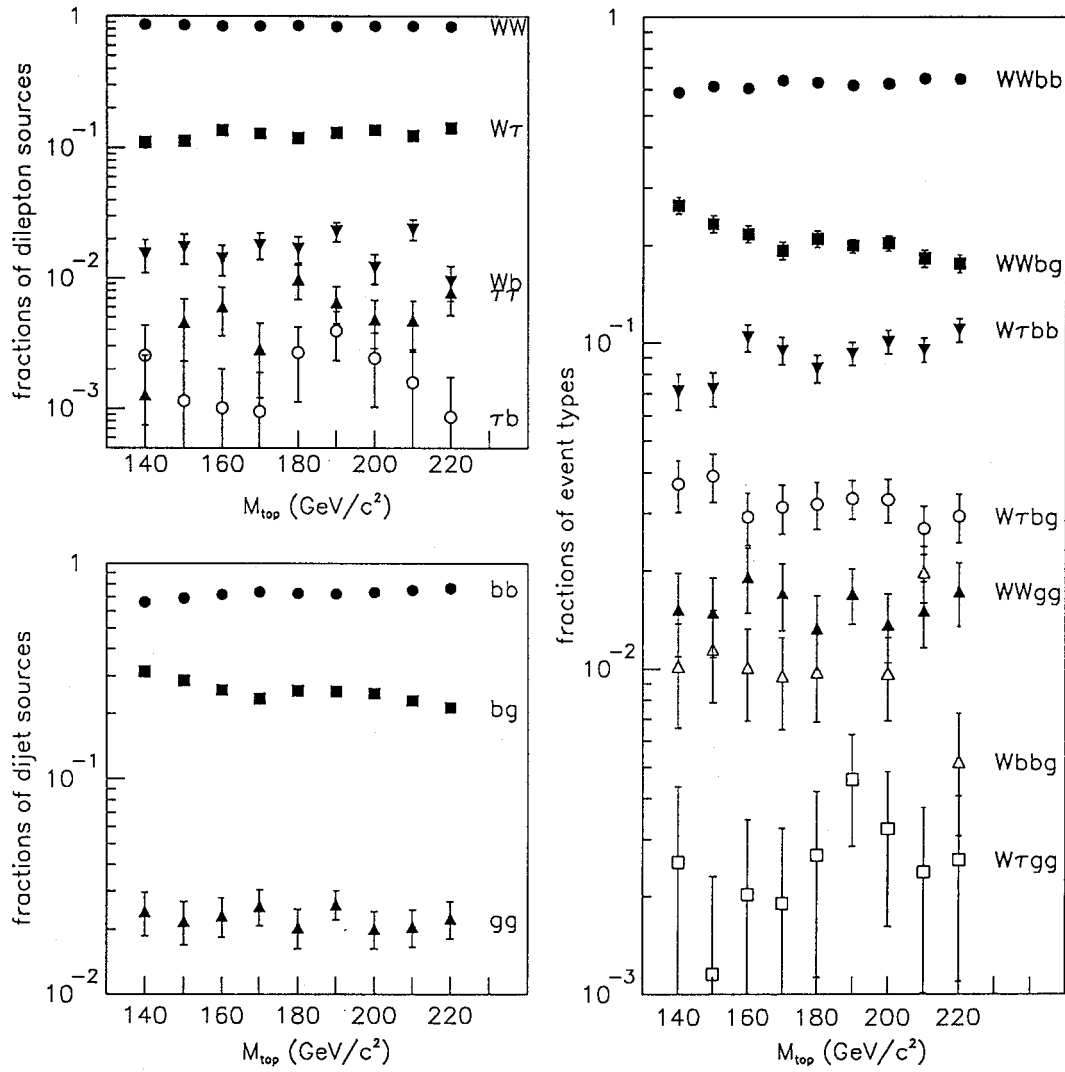
Figure 5.19: Top left: fractions of each type of dileptons for M_t=140 GeV/c^2 to 220 GeV/c^2. The lepton types are defined in text. Bottom left: the fractions of each source of dijets for the same range of M_t. See text for definition of jet sources. Right: fractions of different event types. Event type are categorized by dilepton source and dijet source. Event types that have fractions less than 10^{-3} are not shown.

5.3.2 $\langle M_{min}^2 \rangle$ Distribution

The distribution of $\langle M_{min}^2 \rangle$ of WWbb, WWbg, Wτbb and Wτbg types of events in $M_t = 160$ GeV/c^2 sample are shown in figure 5.20. We see that Wτbb and Wτbg have slightly softer spectra than WWbb because of the cascade decay of W, but there is a long tail in WWbg events. This can be understood that gluons tend to have random angles with respect to leptons and it is possible to have a hard gluon at a large angle to a lepton, and forms a large invariant mass.

The scatter plot of $\langle M_{min}^2 \rangle$ vs M_t for each event type are shown in figure 5.21. All non-WWbb types of events has lower $\langle M_{min}^2 \rangle$ at high top mass. But in the low top mass region ($M_t < 170$ GeV/c^2) the difference is less significant. This is consistent with the tail we see in the M_{min}^2 distribution.

5.3.3 M_t Determination with All Types of t$\bar{\text{t}}$ Events

In general, non-WWbb type of t$\bar{\text{t}}$ events have smaller $\langle M_{min}^2 \rangle$, and gives smaller final M_t if we apply our method on them. See figure 5.22 for a plot of right pair $\langle M_{min}^2 \rangle$ vs $\langle M_{min}^2 \rangle$ in the HERWIG dilepton sample, where no requirement on event types are made. The raw M_t is shifted downward for most of the monte carlo points. The shift is most apparent at true $M_t = 220$ GeV/c^2 sample, the highest true top mass sample we have, where raw M_t moves from 224.8 GeV/c^2 to 213.3 GeV/c^2.

We can re-define the correspondence function C: $\langle M_{min}^2 \rangle \rightarrow \langle M_{tb}^2 \rangle$ in HERWIG dilepton sample so the effect of non-WWbb types of events can be included. We fit the points in figure 5.22 to a straight line $\langle M_{tb}^2 \rangle = C_0 + C_1 \langle M_{min}^2 \rangle$ and this is the new correspondence function. The parameters are found to be $C_0 = -2688. \pm 291., C_1 = 1.55 \pm 0.0335$, and $V_{C_0 C_1} = -9.24$.

One effect of the non-WWbb types of events on top quark mass measurement is that it reduces the sensitivity of the method. This can be quantitatively realized on the value of C_1. With only WWbb type, $C_1 = 1.27$. With every type included, $C_1 = 1.55$. This means, instead of enlarging the statistical uncertainty by 27%, we have to magnify it by 55%. This reduces the discriminating power on M_t.
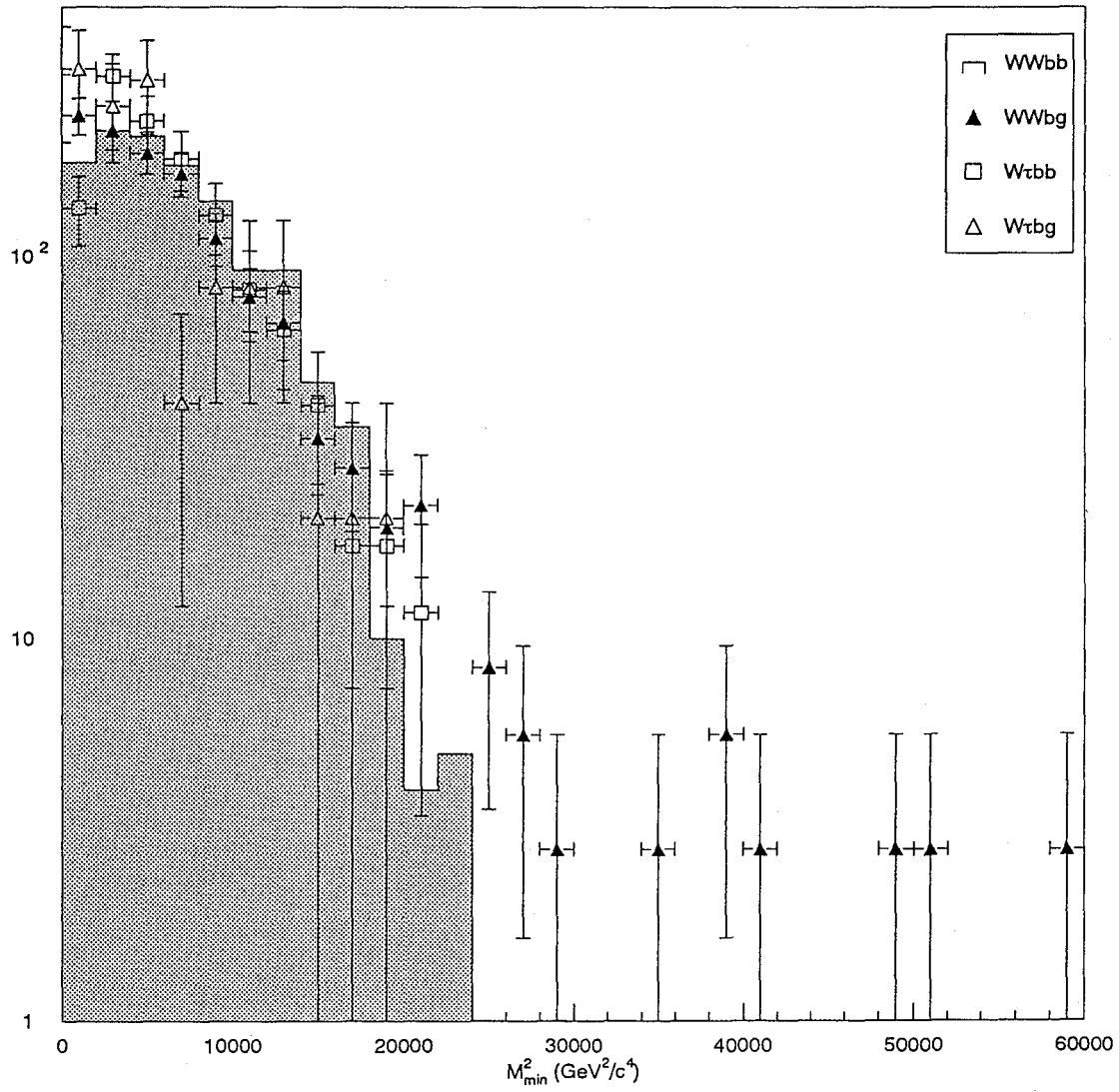
Figure 5.20: The distribution of M^2_{min} in 4 different types of $t\bar{t}$ events in $M'_t = 160$ GeV/c^2 sample.
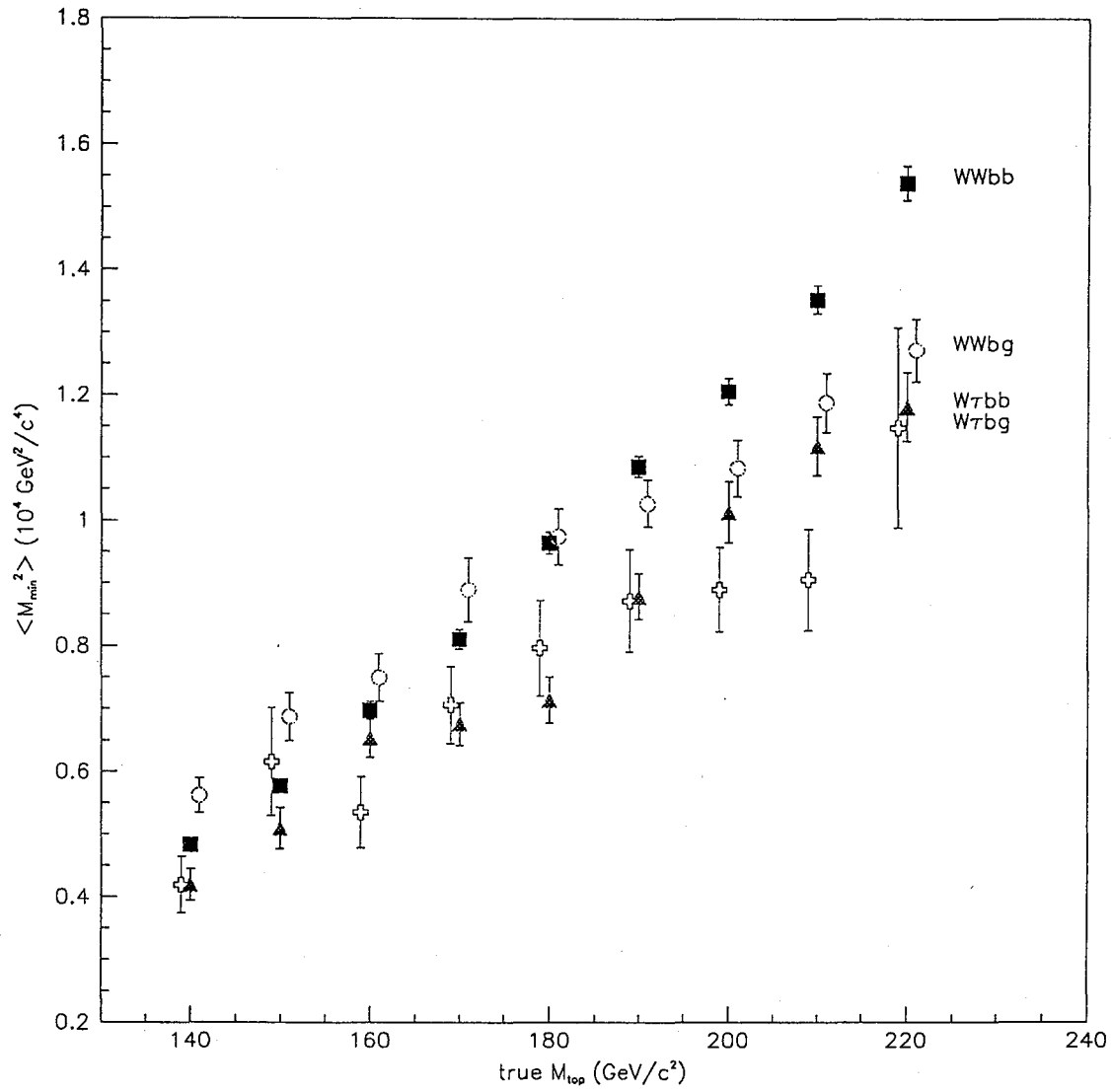
Figure 5.21: $\langle M^2_{min} \rangle$ vs true M_t in 4 different types of $t\bar{t}$ events: WWbb, WWbg, Wτbb, Wτbg. We've shifted points of WWbg and Wτbg horizontally by 1 GeV/c^2 to avoid overlapping error bars.
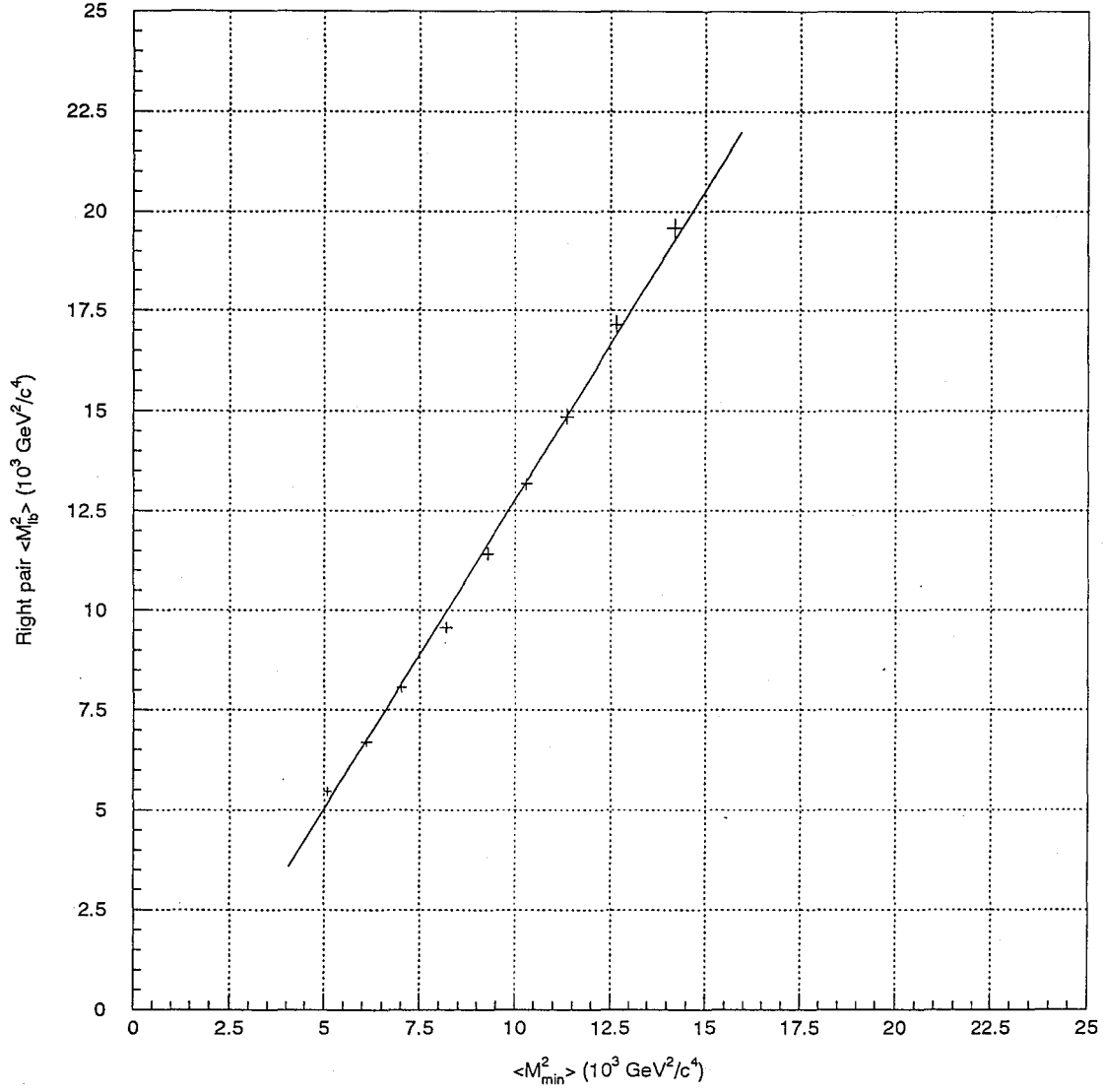
Figure 5.22: Right pair $\langle M_{\ell b}^2 \rangle$ vs $\langle M_{min}^2 \rangle$ in HERWIG dilepton sample. All $t\bar{t}$ dilepton event types are included and reconstructed data are used. The linear fit is also shown.
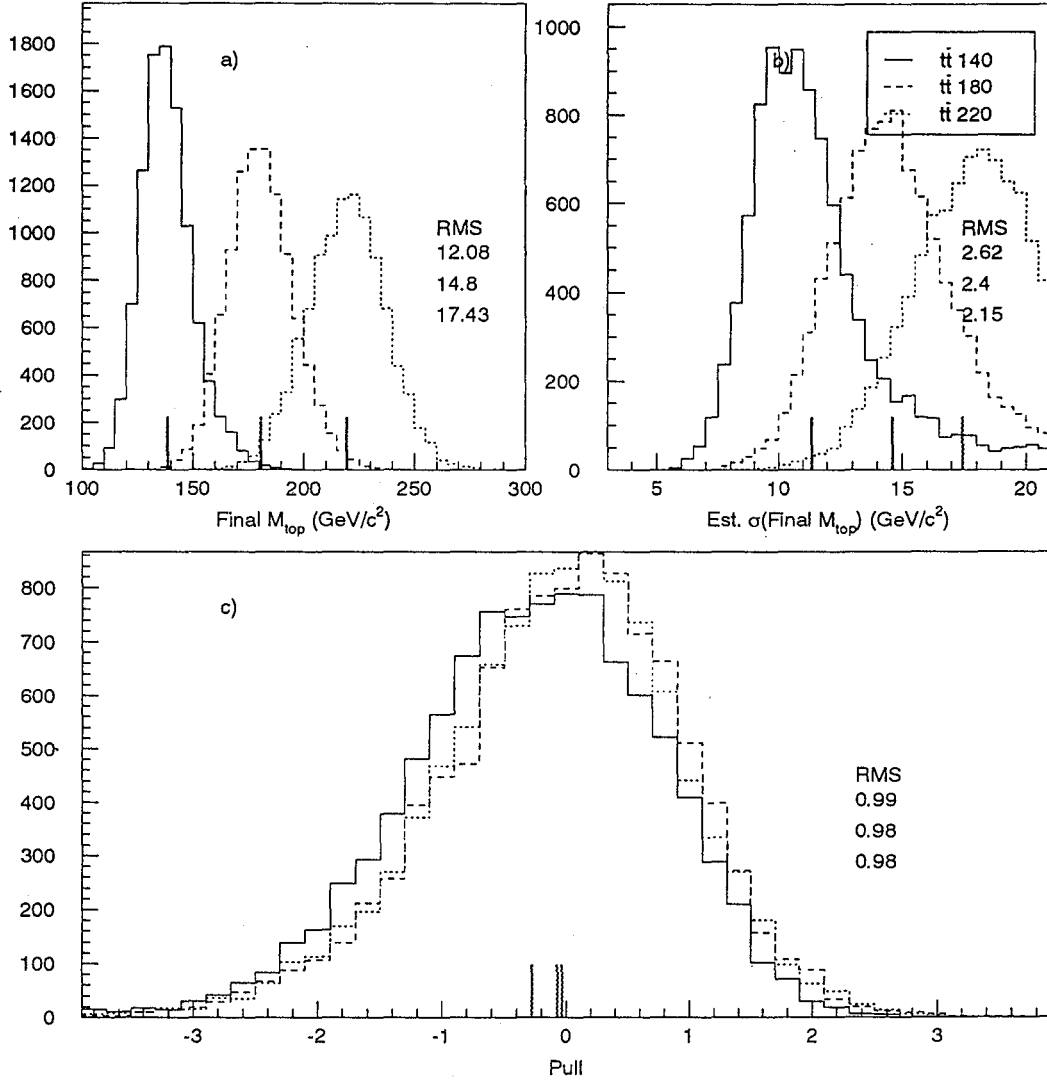
Figure 5.23: Final M_t distribution from $\langle M_{min}^2 \rangle$ pairing in pseudo experiments with input $M_t = 140$, 180 and 220 GeV/c². All types of $t\bar{t}$ events are included. We have used $\sigma\langle M_{min}^2 \rangle = 1.14 \times \text{RMS}/\sqrt{2N}$ in order to obtain correct estimate of statistical uncertainty of $\langle M_{min}^2 \rangle$. Top left: Final M_t. Top right: Estimated statistical error σ_{M_t} from eq. (5.15). Bottom: Pull distribution.

With the new correspondence function, we can again check the pull distribution in pseudo experiments. In order to have a better estimate of $\sigma \langle M_{min}^2 \rangle$, in Figure 5.23 we have multiplied RMS/$\sqrt{2N}$ by 1.14 (for WWbb type alone, this factor would be 1.07). The pull distribution is wider on the negative side. This indicates that we have more chance to under-estimate statistical uncertainty rather than over-estimate it. This is caused by the long tail in WWbg events which increases both $\langle M_{min}^2 \rangle$ and $\sigma \langle M_{min}^2 \rangle$ in the whole monte carlo sample significantly. But when we make an experiment of 10 events, we often get 0 events from the tail and obtain a smaller mean and a smaller RMS. So more than 50% of experiments end up in the negative side of the pull distribution and make it asymmetric.

The presence of non-WWbb $t\bar{t}$ events has reduced the sensitivity of the method by 19% for M_t=220 sample and 66% for M_t=140 sample. The biggest impact is from "g" type of jets. It has 2 effects:

1. Long tails in M_{min}^2 distribution makes the multiplicative factor increase from 1.07 to 1.14, a 6.5% increase.

2. Low $\langle M_{min}^2 \rangle$ makes the slope of correspondence function increase from 1.27 to 1.55, a 22% increase.

If we can eliminate events with "g" jets we can gain some discriminating power, but lose $\approx$ 30% of statistics. Raising jet threshold or require b-tagging are two possible ways for future improvements.

5.3.4 The Statistical Uncertainties in Different Conditions

The expected statistical uncertainties with 10 events in different conditions are summarized in Table 5.3.

We see that in the ideal case (WWbb GENP right pairs) the statistical uncertainty is 7.8 GeV/c² in the $M_t = 180$ GeV/c² sample. The current pairing method works in getting the right mass and estimating the statistical uncertainty correctly at the expense of increasing statistical uncertainty by

True M_t	140	180	220
WWbb GENP right pairs	5.4	7.8	9.6
WWbb GENP M^2_{min}	7.0	10.2	13.7
WWbb rec. M^2_{min}	7.3	11.1	14.6
All types rec. M^2_{min}	12.1	14.8	17.4

Table 5.3: Expected statistical uncertainties of final M_t from 10 events under different conditions. The units are GeV/c².

30% to 10.2 GeV/c². Switching to using reconstructed data doesn't cost too much (9%). However, the presence of "g" type of jets increases the statistical uncertainty by another 33% to 14.8 GeV/c².

We summarize the method and coefficients of correspondence functions in Figure 5.24.

5.4 Effect on M_t Measurement from Background Events

In this section we consider the effect on the top quark mass measurement from background events. The expected number of background events in dilepton data sample is described in Section 4.7 and is listed in table 4.4.

5.4.1 M^2_{min} Distribution in Background Events

W⁺W⁻

We use monte carlo samples to study the M^2_{min} distribution of $W^+W^- + 2$ jets events. We have used 3 different generators:

1. Tao Han $W^+W^- + 2$ jets matrix element monte carlo sample.

2. PYTHIA W^+W^- sample.

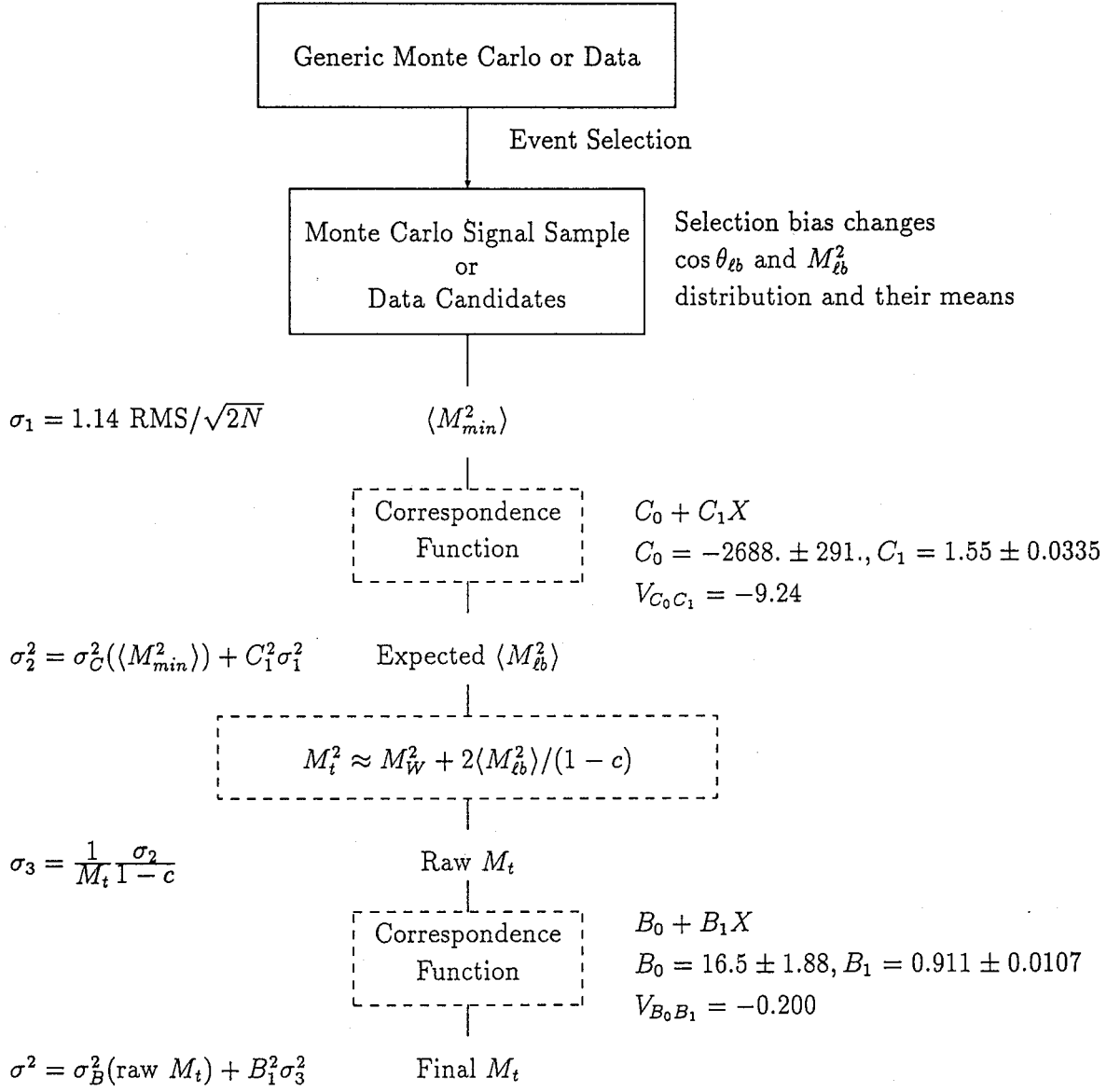3. ISAJET W^+W^- sample.

83

Figure 5.24: Summary of the method.

At first we examine the P_T distributions in those 3 generators. See figure 5.25. We see that all 3 generators give similar distributions for both leptons, while matrix element calculation gives harder leading jet. This is related to the fact that we set $Q^2 = M_W^2$ instead of $Q^2 = \langle P_T^2 \rangle$ in the generator.

Naturally we expect that Tao Han monte carlo with this Q^2 gives a harder M_{min}^2 distribution. It is shown in figure 5.26.

Z→ $\tau\tau$

We use ISAJET $Z \rightarrow \tau^+\tau^-$ sample to study the background shape of $Z \rightarrow \tau^+\tau^-$ events. We are in the process of making a PYTHIA sample at this moment.

Drell-Yan

We don't have Drell-Yan sample right now. But we can use dilepton + dijet data as a good approximation of Drell-Yan sample. In order to increase statistics we don't apply the isolation cuts and missing E_T cuts, but Z window cut is retained to reject Z's.

Fake Leptons

The background from events with one fake leptons are estimated from events with one good lepton, one denominator lepton, $\not{E}_T$ and 2 jets. For our mass analysis, we use the same set of events to get the M_{min}^2 distribution.

Figure 5.27 shows the M_{min}^2 distribution for background events.

5.4.2   Expected Shift of M_t due to Backgrounds

We can do pseudo experiments with appropriate background mixture to examine the shift of final M_t from background events.

We use the following procedure:

1. Make a pool of signal and background events by mixing them in proper fractions and attempt to get as many events as possible. The proper fractions of backgrounds are taken from the
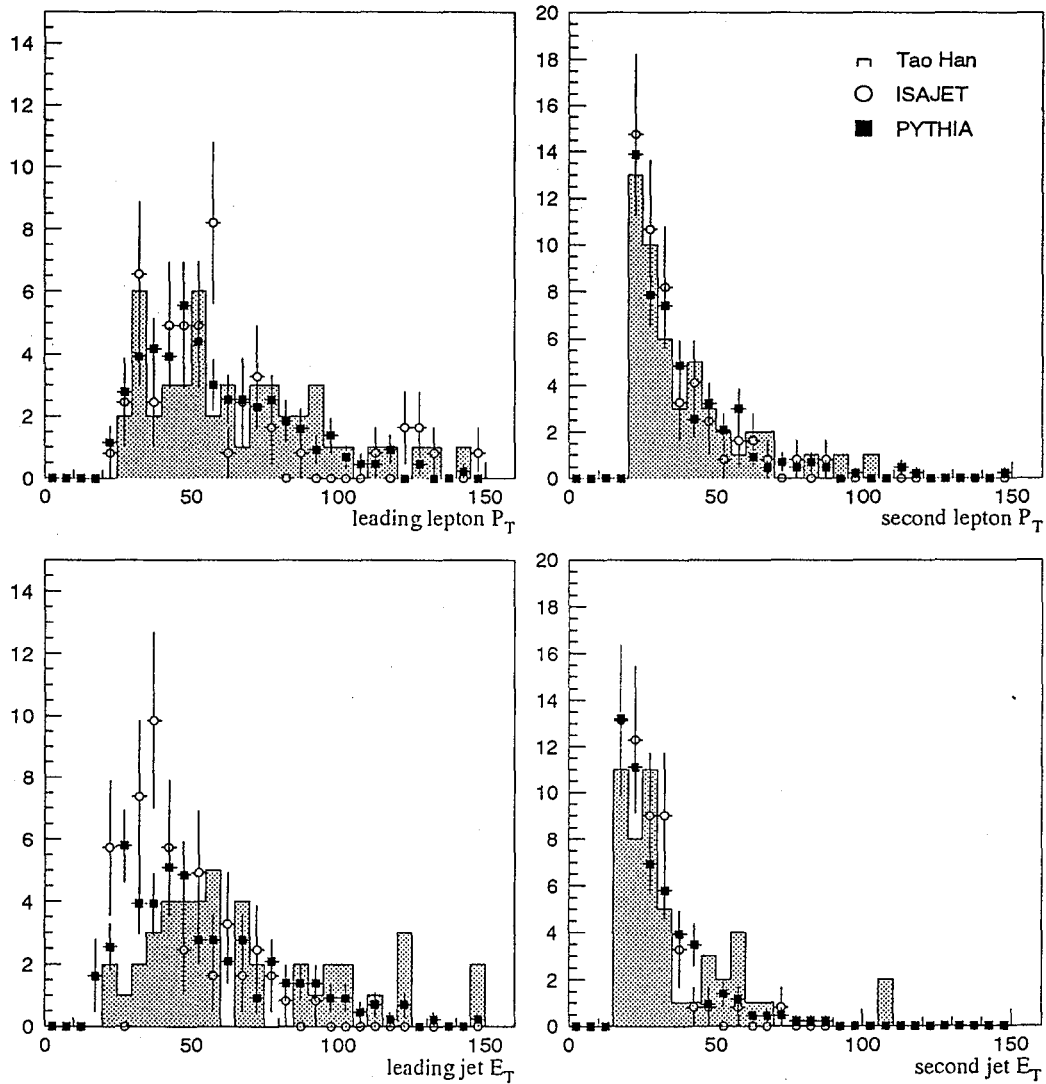
Figure 5.25: The P_T distributions of leptons and jets. Hatched histogram: Tao Han WW+2J matrix element monte carlo, black squares: PYTHIA, open circles: ISAJET. PYTHIA and ISAJET are normalized to Tao Han. The main difference is on the leading jet E_T distribution, where Tao Han matrix element calculation apparently gives harder leading jet.

Figure 5.26: The distribution of M_{min}^2. Legends are the same as figure 5.25. Tao Han matrix element calculation gives harder spectrum because we imposed $Q^2 = M_W^2$.

Figure 5.27: The distribution of M^2_{min} of all four backgrounds.

standard background estimate, and the fractions of $t\bar{t}$ events are calculated as

$$F_i = (1 - \frac{\sum N_B}{N_{Data}}) * P_i,$$

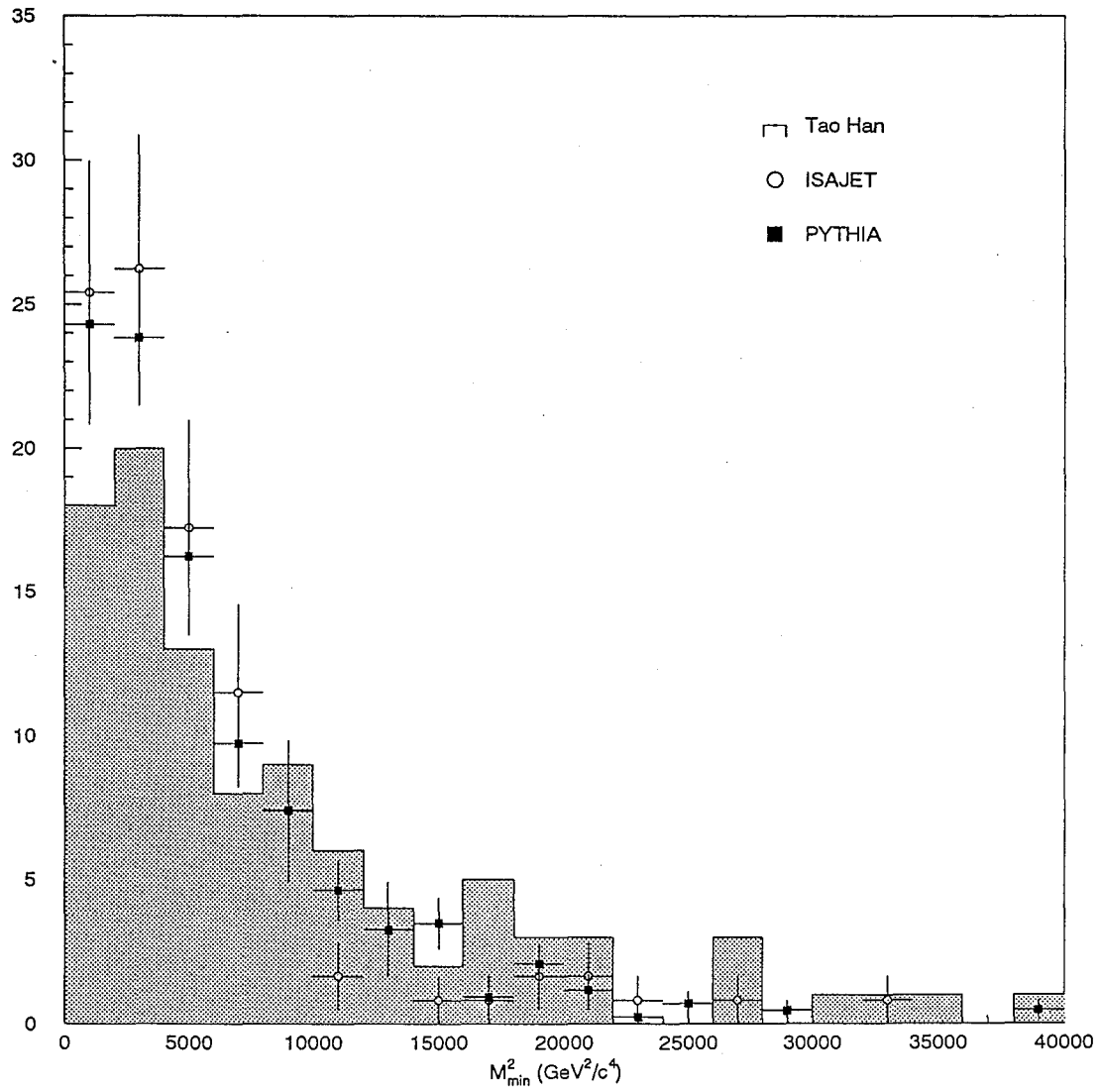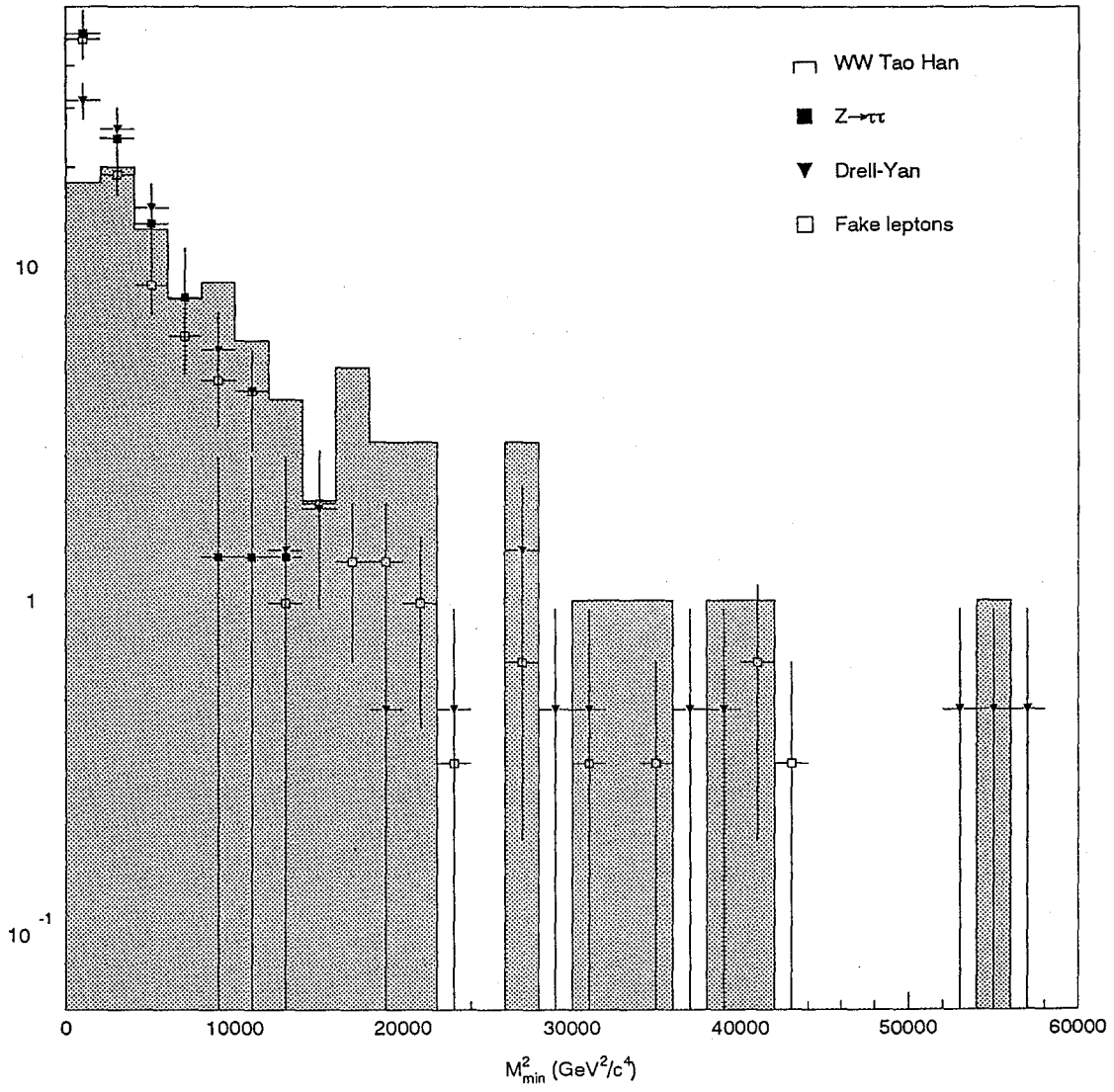where $\sum N_B$ is the expected number of total background events (2.0), N_{Data} is number of observed candidates (10), P_i is the fraction of each $t\bar{t}$ types obtained in previous section, and F_i is the expected fraction of each $t\bar{t}$ types in the whole data. $\sum_i F_i + \sum N_B/N_{Data} = 1$.

Because of the limited statistics in $Z \to \tau^+\tau^-$ monte carlo sample, we end up with 300/270/597 events in the pool for $e\mu$, $ee\mu\mu$ and combined categories, respectively.

2. Randomly select N_{Data} events from the pool to form a pseudo experiment, Measure the final M_t in the pseudo experiment.

3. Repeat this procedure many times and check the distribution of final M_t to determine the mass shift.

The distributions of M_{min}^2 of various backgrounds have been shown in Figure 5.27. We have the following observations:

1. Drell-Yan, Fakes or $Z \to \tau^+\tau^-$ backgrounds are expected to shift $\langle M_{min}^2 \rangle$ in experiments to smaller values.

2. W^+W^- background is $\approx t\bar{t}$ 180 effectively.

We also attempted to vary the expected number of backgrounds up and down by 1 σ and repeat the pseudo experiments. This can serve as an estimate of maximum and minimum 1 σ shift of M_t. The results are listed in Table 5.4.

We see that the shift of mean final M_t for the 160 GeV/c^2 sample is -2.9±1.8 GeV.

89
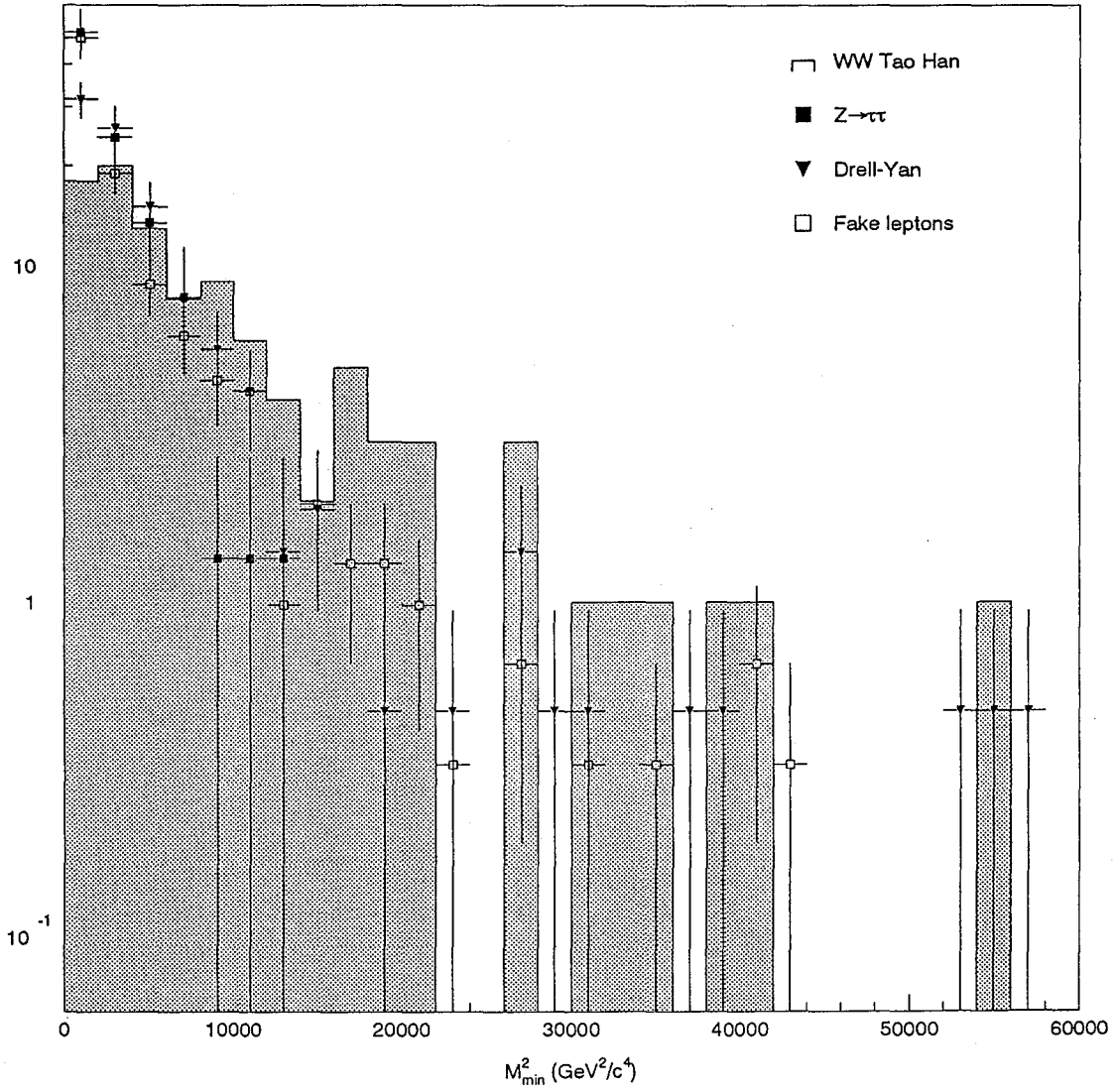
Figure 5.28: $\langle M_{all}^2 \rangle$ in various samples. The grey bands are W^+W^-, Drell-Yan, Fakes and $Z \to \tau^+\tau^-$ backgrounds which are considered M_t independent. Black squares are signal as a function of true M_t, open circles are type WWbg, black triangles are type Wτbb, open crosses are type Wτbg. In order to see the error bars clearly, some markers are shifted horizontally by 1 or 2 GeV from true M_t.

true M_t	Mean Final M_t			
	no bkg	nominal bkg	lowest	highest
140	138.0	139.1	137.6	140.6
160	160.1	157.1	155.3	158.8
180	182.6	175.9	173.1	178.6
200	200.1	190.6	186.7	194.5
220	221.7	209.1	203.8	214.2

Table 5.4: Final M_t in 5 samples of different true M_t. "no bkg": pure $t\bar{t}$. "nominal bkg": the nominal number of expected backgrounds are mixed in. "lowest" and "highest": varying number of expected backgrounds up and down 1 sigma (totally 3^4 configurations) and find the smallest M_t and largest M_t.

5.4.3 Reducing Backgrounds

It would be attractive if we can have a cut to reduce backgrounds while keeping most of the signal events. One kinematic variable with the desired feature is the total transverse momentum of the event, H_T, defined as

$$H_T \equiv P_T(lep1) + P_T(lep2) + P_T(jet1) + P_T(jet2) + \not{E}_T.$$

The H_T cut efficiency as a function of H_T cut for $t\bar{t}$ events is shown in Figure 5.29. Figure 5.30 shows the same plot for backgrounds.

We found that by applying an H_T cut at 170 GeV the backgrounds are reduced by 16%, 51%, 77% and 65% for WW, $Z \rightarrow \tau^+\tau^-$, Drell-Yan and fakes, respectively. That reduces the total background to 0.87 events. The $t\bar{t}$ signals are not sacrificed much, with the efficiencies 94% to 100% for $M_t =$ 140 GeV/c^2 to 220 GeV/c^2.

So we apply this H_T cut on all $t\bar{t}$ monte carlo samples and rederive the correspondence functions. The new coefficients are $C_0 = -2981.\pm308.$, $C_1 = 1.60\pm0.0356$, $V_{C_0 C_1} = -10.5$, $B_0 = 15.4\pm1.93$, $B_1 = 0.915 \pm 0.0109$ and $V_{B_0 B_1} = -0.0208$.
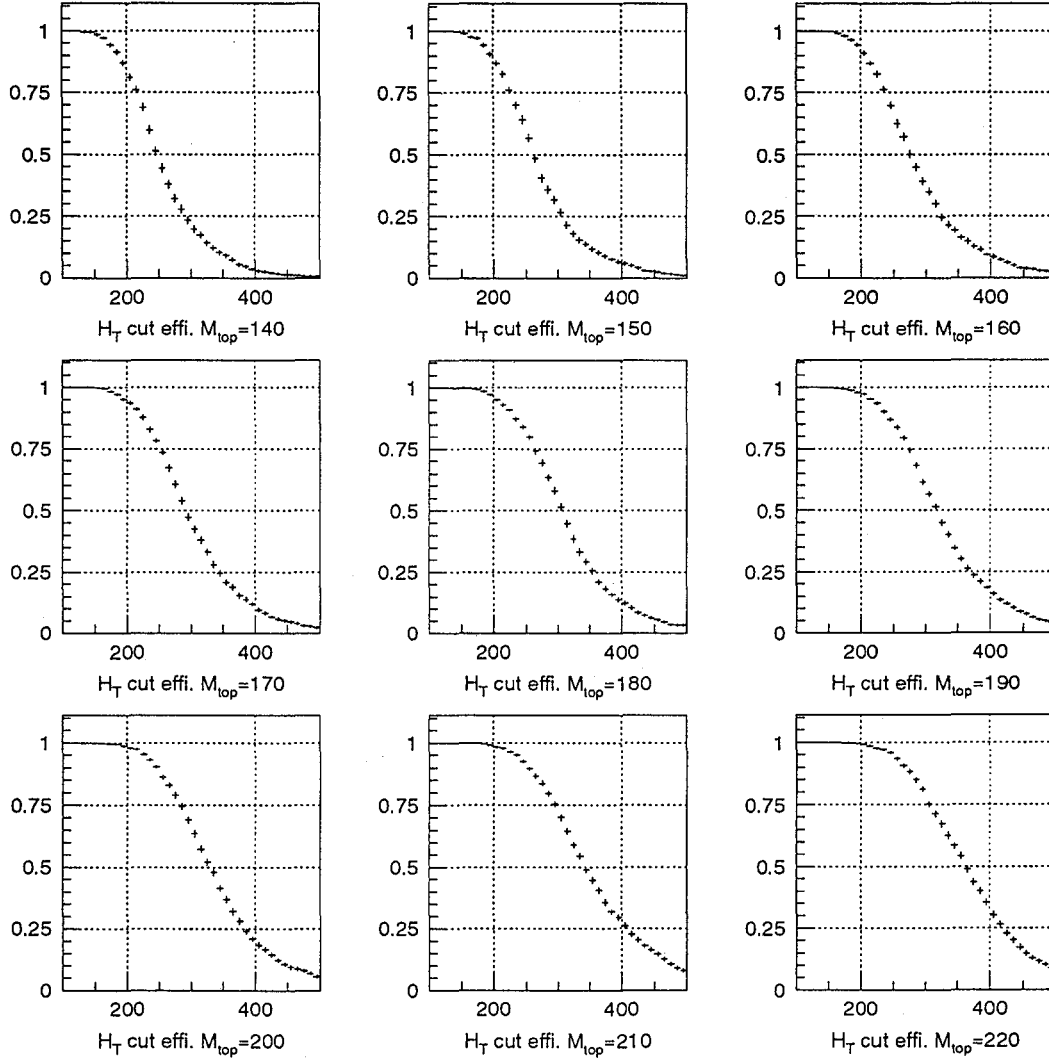
Herwig t̄t MC

Figure 5.29: H_T cut efficiencies as a function of H_T cut in t̄t events.
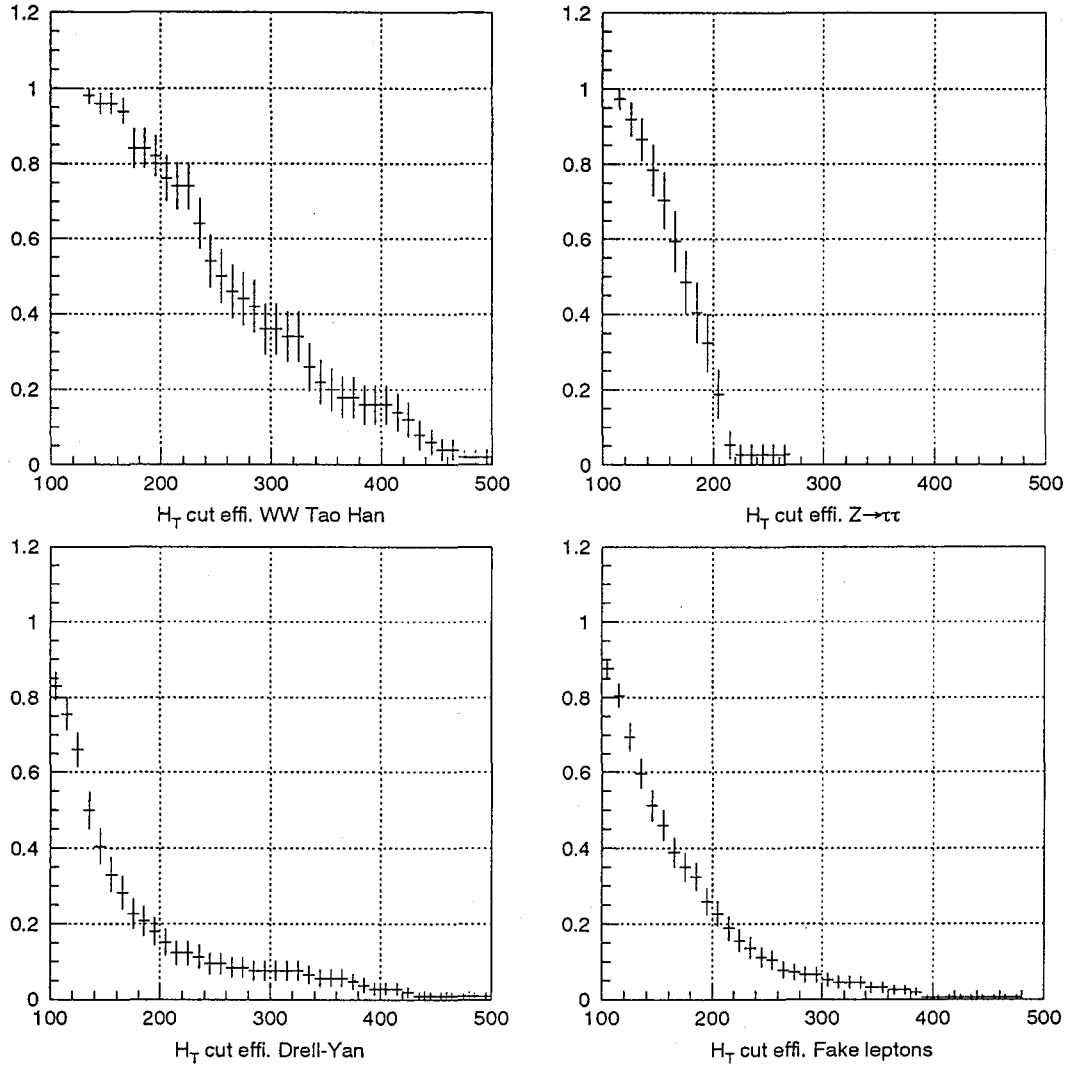
Backgrounds

Figure 5.30: H_T cut efficiencies as a function of H_T cut in background events.

5.5 Data

We list some variables obtained from 10 candidate events in Run 1 in Table 5.5. The events are sorted in H_T.

From table 5.5 we see that an H_T cut at 170 GeV gives $M_t = 163 \pm 21.0$ GeV/c^2.

The two lowest H_T events have no solution for M_t because the $\langle M_{min}^2 \rangle$ is too small and the correspondence function maps them to negative values of $\langle M_{\ell b}^2 \rangle$.

Our mass measurement is based on the mean value of M_{min}^2. As a cross check we compare the M_{min}^2 distribution of data to the expectation from Monte Carlo in Figure 5.31. We see a good agreement between data and $t\bar{t}$ 160 Monte Carlo in the low M_{min}^2 region but it seems we have some upward fluctuation in the high M_{min}^2 region, which increases the RMS of the distribution and results in a larger than average statistical uncertainty.

We compare the statistical uncertainty obtained in data to the expected statistical uncertainty obtained from pseudo experiments in $t\bar{t}$ 160 Monte Carlo in Figure 5.32. We see that the statistical uncertainty in data is about 1.6σ higher than average. This is not too far off and we think it is a pure statistical fluctuation. It is also possible that there are some events from different origin that mixed into the data sample but with limited statistics we can not draw definite conclusions.
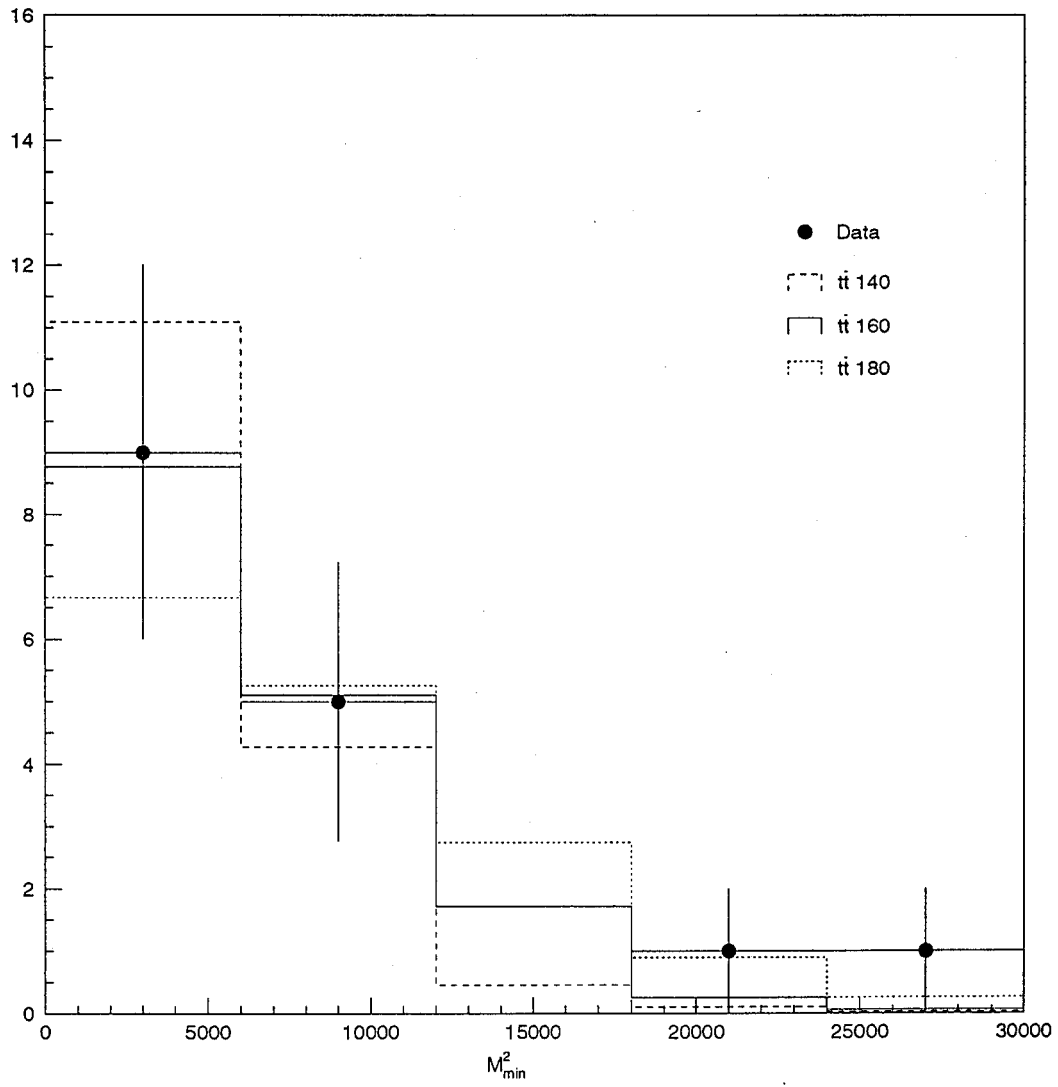
94

Figure 5.31: The distribution of M^2_{min} in data ($\bullet$) and $t\bar{t}$ Monte Carlo with M_t assigned at 140 (dashed histogram), 160 (solid line histogram) and 180 (dotted histogram) GeV/c^2.
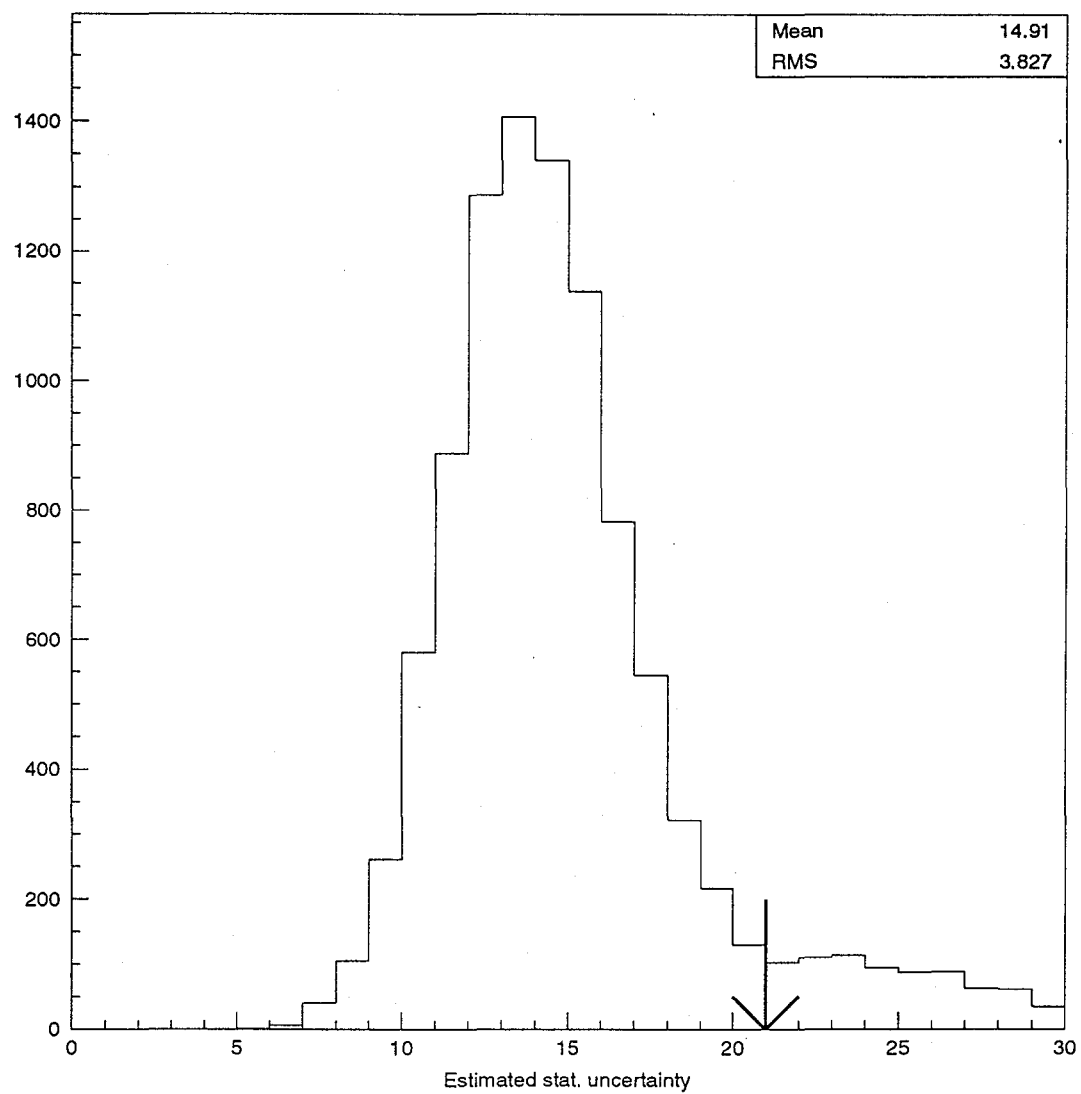
Figure 5.32: The expected statistical uncertainty obtained in pseudo experiments with $t\bar{t}$ 160 Monte Carlo. The arrow indicates the statistical uncertainty in data.

5.6 Systematic Uncertainties

The systematic uncertainties in the M_t determination, summarized in Table 5.6, are presented in this section.

5.6.1 Jet Energy Uncertainties

The old way of estimating jet energy uncertainty is assuming that it is 10% of the jet energy. Multiply the fully corrected jet energies by 1.1|0.9 results in mass shifts of +6.7 and -7.1 GeV/c².

The more detailed way is to study the jet energy measurement and correction, and estimate the uncertainty introduced in the measurement and each step of the correction.

Jet Energy Measurement Uncertainties

- Calorimeter Stability: The calorimeter response to single tracks (mostly pions) have been studied in Run 1B and compared to Run 0[57]. The calorimeter response is found to change in 2% level. So we add or subtract 2% of raw energy to simulate the change.

- Behrends curve: The absolute jet energy scale is derived from QFL detector simulation program which was tuned to Run 0 data. The uncertainty of jet energy from the absolute jet energy scale, combined with uncertainty of underlying event from the same vertex and Monte Carlo fragmentation modelling has been studied and the result is a curve of uncertainty as a function of parton P_T. The curve is parameterized as

$$\Delta P_T / P_T = 0.0245 + 0.0550/P_T$$

and we add or subtract ΔP_T to P_T after absolute correction to simulate the effect.

Jet Energy Simulation Uncertainties

QFL Energy Shift: A study of add 2% on raw energy.

Jet Energy Correction Uncertainties

- f_{rel} switch: increase or decrease f_{rel} by 2% of $|f_{rel} - 1|$.

- Soft Gluon Radiation: add soft gluon correction to P_T after out-of-cone correction.

- $\pm$ 1 GeV switch: add or subtract 1 GeV from P_T after out-of-cone correction.

5.6.2 Different Generators

We also used PYTHIA v5.7 to generate $t\bar{t}$ 160 Monte Carlo sample (with both initial state and final state radiations turned on because HERWIG has gluons by default). Using the correspondence function dervied from HERWIG sample to calculate M_t in the PYTHIA sample, results in a small shift of $+0.4 \pm 2.3(stat.)$ GeV/c^2.

We assign the systematics as ± 0.4 GeV/c^2.

5.6.3 Initial State / Final State Radiations

By turning OFF the initial state and final state radiations in PYTHIA the measured top quark mass is shifted by $4.2 \pm 3.0(stat.)$ GeV/c^2.

We assign the systematics as ± 4.2 GeV/c^2.

5.6.4 Monte Carlo Statistics

The statistics of the HERWIG samples are already included in our formula of calculating the expected uncertainty through the error propagation.

5.6.5 Fraction of $t\bar{t}$ Event Types

We consider 4 types of $t\bar{t}$ events: WWbb, WWbg, Wτbb, Wτbg. For HERWIG $t\bar{t}$ sample with $H_T > 170$ GeV cut, the fraction of each type is 61.4%$\pm$1.1%, 21.1%$\pm$0.9%, 10.6%$\pm$0.6% and 2.9%$\pm$0.3%, respectively. It is very conservative to allow the first two fractions to float up and down by 20%

98

(absolute) and the last two fractions to float by 10.6% and 2.9%, respectively. The maximal positive shift and maximal negative shift of M_t obtained are +2.7/-1.7 GeV/c^2.

5.6.6 Background Fractions

This is estimated in the background section already and the result is +3.7/-0.0 GeV/c^2.

5.6.7 Background Modelling

Since the WW Monte Carlo has the biggest difference among different generators, we take that as a measure of systematics from background shape modelling. Using PYTHIA WW sample, the lowest and highest M_t at 158.5 GeV/c^2 and 161.5 GeV/c^2 represent a shift of +2.0/-1.0 GeV/c^2. Compared to the shift with Tao Han matrix element of +4.6/+0.2 GeV/c^2, the shift due to WW modelling is -2.6/-1.2 GeV/c^2.

We assign the systematics as +0.0/-2.6 GeV/c^2.

5.6.8 Choice of Parameter

The choice of input parameter $\langle \cos \theta_{\ell b} \rangle$ is also a source of systematic uncertainty. In previous sections we have estimated that the shift is less than ± 1.6 GeV/c^2. If we re-derive the correspondence function for the shifted value of $\langle \cos \theta_{\ell b} \rangle$, the uncertainty would be much smaller. To be conservative we quote ± 1.6 GeV/c^2.

5.6.9 Summary of Systematic Uncertainty

The systematic shift and uncertainty have been estimated to be $1.4^{+7.3}_{-6.8}$ GeV/c^2. We will correct the top mass down by this shift.

99

Run/event	alias	H_T	M_1^2	M_2^2	$\langle M_{min}^2 \rangle$	$M_t^\dagger$	Acc. $\langle M_{min}^2 \rangle$	Final M_t
67581/129896	(1B $e\mu$ 2)	435	26.2	3.53	14.8	227±92.7	14.8±12.9	227±92.7
41540/127085	(DPF)	389	8.53	.981	4.75	134±55.1	9.80±6.47	187±57.3
66046/380045	(1B CEMX)	312	9.86	8.42	9.14	181±7.56	9.58±4.10	185±36.7
45047/104393	($\sim e - \mu$)	274	3.06	2.18	2.62	103±9.10	7.84±3.27	169±32.4
47122/38382	(1A CEMX)	242	.591	19.7	10.1	190±95.0	8.30±3.07	173±29.6
69808/639398	(1B $e\mu$ 3)	219	12.2	9.01	10.6	194±15.5	8.68±2.56	177±24.1
57621/45230	(1B $e\mu$ 1)	190	3.54	1.39	2.47	100±22.2	7.79±2.29	168±22.8
68185/174611	(1B ee)	178	3.74	3.31	3.53	117±4.14	7.26±2.04	163±21.0
63700/272140	(1B $\mu\mu$)	145	.763	.825	.794	—	6.54±1.89	155±20.6
58281/44805	($\mu\mu\gamma$)	138	2.92	.447	1.68	—	6.06±1.74	150±19.7

Table 5.5: The candidate events recorded in Run 1, sorted in H_T. M_1^2 and M_2^2 are the two invariant masses of the picked pair in units of 10^3 GeV^2/c^4. $\langle M_{min}^2 \rangle$ is the average of M_1^2 and M_2^2. $M_t^\dagger$ is the mass obtained for each event if we treat the $\langle M_{min}^2 \rangle$ for the event as our best estimate of the true mean and $0.14/2 * |M_1^2 - M_2^2|$ as our best estimate of the error on mean. Acc. $\langle M_{min}^2 \rangle$ is the accumulated mean of M_{min}^2 starting from the event with the highest H_T. We use $1.14 \times$RMS/$\sqrt{2N}$ as the uncertainty of Acc. $\langle M_{min}^2 \rangle$. Final M_t is the result of top quark mass from the accumulated $\langle M_{min}^2 \rangle$.

Type	Uncertainty (GeV/c^2)	
Jet Energy Uncertainty		$+1.4 \pm 2.7$
Relative Scale $\pm 2\%$		$^{+0.05}_{-0.06}$
Behrends Curve		± 1.8
Calorimeter Stability $\pm 2\%$		± 1.4
QFL Energy Shift $+2\%$		$+1.4$
Soft Gluon Radiation		± 0.3
± 1 GeV (out of 1.0 cone)		± 1.4
Different Generators	$(+0.4\pm2.3)$	± 2.3
Initial/Final State Radiation	$(+4.2\pm3.0)$	± 4.2
Monte Carlo Statistics	included in stat.	
Fractions of $t\bar{t}$ Event Types	$[+2.7/-1.7]$	± 2.7
Background Fractions	$[+3.7/-0.0]$	$^{+3.7}_{-0.0}$
Background Shape Modelling	$[-1.1/-2.6]$	$^{+0.0}_{-2.6}$
Choice of parameter	$[+1.6/-0.9]$	± 1.6
Total		$+1.4^{+7.3}_{-6.8}$

Table 5.6: Summary of systematic uncertainties. In the rows with parentheses the numbers are the central value of the shifts and the statistical errors. In the rows with [and] the numbers are the bound we obtained by changing the parameters.

Chapter 6

Conclusion and Future Prospect

We have developed a systematic method to measure top quark mass in dilepton channel. The expected statistical uncertainty is very small (< 10 GeV) if we have 10 pure WWbb type of $t\bar{t}$ events with leptons and b-jets correctly paired. Without a perfect pairing algorithm and the presence of "g" type of jets makes the statistical uncertainty increase by a factor of 2.

Applying our method to 8 high H_T dilepton candidates results in a top quark mass of

$$162 \pm 21(stat.)^{+6.8}_{-7.3}(syst.) \text{ GeV}/c^2.$$

In Fermilab Collider Run II we expect 2 fb^{-1} of data recorded on tape so the statistics will increase by a factor of 20. The improved coverage of upgraded trackers will increase the lepton acceptance by approximately 30% to 45%.[54]. Taking into account both factors we expect about 280 dilepton events in Run II. The statistical error of top quark mass from dilepton channel will be ≈ 2.5 GeV/c^2.

Further improvements on the method itself are still possible. For example, raising jet E_T thresholds can reduce the "g" type of jets without sacrificing much signal. The other direction is to study the pairing algorithm. We expect to gain $\sim 15\%$ on statistical uncertainty if a 80% efficient pairing algorithm can be found. Under the assumption that these improvements are realized, the resolution of top quark mass in Run II can reach 2 GeV/c^2 and the mass measurement will be limited by systematic uncertainties.

Bibliography

[1] UA1 collaboration, "Experimental Observation of Isolated Large Transverse Energy Electrons with Associated Missing Energy at $\sqrt{S}$ = 540 GeV." Phys. Lett. **122B**, 103 (1983).

[2] UA2 collaboration, "Observation of Single Isolated Electrons of High Transvers Momentum in Events with Missing Transvers Energy at the CERN $\bar{p}p$ Collider." Phys. Lett. **122B**, 476 (1983).

[3] UA1 collaboration, "Experimental Observation of Lepton Pairs of Invariant Mass around 96 GeV/c² at the CERN SPS Collider." Phys. Lett. **126B**, 398 (1983).

[4] UA2 collaboration, "Evidence for $Z^0 \rightarrow e^+e^-$ at the CERN $\bar{p}p$ Collider." Phys. Lett. **129B**, 130 (1983).

[5] R. Brandelik et. al. (TASSO collaboration), "Evidence for planar events in e^+e^- annihilation at high energies." Phys. Lett. **86B**, 243 (1979).

[6] Particle Data Group, "Review of Particle Properties." Phys. Rev. D **50**, 1395 (1994).

[7] S. Herb et. al., "Observation of a Dimuon Resonance at 9.5 GeV in 400-GeV Proton-Nucleus Collisions." Phys. Rev. Lett. **39**, 252 (1977).

[8] F. Abe et. al. (CDF collaboration), "Evidence for top quark production in $\bar{p}p$ collisions at $\sqrt{s}$ = 1.8 TeV." Phys. Rev. D **50**, 2966 (1994).

[9] Chris Quigg, "Top-ology." FERMILAB-CONF-95/139-T, hep-ph/9507257, 1995.

[10] P. D. B. Collins, A .D. Martin, E. J. Squires, "Particle Physics and Cosmology." p.109.

[11] M. Acciarri *et. al.* (L3 collaboration), "Measurement of the $B^0 - \bar{B}^0$ Mixing Parameter and the $Z \to b\bar{b}$ Forward-Backward Asymmetry." Phys. Lett. B **335**, 542 (1994).

[12] P. Abreu *et. al.* (DELPHI collaboration), "Measurement of the forward-backward asymmetry of $e^+e^- \to Z \to b\bar{b}$ using prompt leptons and a lifetime tag." Phys. Z. Phys. C **65**, 569 (1995).

[13] R. Akers *et. al.* (OPAL collaboration), "A measurement of the forward-backward asymmetry of $e^+e^- \to b\bar{b}$ by applying a jet charge algorithm to lifetime tagged events.." Z. Phys. C **67**, 365 (1995).

[14] S. L. Glashow, J. Iliopoulos, and L. Maiant, "Weak Interactions with Lepton-Hadron Symmetry." Phys. Rev. D **2**, 1285 (1970).

[15] A. Bean *et. al.* (CLEO collaboration), "Improved upper limit on flavor-changing neutral-current decays of the b quark.." Phys. Rev. D **35**, 3533 (1987).

[16] Particle Data Group, "Review of Particle Properties." Phys. Rev. D **35**, 1172 (1944) p.1208.

[17] F. Abe *et. al.* (CDF collaboration), "Observation of top quark production in $\bar{p}p$ collisions with the Collider Detector at Fermilab." Phys. Rev. Lett. **74**, 2626 (1995).

[18] S. Abachi *et. al.* (D0 collaboration), "Observation of the Top Quark." Phys. Rev. Lett. **74**, 2632 (1995).

[19] C. Albajar *et. al.* (UA1 collaboration), "Search for new heavy quarks at the CERN proton-antiproton collider." Z. Phys. C **37**, 505 (1988).

[20] F. Abe *et. al.* (CDF collaboration), "Top-quark search in the electron+jets channel in proton-antiproton collisions at $\sqrt{s} = 1.8$ TeV." Phys. Rev. D **43**, 664 (1991).

[21] F. Abe *et. al.* (CDF collaboration), "Lower Limit on the Top-Quark Mass from Events with Two Leptons in $p\bar{p}$ collisions at $\sqrt{s} = 1.8$ TeV." Phys. Rev. Lett. **68**, 447 (1992).

[22] S. Abachi *et. al.* (D0 collaboration), "Search for the Top-Quark in $p\bar{p}$ collisions at $\sqrt{s} = 1.8$ TeV.." Phys. Rev. Lett. **72**, 2138 (1994).

[23] I. Bigi *et. al.*, "Production and decay properties of ultra-heavy quarks." Phys. Lett. B **181**, 157 (1986).

[24] G. L. Kane, G. A. Ladinsky and C. -P. Yuan, "Using the top quark for testing standard-model polarization and CP predictions." Phys. Rev. D **45**, 124 (1992).

[25] This can be derived easily, see, for example, Particle Data Group, "Review of Particle Properties." Phys. Rev. D **35**, 1172 (1944) p.1292.

[26] D. Amidei *et. al.*, "The CDF Silicon Vertex Detector." Nucl. Inst. Meth. Phys. Res. **A350**, 73 (1994).

[27] D. Amidei *et. al.*, "SVX': The New CDF Silicon Vertex Detector." Nucl. Inst. Meth. Phys. Res. **A360**, 137 (1995).

[28] F. Snider *et. al.*, "The CDF Vertex Time Projection Chamber System." Nucl. Inst. Meth. Phys. Res. **A268**, 75 (1988).

[29] F. Bedeschi *et. al.*, "Design and Construction of the CDF Central Tracking Chamber." Nucl. Inst. Meth. Phys. Res. **A268**, 50 (1988).

[30] L. Balka *et. al.*, "The CDF Central Electromagnetic Calorimeter." Nucl. Inst. Meth. Phys. Res. **A267**, 272 (1988).

[31] S. Bertolucci *et. al.*, "The CDF Central and Endwall Hadron Calorimeter." Nucl. Inst. Meth. Phys. Res. **A267**, 301 (1988).

[32] Y. Fukui *et. al.*, "CDF End Plug Electromagnetic Calorimeter Using Conductive Plastic Proportional Tubes." Nucl. Inst. Meth. Phys. Res. **A267**, 280 (1988).

[33] G. Brandenburg *et. al.*, "An Electromagnetic Calorimeter for the Small Angle Regions of the Collider Detector at Fermilab." Nucl. Inst. Meth. Phys. Res. **A267**, 257 (1988).

[34] S. Cihangir *et. al.*, "The CDF Forward/Backward Hadron Calorimeter." Nucl. Inst. Meth. Phys. Res. **A267**, 249 (1988).

[35] G. Ascoli *et. al.*, "CDF Central Muon Detector." Nucl. Inst. Meth. Phys. Res. **A268**, 33 (1988).

[36] K. Byrum *et. al.*, "The CDF Forward Muon System." Nucl. Inst. Meth. Phys. Res. **A268**, 46 (1988).

[37] D. Ameidei *et. al.*, "A Two Level Fastbus Based Trigger System for CDF." Nucl. Inst. Meth. Phys. Res. **A269**, 51 (1988).

[38] J. Carroll *et. al.*, "The CDF Level 3 Trigger." Nucl. Inst. Meth. Phys. Res. **A300**, 552 (1991).

[39] G. Ascoli *et. al.*, "CDF Central Muon Level-1 Trigger ELectronics." Nucl. Inst. Meth. Phys. Res. **A269**, 63 (1988).

[40] P. Derwent and B. Flaugher, "Comparison of Dielectron Mass, Run 0, Run IA, and Run IB." CDF internal note 2880.

[41] W. Yao *et. al.*, "Studies of Gluon Radiation Systematics with $b\bar{b}$ events and a Proposal for a Jet Energy Correction Based on Multiple Underlying Events." CDF internal note 3257.

[42] L. Keeble and B. Flaugher, "New Jet Correction Function QDJSCO 2.0." CDF internal note 1513.

[43] M. Kruse *et. al.*, "Top Acceptance in the Dilepton Channel for Run 1B." CDF internal note 3300.

[44] M. Contreras, "Estimate of the Drell-Yan background in the Top Dilepton Analysis." CDF internal note 2261.

[45] J. Konigsberg, "Drell-Yan Backgrounds for the Top Dilepton Analysis in 100 pb−1." CDF internal note 3208.

[46] Q. F. Wang, "A Dilepton Fake Rate Study in Top Search." CDF internal note 2102.

[47] J. Romano et. al., "Background due to Hadron Misidentification in to Top Dilepton Search." CDF internal note 2107.

[48] J. Wang et. al., "Estimate of $Z^0 \to \tau^+\tau^-$ background in the Top Dilepton Analysis." CDF internal note 2108.

[49] J. Antoš, "Simple Method for Top Quark Mass Determination." CDF internal note 3449.

[50] D. J. Winn and D. Amidei, "Study of the $t \to Wb$ Vertex at CDF." CDF internal note 2914.

[51] A. Beretvas and M. Binkley, "W Polarization in Top Decay." CDF internal note 3380.

[52] L. Galtieri et. al., "Top mass determination by likelihood method." CDF internal note 2470.

[53] B. Harral, "Comments on Likelihood Method for Extracting M_{top}." CDF internal note 2503.

[54] R. Roser and R. Hughes, "How the improvements in the Run 2 Detector impact the top yield." CDF Top Group Meeting, March 28, 1996.

[55] P. L. Jolivette, "Least-Square fits when there are errors in X." Computers in Physics, Vol 7, No. 2, Mar/Apr 1993.

[56] T. Chikamatsu et. al., "Top Dilepton Analysis — Run 1." CDF internal note 2851.

[57] C. Loomis, "Comparison of Run 1B Isolated Pions to Previous Studies and QFL Monte Carlo." CDF internal note 3554.